Winter 2015

Assessing coupled mechanical behavior and environmental degradation at submicron scales

Samantha K Lawrence
Purdue University

PURDUE UNIVERSITY
GRADUATE SCHOOL
Thesis/Dissertation Acceptance

This is to certify that the thesis/dissertation prepared

By Samantha K. Lawrence

Entitled

ASSESSING COUPLED MECHANICAL BEHAVIOR AND ENVIRONMENTAL DEGRADATION AT SUBMICRON SCALES

For the degree of Doctor of Philosophy

Is approved by the final examining committee:

David F. Bahr

David R. Johnson

Robert H. Spitzer

Rodney W. Trice

To the best of my knowledge and as understood by the student in the Thesis/Dissertation Agreement, Publication Delay, and Certification Disclaimer (Graduate School Form 32), this thesis/dissertation adheres to the provisions of Purdue University's "Policy of Integrity in Research" and the use of copyright material.

Approved by Major Professor(s): David F. Bahr

Approved by: David F. Bahr 1/16/2015

Head of the Departmental Graduate Program Date

ASSESSING COUPLED MECHANICAL BEHAVIOR AND ENVIRONMENTAL DEGRADATION AT SUBMICRON SCALES

A Dissertation

Submitted to the Faculty

of

Purdue University

by

Samantha K. Lawrence

In Partial Fulfillment of the

Requirements for the Degree

of

Doctor of Philosophy

May 2015

Purdue University

West Lafayette, Indiana

For my parents, my first and best teachers.

ACKNOWLEDGEMENTS

Financial support for my studies through the Department of Energy, National Nuclear Security Administration, Stewardship Science Graduate Fellowship (DOE NNSA SSGF), under contract DE-NA0002135 is gratefully acknowledged. I'd like to thank the staff at the Krell Institute, particularly Lucille Kilmer, for finding solutions to unique problems with all due haste, with plenty of kindness, and a welcome dash of humor. I must also acknowledge financial support through NSF/CMMI grant 1030843 and Defense Threat Reduction Agency, Basic Research Award # IACRO 13-5897I.

First and foremost I would thank my advisor, David Bahr, whose wise and witty guidance has enabled me to successfully tackle each adventure that has comprised my Ph.D. In addition to an excellent thesis advisor, I have been fortunate to have multiple mentors at Sandia National Laboratories. I am grateful to Neville Moody for welcoming me onto the Sandia team and finding opportunities for me to grow into and serve my scientific community; to David Adams for providing guidance from the "mother ship" for three years and an open door when I was able to join the Surface and Coatings Technology group for a few months; and to Brian Somerday for fostering my interest in hydrogen effects on materials and encouraging me to ask, and answer, difficult questions through numerous enlightening conversations.

I owe many thanks to my collaborators Megan Cordill, Doug Stauffer, Iman Salehinia, and Stefan Wurster, for experimental help and fruitful conversations; to Yuri Yagodzinskyy for his enthusiasm to collaborate, host me at Aalto University, and provide the opportunity to conduct TDS and PAS with Olga Todoshenko and Esa Korhonen; to the other members of the Bahr research group—Michael Maughan, Rachel Schoeppner, Nannan Tian, and Mohammad Zbib—for friendship and brainstorming; to the Sandians with whom I've been privileged to work and share a laugh or two: Jeff Campbell, Ray Friddle, Carter Hodges, and David Saiz. And a special thanks to Profs. Hussein Zbib and David Field of WSU, who continued to offer advice and support after I moved to Purdue.

I would also like to acknowledge those outside my academic community who helped me to thrive these four years. Father Cummins and the St. Florence Saturday evening crowd for cheering me on and reminding me that "qué sera, sera". Shalie, for always picking up right where we left off. My aunts, uncles, and cousins who have shown me the strength of family even when I'm thousands of miles away. Brit, for reminding me that it's okay to live in a glass house of emotion from time to time. My sister Julie, who has always been available to talk and particularly adept at making me laugh when I needed it most. Scott and Anna Gibbs for making me feel like part of the family from day one. And Paul Gibbs, for having a fisherman's care and patience with this oft-changing river.

Finally, words are not enough to express my gratitude to my parents, who have stood beside me throughout every victory and every failure, loved me through every challenge, and willed me to continue running the race, especially when the going got tough. The Lord has truly blessed me to have such strength and love upon which to draw when I felt empty.

TABLE OF CONTENTS

Page

Page

Page

LIST OF TABLES

Table Page

Table Page

LIST OF FIGURES

Figure Page

Figure Page

Figure Page

Figure Page

Figure Page

Figure Page

Figure Page

Figure Page

ABSTRACT

Lawrence, Samantha K. Ph.D. Purdue University, May 2015. Assessing Coupled Mechanical Behavior and Environmental Degradation at Submicron Scales. Major Professor: David Bahr.

Mechanical and electromechanical properties, deformation and fracture mechanisms, and environmental resistance of materials at submicron scales have been investigated through the combination of nanomechanical testing, high resolution microscopy, diffraction, and electrochemical testing. Nanomechanical techniques were used to isolate environmental, orientation, and size effects. Material evaluation focuses on metals, both model and engineering alloys, in bulk and thin-film form as well as oxide-substrate systems. Yield behavior of Ni 200, a model material, depends on sampled volume size, orientation, and surface preparation. Exposure to high-pressure hydrogen gas is also found to impact incipient plasticity and mechanical properties of commercially pure Ni 201. Nanomechanical testing of oxide-substrate systems can be used to study coupling of environment and size effects. Investigation of films grown on 304L stainless steel and commercially pure grade II Ti *via* nanosecond pulsed laser irradiation has enabled isolation of film fracture behavior and the effect of processing on mechanical and electromechanical properties. Additionally, laser processing causes substrate composition gradients that limit environmental stability. Combining techniques provides a unique approach for understanding and improving materials reliability in harsh environments.

CHAPTER 1. INTRODUCTION

As materials are exposed to harsher environments and tighter tolerances in high-performance applications, understanding the coupling of mechanical behavior and environmental effects is vital for designing alloys and safe-operating systems. Mechanical behavior of materials in small, constrained, volumes is often drastically different from mechanical behavior of bulk materials. Development of engineering applications dependent on length scales from a few nanometers to a few hundred microns requires a fundamental understanding of scaling effects on deformation. Due to the unique challenges of small-scale materials research in extreme environments, coupled development of fundamental modeling with experimental validation provides the most effective method for advancing the understanding of mechanisms involved in dislocation motion, deformation, and fracture of nanometer-scale materials.

Robust materials models that span length and time scales require experimental validation under equivalent conditions. There is an ongoing debate in literature surrounding the idea that “smaller is stronger”; efforts continue to uncouple specimen size and sample preparation effects from deformation mechanisms.[1–5] The current study compares small-scale and bulk-like materials testing in an effort to quantify the impact of sample size, surfaces, and environment on deformation and failure of metals and oxide-metal substrate systems. Mechanical testing data has been coupled with advanced

characterization techniques and dislocation theory to identify defects, particularly dislocations, grain boundaries, and interfaces.

The objectives of the doctoral research described herein were threefold: (1) *demonstrate* the ability to quantify relationships between structure and mechanical properties in sub-micron volumes of materials, (2) *determine* the changes in performance of engineering alloys when exposed to harsh environmental conditions, (3) *predict and control* the microstructural response of these materials to perform reliably in harsh environments. The critical mechanical properties that have been considered in this work include the stress required to initiate plasticity and the fracture behavior of oxide films on metals.

The following chapters will discuss work conducted in order to understand coupling of sampled volume and material preparation on yield behavior, to develop mechanically and environmentally robust oxide coatings on alloy substrates, and to interrogate the effect of dissolved hydrogen on mechanical behavior of Ni alloys.

Chapter 2 will discuss the impact of indenter tip radius and grain orientation on measured mechanical properties and yield behavior of a commercially pure model alloy, Ni 200. Material testing during this investigation suggested that the condition of the indented surface also had a measurable effect on yield. This chapter was originally published as a paper in the Journal of Materials Research.

Three sample preparation techniques were chosen to quantify the effect of indented surface condition on mean yield pressure. This investigation, presented in Chapter 3, highlights the use of small value statistics in quantifying incipient plasticity in

Ni 200. This chapter is an original publication in Metallurgical and Materials Transactions A.

The indention techniques explained in the previous chapters were next applied to novel oxide coatings fabricated on stainless steel 304L and commercially pure grade II titanium using a nanosecond pulsed laser irradiation technique. Chapter 4 is the inaugural investigation of phase, morphology, deformation and fracture behavior, and electromechanical properties of oxides grown on CP grade II Ti using techniques such as X-ray diffraction, electron mircroscopy, and nanoindentation. The overarching goal of these investigations is to determine archivable properties of laser-fabricated films which can then be used as passive authentication structures. This work was published in the Journal of Materials Science.

Chapter 5 is a commensurate investigation into the phase, morphology, mechanical and electromechanical properties of oxides grown on stainless steel 304L. The results suggest that oxides films are mechanically robust and well-adhered to the substrate. This work was originally published in Surface and Coatings Technology.

Laser-fabricated oxide films to be used as passive authentication structures must be resistant to environmental degradation, in addition to being mechanically robust. Chapter 6 represents the first efforts to determine the environmental resistance of oxides on both stainless steel and Ti by testing with respect to the most aggressive anticipated service condition. Oxide-substrate systems are exposed to a salt fog atmosphere and are anodically polarized in a 3% NaCl solution to achieve this goal. The Ti system is stable under all conditions, but the stainless steel system suffers from substrate corrosion in specific conditions. This corrosion is ascribed to Cr depletion in the melt zone of the

substrate as a result of laser processing. However, certain oxides are protective in chloride containing environments.

Working from the results obtained in the previous chapter, an effort was initiated to enhance the corrosion resistance of the stainless steel system. Chapter 7 focuses on the development of layered oxide coatings with total thicknesses matching those found to be protective in the previous study. The results suggest that processing parameters can be tailored to mitigate the effects of chloride attack.

The remaining chapters address a different, but critical, materials reliability issue: hydrogen degradation of metallic systems. Nanoindentation, electron diffraction, and atomic force microscopy are initially combined to assess the effect of dissolved hydrogen on mechanical behavior of a commercially pure alloy, Ni 201. Chapter 8 evaluates the orientation dependent reduction in measured mechanical properties in terms of the hydrogen enhanced decohesion (HEDE) mechanism.

Conversely, Chapter 9 highlights the importance of the hydrogen enhanced localized plasticity (HELP) mechanism in slip transmission across special and random grain boundaries in Ni 201. Grain boundary misorientation is found to affect the likelihood of slip transmission, which ultimately contributes to the propensity for intergranular failure of this Ni alloy. This work was originally published in the Journal of Materials.

Finally, Chapter 10 presents preliminary results of an investigation into the importance of vacancy concentration in hydrogen degradation of Ni alloys. This study suggests that prior deformation and grain size, which affect free volume, plays a critical

role in the generation and agglomeration of vacancies in hydrogen charged Ni. Additional work is required to clarify these results.

CHAPTER 2. CRYSTALLOGRAPHIC ORIENTATION AND INDENTER RADIUS EFFECTS ON THE ONSET OF PLASTICITY DURING NANOINDENTATION

Previously published by Journal of Materials Research*, Volume 27, pages 3058-3065, in December 2012*

2.1 Introduction

Nanoscale instrumented indentation provides the ability to accurately measure indentation load and penetration depth and thus extract properties such as elastic modulus, hardness, and onset of plasticity, thereby allowing characterization of small-scale mechanical behavior.[6,7] The onset of plasticity in load-controlled nanoindentation experiments of relatively defect-free solids is often associated with a sudden displacement burst or "pop-in," i.e., a sudden increase in penetration depth with no corresponding increase in indentation load. Pop-ins have been associated with fracture of a surface oxide,[8] but in a material relatively free of dislocations, pop-ins are often believed to be associated with dislocation nucleation under the indenter, either in a homogenous state or from point defects.[9–11] The correspondence of pop-in behavior with the onset of plasticity is derived from observations that deformation before pop-in is purely elastic. The load–displacement curve before pop-in is fully reversible and can be generally described by Hertzian contact theory:

$$P = \frac{4}{3} E^* \sqrt{R h^3}, \qquad \text{Equation 2.1}$$

here R is the indenter radius, E^* is the reduced modulus, and h is the indentation contact depth. This is only an approximation, and the real tip geometry alters the actual stress distribution under the contact surface; to first order, a Hertzian approximation will generally underestimate the true maximum shear stress by approximately 30%.[12] Additionally, if the indenter is unloaded before pop-in, atomic force microscopy reveals no residual indent; conversely, if unloading occurs after pop-in, a residual impression of the indent is observed.[10] There are reports from in situ indentations using transmission electron microscopy that identified pop-in events after dislocation nucleation,[13] which matches experimental ex-situ indentation observations of pop-ins occurring after elastic loading. While these events can be fit with a Hertzian-type power load, they are not purely elastic.[14]

There remain significant challenges in directly correlating loading discontinuities during the indentation process with homogenous dislocation nucleation. One particular difficulty arises from preexisting dislocations. Even in well-annealed metallic single crystals, the initial dislocation density may be on the order of 10^{11} m^{-2}, and with even slight deformation due to processing, the surface dislocation density can increase to a value beyond 10^{12} m^{-2}.[15] Thus, there is a significant probability that the stress field beneath the indenter tip will interact with a preexisting dislocation after only a small amount of elastic loading. Other investigators have also suggested that incipient plasticity is rate limited by a low-energy process on the scale of a single point defect.[16] This could even be true in a sample with existing dislocations; if a process such as double kink nucleation was the rate-limiting step in generating plastic deformation, assuming that the critical double kink width was on the order of the Burgers' vector, it would be possible to

determine an activation volume on the order of an atomistic volume even in the presence of dislocations.

For the current study, a polycrystalline sample of commercially pure nickel was annealed to produce large grains for orientation-specific indentation, and multiple tip geometries were used for indentation to investigate the effect of tip radius on deformation. Nickel is known to be elastically anisotropic: the elastic modulus ranges from 138 GPa in the <001> direction to 215 GPa in the <110> direction and to 262 GPa in the <111> direction,[17] thus it is a good candidate material for investigating anisotropy in deformation. Deformation results are discussed in terms of orientation and size effects, with respect to the presence of defects within the material.

2.2 Experimental Procedures

A sample of nickel 200 (hereafter, Ni200), approximately 13 mm in diameter and 2 mm thick, was prepared by cutting, rolling to 20% deformation, and annealing to generate large (0.5-mm-scale) grains. The maximum allowable impurities for this alloy by weight are 0.25% Cu, 0.4% Fe, 0.35% Mn, 0.15% C, 0.35% Si, 0.01% S. The Ni200 was annealed in air at 1150 °C for 24 h and then air-cooled. It was ground through 1200 grit SiC, mechanically polished with 3- and 0.5-μm diamond compound, and finally polished with 0.02-μm colloidal silica on a vibratory polisher until a clean, flat, mirror finish surface suitable for electron back scatter diffraction (EBSD) was achieved. Fiduciary marks were then made using Vickers micro-indentations, so as to be able to locate grains identified with EBSD when nanoindentation was performed. EBSD data were obtained using orientation image microscopy from TSL (TSL/EDAX, Draper, UT),

attached to a FEI FEG/SFEG scanning electron microscope (FEI Company, Hillsboro, OR). Inverse pole figure (IPF) maps were generated for grains around fiduciary marks, and grain orientations were identified. Grains to be indented were selected based on the IPFs. A grain oriented at each vertex of the stereographic triangle was selected; two additional grains with orientations between the vertices were also selected. The sample was electropolished using a solution of 37% H_3PO_4, 56% glycerol, and 7% H2O, etching the top few micrometers of material, thereby effectively removing any residual damage layer from mechanical polishing. EBSD was repeated to verify grain orientations. Specifically oriented grains were then indented using a Hysitron Triboindenter (Hysitron, Inc., Minneapolis, MN) with three tips of varying geometry: Berkovich, conical, and cube corner. A series of 25 indents were performed in each grain. A five-segment partial unloading load function was used with peak loads ranging from 250 to 7000 μN. All indentations were separated by 15 μm to ensure that no previous indentation influenced a subsequent indentation. The load–depth curves generated were analyzed to determine reduced modulus, hardness, and "pop-in" load and depth as a function of orientation and indenter size.

2.3 Results

Indentation of uniquely oriented grains reveals a pronounced orientation effect of yielding. The orientation effect, however, is somewhat overshadowed by the effect of indenter tip radius. Each effect will be addressed separately. The effect of orientation on yield point data is obtained by indenting grains with specifically oriented planes, which are identified using EBSD. The IPF map obtained from EBSD is shown in Figure 2.1. Indented grains are labeled and approximate locations of the specific indents are

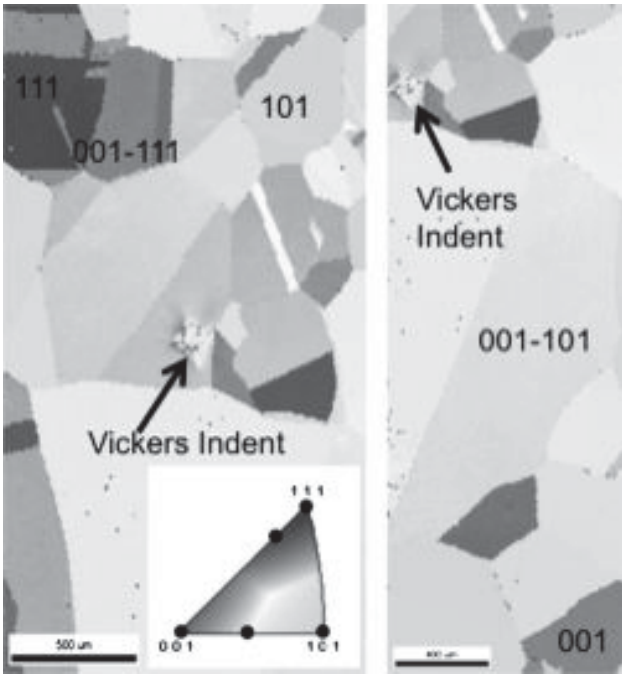

Figure 2.1 IPF maps generated from EBSD. Indented grains are labeled with their orientations. Fiduciary Vickers indents are also labeled. Black circles on the stereographic triangle indicate approximate orientation positions.

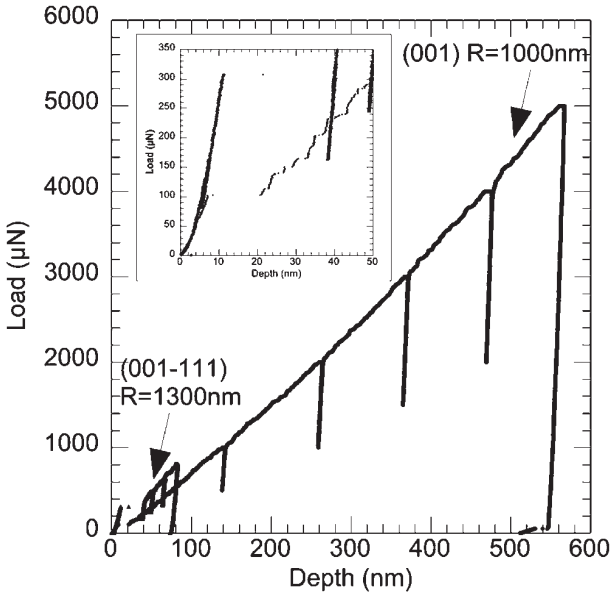

Figure 2.2 Examples of load-depth curves showing "pop-ins." The inset shows an expanded view of the region. The curve with a yield point of ~300 μN exhibits an elastic unload/reload prior to yield.

indicated. For those indents that exhibit a yield point (pop-in) at the onset of plastic deformation, the load and depth of yield point initiation are recorded; Figure 2.2 presents examples of two pop-in events. To first order, Hertzian contact mechanics [18] was used to calculate maximum pressure (p_0) at yield knowing that:

$$\delta = \frac{a^2}{R} = \left[\frac{9P^2}{16RE^{*2}}\right]^{1/3}, \text{ Equation 2.2}$$

where δ is the contact depth at the yield point, P is the load at the yield point, a is the contact radius, R is the indenter radius, and E^* is the reduced modulus. Hertzian approximations are only valid for small strain criterion and can underestimate the stress field beneath typical nanoindentation tests;[12,19] however, since the contact depths at pop-in for these experiments are less than *R/3*, the low strain approximation is reasonable for the following discussion. For this analysis, the average measured indentation modulus for each grain (using a classical Oliver–Pharr approach [7]) was used to account for anisotropic elastic properties. From Equation 2.2, R is given by:

$$R = \frac{9P^2}{\delta^3 16E^{*2}}. \quad \text{Equation 2.3}$$

Since the load and depth at the yield point are used in this calculation, the R obtained is the "instantaneous radius," i.e., the radius of the indenter contact at the moment of pop-in (this is a first order attempt to address the fact that the tips are not perfect spheres). With the instantaneous radius, the yield load, and the orientation-dependent average reduced modulus, the maximum pressure is calculated using:

$$p_o = \frac{3P}{2\pi a^2} = \left[\frac{6PE^{*2}}{\pi^3 R_i^2}\right]^{1/3}. \qquad \text{Equation 2.4}$$

A cumulative fraction plot of the maximum pressure at pop-in was used to compare the distribution of p_0 at yield as a function of orientation. Figure 2.3 shows typical results for indents performed with a Berkovich indenter on electropolished Ni200. The (001) oriented grain clearly exhibits a higher p_0 at yield than the (111) grain.

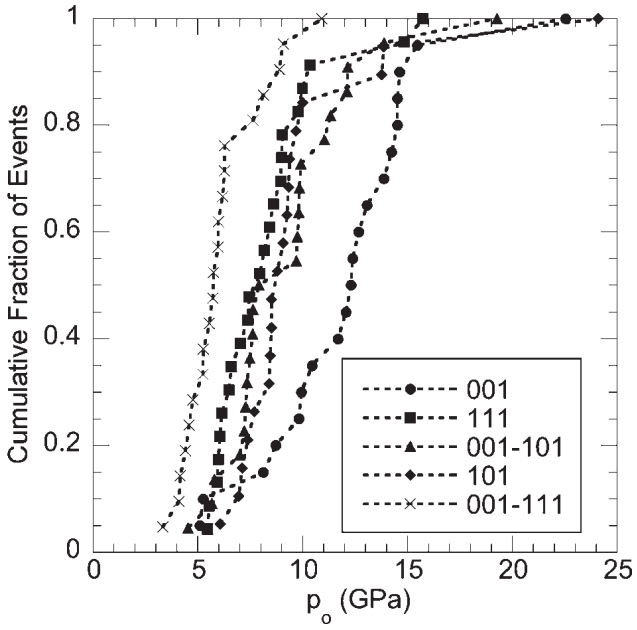

Figure 2.3 Maximum pressure at pop-in as a function of orientation. Indentation performed with a blunt Berkovich indenter. (001)-oriented grain exhibits p_o values higher than those of (110) or (111) orientations.

Indentation with tips of varying effective tip radii was performed to determine if a size effect was present and if this effect was impacted by orientation. Figure 2.4 shows a cumulative fraction plot of maximum pressure for two specific grain orientations for each of the three indenter tip geometries. The Berkovich tip has an approximate tip radius, R, of 1300 nm and an included angle, θ, of 142.3°, the conical tip has R ≈ 1000 nm and θ =

90°, and the cube corner tip has $R \approx 100$ nm and $\theta = 90°$. The data indicate that tip radius does impact the onset of plasticity during nanoindentation. In this case, radius is likely more important than included angle since all pop-in behavior occurs in the pseudospherical region, well below the depth at which the tip becomes self-similar.

In determining the mean pressure during any nanoindentation test, there are three likely sources of uncertainty: changing the effective tip radius as a result of variation in indentation depth, i.e., the tips are not actually spheres,[12] apparent radii differences due to indenting on a nonflat sample surface (contact with flat, concave, or convex roughness), and instrument accuracy. The method for determining pressure at yield, using the tip radius measured at the initiation of plasticity, detailed above accounts for radius uncertainty due to both indentation to different depths as well as due to indenting a nonflat surface. The only remaining uncertainty deals with instrument resolution. Since mean pressure varies as depth squared, it is the most sensitive to depth ranges and instrument resolution; we thus expect a maximum uncertainty in pressure of 10%. For clarity, error bars were not included in Figure 2.4 or Figure 2.5.

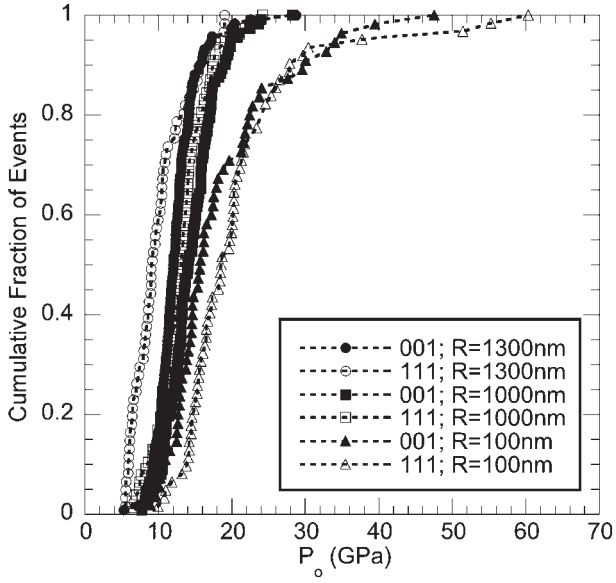

Figure 2.4 Interaction of orientation and indenter radius effects on maximum pressure. For clarity, data presented are compiled from two sets of two indented grains with the same nominal orientation. The blunt Berkovich tip is sensitive to orientation, while the sharp cube corner tip is relatively insensitive to orientation but shows a pronounced radius effect, postulated to be the result of defects. A maximum 10% uncertainty is expected due to instrument resolution; for clarity, error bars have not been added to the data points.

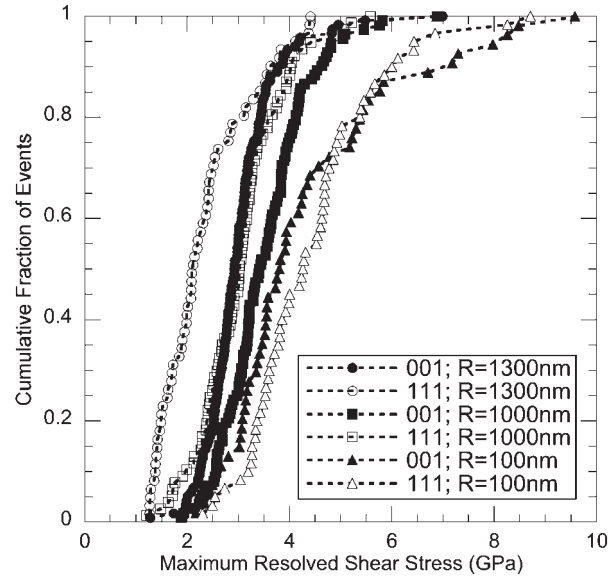

Figure 2.5 Correlation of orientation and radius effect on maximum resolved shear stress. For clarity, data presented are compiled from two sets of two indented grains with the same nominal orientation. A maximum 10% uncertainty in the calculation is expected due to instrument resolution; error bars have not been added to the data points.

2.4 Discussion

2.4.1 Sampled Volume Effects

Figure 2.3 indicates that the yield point is orientation dependent for Ni200 when probed with a large radius indenter. Figure 2.4 implies that orientation dependence is a function of indenter radius. Blunt or large radius tips are more sensitive to orientation, while the effect is less prevalent for tips with a smaller radius. Other experiments on gold have shown similar orientation effects[20,21] and similar trends with the effect of radius on pop-in loads have been observed in Ni_3Al[22] and NiAl[23], while other research in our group indicates that as experimental tip radius decreases, the orientation effect begins to align with that seen via atomistic modeling.[24] As tip radius decreases, the relative invariance in yield pressures for different crystallographic orientations is likely due to a higher probability of indenting a relatively defect-free volume under the indenter.[25] The effect of defects on the initiation of plasticity for small radius tips is lower, thus pop-in pressures are likely controlled by shear stresses and orientation. These trends have been enumerated in literature as well.[21] Assuming that the maximum pressure is near a "perfect" crystal location, then the lowest yield pressures are likely tied to the "worst-case" position of a defect.[26] The experimental range of yield pressures is largest for the (111) orientation and lower for the (001) and (101). The lack of significant variation in the lowest observed yield pressure would indicate either a relatively constant defect density, i.e., many indentations will sample a defect but not one in the "worst-case" position, or a defect density, which is on average so small that it is unlikely that the critical stressed volume under the indenter tip contains a heterogeneous dislocation source. Structural defects have a greater effect for the larger radius tip than that for the smaller radius tip.

The larger radius tip creates a larger volume under stress at a given pressure, which is more likely to sample either multiple or larger defects. In this case, the effect of structural defects on the onset of plasticity may be more complex than in simulations. The question then arises: is dominance of tip radius (size) over orientation a result of existing defects or a result of a fundamental size effect?

2.4.2 Defects within Sampled Volumes

If the effect is a result of structural defects, then a plausible mechanism must be identified. Vacancies and stacking fault tetrahedra are unlikely to be present in significant concentrations in these samples due to the long annealing and slow cooling cycle. Impurities may play a role, but likely a small one, because the sample is a commercially pure Ni alloy and the composition should be independent of orientation. The interaction of dislocations with impurities in commercially pure nickel would lead to local strain hardening, as observed by nanohardness testing. Surface asperities are unlikely contributors as the surface roughness (*Ra*) of the electropolished surface was measured, using atomic force microscopy, to be only 1.71±0.4 nm for all samples. The most likely subsurface defects, then, are dislocations. It has been shown that even in materials with substantial dislocation densities, it is possible to generate a sudden transition from elastic to plastic deformation.[15] Using conical indentation, Li et al. have shown an orientation effect, which corresponds with the Berkovich indentation orientation effect observed in this work. The authors suggested that the large pop-in loads measured for orientations close to <001> correspond with a large contact area at pop-in, thus there is a higher probability of activating preexisting dislocations.[23] Our group has proposed that the

orientations near (001) are less sensitive to defects but more sensitive to crystallography, while the (111) planes are more sensitive to the impact of defects. Based on the Taylor relation, an upper bound for total dislocation density can be estimated from:

$$\tau = \alpha G b \sqrt{\rho_T}, \qquad \text{Equation 2.5}$$

where τ is the shear stress calculated at the yield point from:

$$\tau = \frac{H}{6}, \qquad \text{Equation 2.6}$$

H is the approximate Vickers hardness of the bulk, 738 MPa, *G* is the bulk modulus determined from the relationship $G = E/2(1+\nu)$, *b* is the Burgers' vector, *a* is a constant 0.3,[27] and ρ_T is the total dislocation density, including both statistically stored dislocations as well as geometrically necessary dislocations. Using these equations, an upper bound ρ_T calculated from indents in electropolished Ni200 is on the order of 10^{14} m^{-2}. This value is clearly an extremum, as it was obtained after the sample was annealed, mechanically polished, and then electropolished. It is, however, likely that the dominance of tip radius is due in part to interactions with dislocations; the volume of material under significant shear stress for the largest indenter tips will be on the order of the spacing between dislocations. As tip radius decreases, thereby decreasing sampling volume, fewer defects are probed, and thus, their impact on properties becomes less important. Additionally, as tip radius and thus sampling volume decreases, the likelihood of activating a dislocation source of strength similar to those activated by a blunt tip decreases, and thus, a higher pressure is needed to initiate the process. This reasoning has also been suggested by Wang et al.[28] As dislocation nucleation beneath an indenter tip

should be a shear-biased event,[29–31] it follows that source activation can also be examined in terms of shear stresses. Calculating the resolved maximum shear stress for each orientation and tip geometry combination provides a means of comparing orientation and radius effects. Maximum resolved shear stress, τ_{rss}^{max}, is calculated with the formula used by Li et al.:

$$\tau_{rss}^{max} = S * p_o, \qquad \text{Equation 2.7}$$

where p_o is the maximum pressure determined with Equation 2.4 and S is the indentation Schmid factor.[23] A linear interpolation based on their Schmid factor map was used to determine the values of S for indented orientations on the (001–111) and (001–101) boundaries. Figure 2.5 is a cumulative fraction plot of τ_{rss}^{max} for the (001) and (111) orientations indented with all three tip geometries. In agreement with the maximum contact pressure data, the highest τ_{rss}^{max} values are achieved with the sharpest tip, while the most prominent orientation effect is observed for the blunt tip. This examination matches with the postulation that activating a source with a sharp tip requires a higher pressure, or for this analysis, shear stress. We have shown that despite careful sample preparation, the surface of indented grains of Ni200 can have a relatively high existing dislocation density. If this is the case, it should be possible to use a statistical analysis to separate the effect of available sites and the energy required to activate a site at the yield point. To verify that the sample sets are statistically unique, Wilcoxon–Mann–Whitney rank sum tests were applied to the data. P values between data sets for the different orientations generated by different tips were generally below 0.01, indicating a greater than 99% probability that the data are unique. By examining Figure 2.3, there is a

distribution in maximum pressure required to initiate plastic deformation, a trend consistent with other works;[31–33] Figure 2.6 plots the pressure range (p_{max}–p_{min}) as a function of the measured average instantaneous tip radius for each grain orientation. As noted by Li et al.,[23] the cumulative fraction of events curve will maintain a smooth sigmoidal shape when only a single type of defect is sampled. Using this definition, the data presented in Figure 2.4 appear to indicate that only a single defect type is responsible for these measured events. In that case, the variation in pressure or stress at a yield event is most likely controlled by the spatial distribution of defects under the indenter tip. This variation could be examined in a variety of ways, ranging from standard deviation to total range of measured data, to a fraction of the range of measured data (i.e., 20–80%), to a value such as the coefficient of variance. For the purposes of this study, we have selected the total range of event data, but the trends indicated by this would be supported by any of the aforementioned measures of variation in measured data. The greatest effect of pressure range is evidenced in the (111) oriented grain, where the increase in tip radius shows a marked decrease in the pressure range. Michalske and Houston[30] saw a similar decrease in shear stress with increasing tip radius. Conversely, the (001) grain shows a minimally increasing trend with tip radius. It is important to note in this analysis that p_{min} is relatively unresponsive to orientation within a specific tip geometry but highly responsive to changing tip radius. These trends support the proposition that the (111) oriented plane is more sensitive to defects than the (001) oriented planes. As tip radius increases, sampling volume increases, and the likelihood of probing a single defect decreases, thereby decreasing the range of pressures, which initiate plasticity, and defining the minimum pressure required for yield.[34]

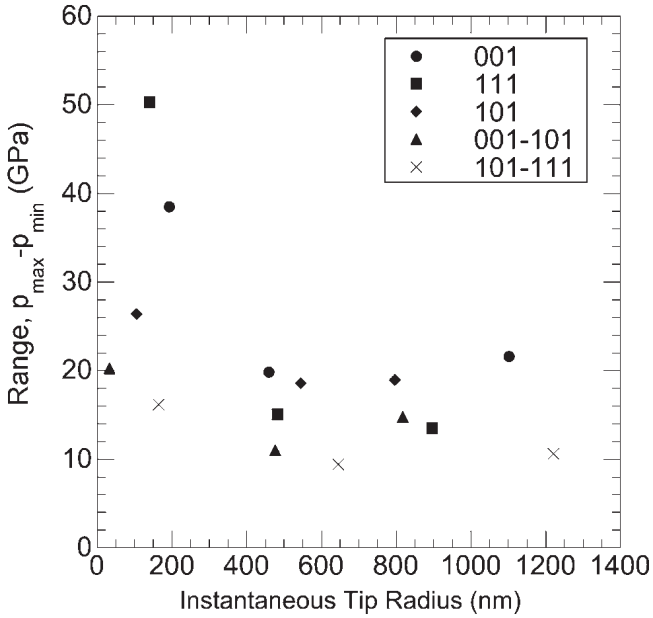

Figure 2.6 Range of pressures required to initiate plastic deformation as a function of instantaneous tip radius. The pressure range (p_{max}–p_{min}) is used as a measure of the variation in spatial distribution of defects beneath the indenter tip. This measure is used since the shape of the cumulative fraction curves indicate that the same type of defect is sampled in each case.

2.4.3 Activation Volume Analysis

The energy required to activate a defect site during nanoindentation can be determined by evaluating the cumulative distribution of maximum pressures associated with the initial yield point. The rate of dislocation source activation in a unit volume of material subjected to a pressure p_0 has an Arrhenius-type relationship and can be written:

$$\dot{N} = \dot{N}_0 exp\left[-\frac{\varepsilon - 0.31 p_o v^*}{kT}\right], \quad \text{Equation 2.8}$$

where $\dot{N}_0$ is the pre-exponential constant "attempt frequency," v^* is the activation volume, e is the intrinsic nucleation energy barrier, and kT is the thermal energy. Since the nucleation of dislocations is a stress-induced process, Equation 2.8 is generally presented in terms of the maximum shear stress, τ. However, $\tau = 0.31 p_0$, thus Equation 2.7 can be

written as shown above. The cumulative distribution of pressures at yield for indentations in two representative grain orientations for all three tips is shown in Figure 2.4. This plot illustrates the strong radius dependence, with a noticeable increase in pressures between the blunt tip (Berkovich) and the sharpest tip (cube corner) and indicates orientation dependence, as evidenced in Figure 2.3. As described by Schuh and Lund,[10] if we recognize that there is only one initial yield point allowed per indentation, the population of indentations available to yield is equal to 1-*f*. Then, a differential equation describing the population in terms of activation rate can be expressed as:

$$\dot{f} = (1 - f)\dot{N}. \qquad \text{Equation 2.9}$$

To obtain the unknown parameters of Equation 2.8, a linear least squares fitting technique is applied. Figure 2.7 is a plot of $\ln(\ln(1\text{-}f)^{-1})$ as a function of $0.31p_0$ and the data are curve fit using a linear regression; therefore, the slope of the line is v^*/kT, and the intercept is the ln(η), where $\eta = \dot{N}_0 \exp\left(-\frac{\varepsilon}{kT}\right)$, or the rate at which defects would nucleate due to thermal activation alone. The values of v^* for each orientation for all three tips are tabulated in Table 2.1; activation volume decreases with decreasing tip radius. Additionally, the maximum shear stress tends to increase as the tip radius decreases for all orientations except the (001)–(111) grain. If homogeneous dislocation nucleation is the active mechanism in this case, one would expect that a smaller volume under a higher stress was needed to create a new dislocation. However, the volume determined is significantly smaller than one would expect for a dislocation loop, so it is the magnitude, not the trend, which implies that the mechanism in this case is not homogeneous dislocation nucleation.

Table 2.1 Activation volumes (in nm^3) normalized by Burgers' vector (b_{Ni}=0.248nm) calculated from least squares fitting of Equation 2.8 for each sampled orientation and tip geometry, and maximum applied shear stresses in (GPa) for each case. The (001) and (111) data was collected from two grains with the same nominal orientations, while the other three orientations included data from only one indented grain.

	(001)		(111)		(101)		(001-101)		(001-111)	
	V	τ_{max}	V	τ_{max}	V	τ_{max}	V	τ_{max}	V	τ_{max}
1300 nm	$0.32b^3$	3.06	$0.37b^3$	1.92	$0.38b^3$	2.52	$0.38b^3$	2.22	$0.57b^3$	2.21
1000 nm	$0.31b^3$	3.06	$0.29b^3$	2.56	$0.35b^3$	2.82	$0.29b^3$	1.77	$0.32b^3$	1.70
100 nm	$0.16b^3$	4.21	$0.12b^3$	4.90	$0.10b^3$	6.71	N/A*	N/A*	$0.15b^3$	1.61

For propagation, rather than nucleation, in a pure shear condition, one would not expect a yield point. However, since the dislocations sampled by the stress field are likely not perfectly located symmetrically under the indenter tip, the most likely way to cause a loop to expand is to require an activation event to occur once the entire loop is at a stress high enough to move the dislocation. For instance, a kink or double kink (on the order of fractions of a Burgers' vector) on the portion of the loop furthest from the indenter could be the critical activation event needed to start the loop growing, assuming that the double kink separation distance is on the order of the Burgers' vector. Since the region of the dislocation loop closest to the indenter would be overdriven, the activation of a double kink could then lead to the rapid expansion of the dislocation loop, rather than a smooth propagation that one might expect for a uniformly applied shear stress. It should be noted that the activation volume is not related the volume under the tip, which is undergoing shear stress; however, in these cases, they indeed are both smaller for the smaller radius tips.

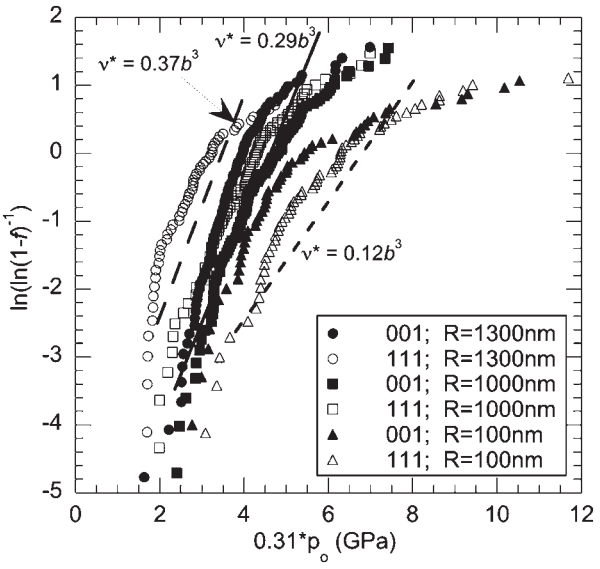

Figure 2.7 Data used for linear least squares fitting to determine activation volume. Data presented are compiled from two sets of two indented grains with the same nominal orientation. Heavy straight lines are examples of fits and the accompanying activation volume value, which is normalized by the Burgers' vector.

2.5 Conclusions

The effects of crystallographic orientation and indenter tip radius were investigated through EBSD and nanoindentation of commercially pure Ni200.

1. An orientation effect is observed in yield pressure for the onset of plasticity in Ni. Yield occurs at generally higher loads in the (001) oriented grain than in the (110) or (111) grains when indentation is performed with a relatively blunt (1300 nm) radius indenter tip.
2. The effect of tip radius can overshadow the orientation effect, as the 1300-nm radius tip is more sensitive to orientation than either the 1000- or 100-nm radius tips. However, the sharpest tip appears to be most sensitive to individual defects.

3. The observed indenter radius effect on the onset of plasticity is likely due to the presence of defects rather than a fundamental size effect. The initial dislocation density is sufficiently high to result in an interaction between the stress field beneath the indenter tip and a dislocation even at very low loads and shallow indentation depths.
4. The activation volume for incipient plasticity, using a cumulative event fraction analysis, suggests that larger tips require activating a larger volume of material. However, since this occurs at a lower stress than the smaller tips, the logical feature being activated in this case is a dislocation loop rather than an atomistic-level defect. This does not preclude an atomistic event being the critical feature in expanding a dislocation loop but instead suggests that the activation volume analysis alone cannot distinguish between nucleating a new dislocation and an atomistic process expanding an existing loop.

In summary, we have shown an orientation dependence of the onset of plastic deformation processes as well as a pronounced tip radius effect, likely the result of an interaction between an existing dislocation and the stress field produced beneath the indenter tip.

CHAPTER 3. STATISTICAL QUANTIFICATION OF THE IMPACT OF SURFACE PREPARATION ON YIELD POINT PHENOMENA

Previously published by Metallurgical and Materials Transactions: A, *Volume 45, pages 4307-4315, in September 2014.*

3.1 Introduction

During nanoindentation testing, a distinct excursion in the load-displacement curve at the transition from recoverable elastic to plastic deformation is often observed. First identified by Gane and Bowden,[35] this phenomena is known as a yield point or "pop-in" event. Yield point phenomena have been extensively studied and have been found to correlate with oxide film fracture,[8] dislocation source activation,[15] or homogenous dislocation nucleation,[9,10,36] depending on the pre-existing dislocation density.

For metals, the near-surface dislocation density of a particular specimen is often governed by sample preparation. It is well established that the occurrence of abrupt elastic-plastic transitions causing yield points can be greatly reduced when the surface of a metal is mechanically altered.[7,31,37–39] Oliver and Pharr[7] demonstrated that yield points occur regularly on electropolished tungsten surfaces but are completely absent when the surface is prepared by standard mechanical metallographic techniques (i.e. mechanical grinding and polishing). In light of similar results garnered by other investigations in materials with a variety of crystal structures[31,38–40], the elimination of a distinct yield point is generally thought to result from the introduction of near-surface dislocations

during mechanical polishing. Activation of pre-existing dislocations, rather than nucleation of new ones, enables incipient plasticity at much lower applied stresses[2] and generally causes a smooth transition in the load-displacement record of a nanoindentation. Due to the lack of quantification regarding the effect of surface preparation on yield point phenomena, Wang et al.[41] recently evaluated the indentation response of Mo when mechanically polished, chemo-mechanically polished, and electropolished. The authors found that mechanical polishing eliminated all yield points; subsequent colloidal silica polishing removes enough of the mechanical damage to achieve some yield points, but never fully returns the surface to the pristine state achieved with electropolishing.

The effect of dislocation density on incipient plasticity has also been investigated for FCC materials.[42,43] Shim et al.[43] determined that the stress required to initiate plasticity in single crystal Ni is lower when the crystal was pre-strained 10% and 20% than in the as-annealed condition. They also found that the shear stress at yield decreased as indenter radius (stressed volume) increased. Thus, the authors suggest that when the indenter radius is smaller than the dislocation spacing, the probability that the stressed volume contains a dislocation is low, requiring a high shear stress to initiate plasticity. Conversely, the stress required decreases when the indenter radius is larger than the dislocation spacing because the probability that a dislocation exists in the stressed volume is high. Similarly, varying surface preparation may result in a changing dislocation density leading to a measurable variation in yield behavior.

Surface ablation using energetic ions can be used as an alternative method to mechanical polishing or electropolishing in the preparation of micro- and nanomechanical specimens. Techniques such as focused ion beam (FIB) milling, result in

extensive surface damage from bombardment with high-energy gallium ions[44–47] and FIB damage has previously been shown to introduce damage that eliminates yield point behavior in metallic solids during nanoindentation.[47] Conversely, ion polishing, which involves bombarding a surface with low energy argon ions, is generally thought to result in less surface damage than FIB.[48,49]

Using orientation imaging microscopy (OIM) to analyze backscattered electrons, the crystallographic orientation of each point in a sampled material is indexed and the quality of the Kikuchi pattern is analyzed. The image quality (IQ) parameter describes the quality of an EBSD pattern; the perfection of the crystal lattice in a sampled volume is a main factor affecting the IQ. Distortions caused by lattice imperfections will result in more diffuse diffraction patterns and reduce image quality. Thus, IQ data can be used to obtain a qualitative description of local strains in a microstructure.[50] Local misorientations can be further characterized using a kernel approach, based on a user-defined area. The kernel average misorientation (KAM) is related to lattice curvature, which is a result of local variation in lattice orientation, and is a parameter that requires a certain number of geometrically necessary dislocations (GNDs). Because of this relation, KAM can, to first order, be used to estimate relative dislocation densities by assuming the ratio of GNDs is proportional to the total dislocation density. Previous investigations using KAM as a first order measurement of local misorientation, θ, approximated GND density from:

$$\rho_{GND} = \frac{2\theta}{ub}, \quad \text{Equation 3.1}$$

where *b* is the Burgers vector and *u* is the unit length. In this approximation, a GND array is defined for simple cylindrical torsion following the method of Calcagnotto et al.[51] and Kubin and Mortensen.[52] This array, based on strain gradient theory,[53] assumes a series of twist subgrain boundaries in the cylinder each containing two perpendicular arrays of screw dislocations. When combined, IQ and KAM data can be used to qualitatively assess the changes in defect densities as a function of material preparation technique.

The current study will investigate the relative effects of surface damage caused by conventional metallographic sample preparation methods on indentation-induced yield point phenomena in Ni. The sample preparation methods to be considered are chemo-mechanical polishing, electropolishing, and ion polishing. The magnitude of structural defects caused by these sample preparation techniques will be estimated using a combination of IQ and KAM data and the Taylor relation. Finally, the yield behavior will be related to the defect density using a statistical approach to account for the similarity between the volume of material sampled in the nanomechanical test and the representative volume of the spatially distinct defects.

3.2 Experimental Procedures

3.2.1 Surface Preparation Techniques

A sample of commercially pure (99.5%) nickel 200 (hereafter Ni200), approximately 13 mm in diameter and 2 mm thick was prepared by cutting, rolling to 20% deformation, and annealing in air at 1150 ^{o}C for 24 hours followed by air-cooling to generate large (0.5 mm-scale) grains. The sample was sequentially polished using three different techniques: (1) chemo-mechanical polishing, (2) electropolishing, (3) ion

polishing, and indented in each polishing condition. First, the sample was mechanically ground through 1200 grit silicon carbide grinding papers and polished with 3 μm and 0.5 μm diamond compound on a flat nylon cloth, and finally vibropolished with 0.02 μm colloidal silica suspension. Atomic force microscopy (AFM) was used to measure an average surface roughness, *Ra*, at each surface preparation condition. In the mechanically polished condition, the measured *Ra* was 1.8 nm±0.5 nm over a 10 μm square scan. The second surface condition was then achieved with electropolishing in a solution of 37% H_3PO_4, 56% glycerol, 7% H_2O. This procedure etched the top few tens of microns of material, thereby effectively removing both residual damage from mechanical polishing and the plastic zone formed by the nanoindentation of the mechanically polished surface. The measured *Ra* roughness of the electropolished surface was 1.7 nm±0.4 nm. The final surface preparation condition was achieved by ion polishing for one hour at 4 kV discharge voltage, 6 kV accelerating voltage, and an argon ion current of approximately 130 μA using a Hitachi Model E-3500 cross section ion polisher. Argon ions impinged perpendicular to the sample surface. Ion polishing removed approximately 500 nm of material. AFM was again performed; the *R*a roughness was 1.3 nm±0.5 nm in the indented grain, while the *Ra* roughness in the innermost damage ring, where the ion beam was most intense, was 15.1 nm±0.8 nm. An optical micrograph and a schematic of damage zones are shown in Figure 3.1a and b.

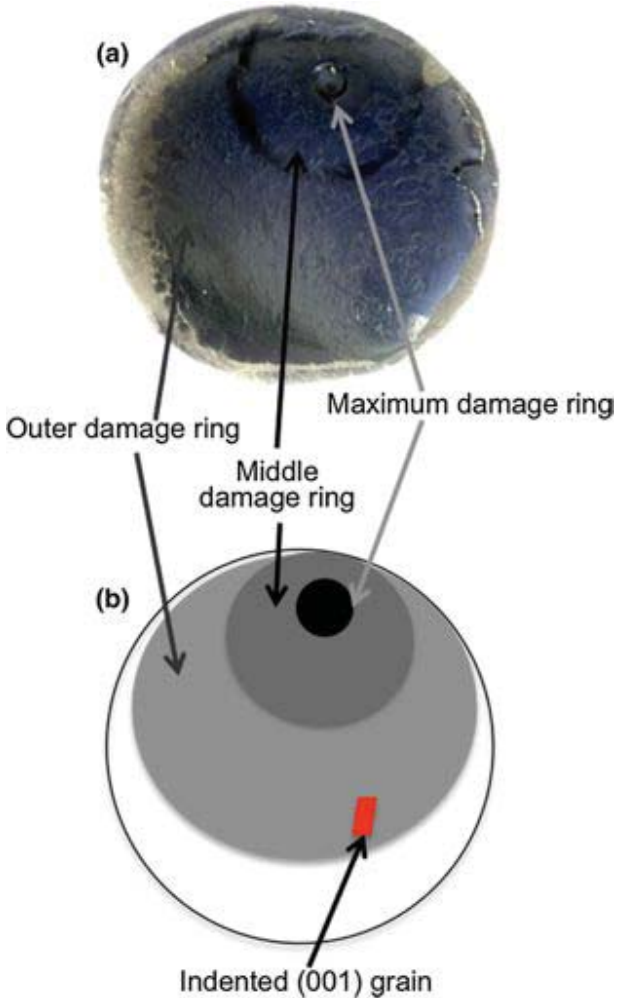

Figure 3.1 Damage zones induced by ion polishing are shown in an optical micrograph of Ni200 sample (a) and represented as a schematic (b) with the approximate location of the indented grain identified. The diameter of the Ni sample is 13 mm.

3.2.2 Grain Identification and Nanoindentation

In order to identify a grain suitable for indentation, EBSD data were obtained using orientation image microscopy (OIM) DC 5.3 software from TSL, with an FEI Sirion field emission scanning electron microscope at 20 kV. Figure 3.2a shows a typical orientation map obtained via a Hough-based EBSD analysis of large area (~1 mm x 2

mm) scans utilizing 4 x 4 detector binning and a hexagonal grid with a step size of 5 or 10 μm. The large (001)-type grain identified in Figure 3.2a was selected for indentation. Nanoindentation of this (001)-type grain was performed at each surface preparation condition using a Hysitron Triboindenter equipped with a Berkovich tip of nominal radius ~1300 nm. The effective tip radius was determined by performing a Hertzian analysis of fully elastic indents made in single crystal W. Twenty-five indents, arrayed in a square, were performed in the chosen grain. A five segment, partial-unloading load function was used with peak loads ranging from 250 μN to 7000 μN. All indentations were separated from one another by 15 μm; the largest plastic zone radius generated was 3 μm, ensuring no previous indentation influenced a subsequent indentation. Indents were placed at least 50 μm away from the grain boundaries visible on the exposed surface. Some of the indent arrays are visible in the optical micrograph of the (001)-type grain shown in Figure 3.2b.

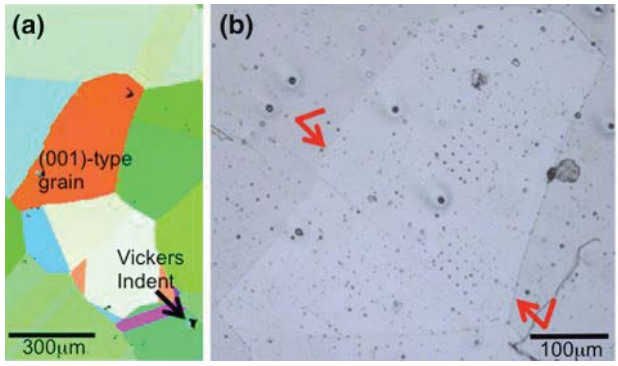

Figure 3.2 Orientation map (a) generated from EBSD data showing the (001)-type grain indented for this study. Optical micrograph (b) of the ion polished sample surface showing the indented (001)-type grain with visible 5 x 5 square arrays of nanoindents. Red arrows indicate approximate location of grain width measurements used to generate Figure 3.3.

EBSD was also used to determine whether sub-surface grain boundaries influenced properties measured with nanoindentation. Grain shape was verified and grain size was measured at each surface preparation condition, and it was found that the grain width increased as material was removed from the surface. Thus we assume that a grain boundary does not run parallel to the indented surface at a distance that would affect measured properties. A schematic of the probable grain boundary location relative to the initial sample preparation surface is shown in Figure 3.3. Additionally, indent arrays conducted on each newly polished surface were placed 125 μm from the locations of any previous arrays.

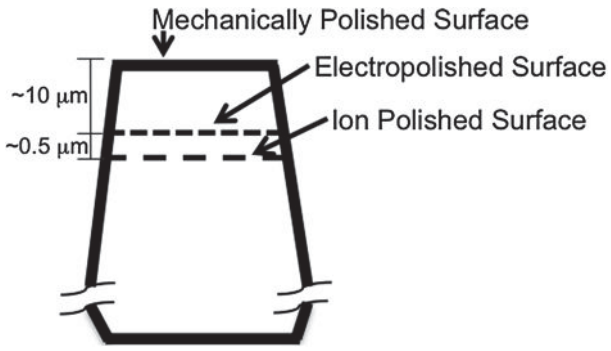

Figure 3.3 Schematic showing possible grain shape normal to the indented surface; the schematic cross section was developed from grain width measurements which are indicated in Figure 3.2(b).

3.2.3 GND and Total Dislocation Density Estimation

Two methods were employed to evaluate the change in near-surface dislocation density among a chemo-mechanically polished surface, an electropolished surface, and an ion polished surface. First, image quality (IQ) and kernel average misorientation (KAM) were determined using the EBSD data. The KAM quantifies the average misorientation

around a point with respect to a set of nearest neighbor or second-nearest neighbor points.[51] For any given pixel *i*, the kernel average misorientation is obtained from:

$$KAM(i) = \frac{1}{K}\sum_k \omega_{ik}, \quad \text{Equation 3.2}$$

where *K* is the number of pixels around pixel *i* and ω_{ik} is the minimum misorientation angle between pixels *i* and *k.* In this work KAM was determined using first near neighbor pixels, with a maximum allowable misorientation value of 5° to be considered as part of the same grain.[54,55] Values above this threshold are assumed to belong to subgrains or an adjacent grain and are thus excluded from the calculation.

Because KAM is a measure of local lattice curvature it does not take into account the statistically stored dislocation (SSD) density. However, the total dislocation density ($\rho_T = \rho_{GND} + \rho_{SSD}$) can be approximated using the Taylor relation:[56]

$$\tau = \alpha G b \sqrt{\rho_T}, \quad \text{Equation 3.3}$$

where α is a numerical constant (typically ~0.4), *G* is the shear modulus of the material (80 GPa for Ni), and *b* is the Burgers vector (0.248 nm for Ni). Shear stress, τ, is 1/6 of the hardness, assuming the Tabor relationship, $\tau = \sigma_y/2$ and $\sigma_y = H/3$,[57] where σ_y is the uniaxial yield stress. For this calculation, hardness was determined by measuring the change in projected area of a Vickers indent at each polishing step and has units of GPa.

3.3 Results

3.3.1 Defect Density

Previous work suggests that defect density is influenced by material processing as well as surface preparation. Common defects include vacancies, stacking faults, impurities, and surface asperities. However, because of the long annealing and slow-cooling cycle applied to the Ni sample, vacancies and stacking fault tetrahedra are unlikely to be present in significant quantities. Impurities may play a role, but it is likely minimal, because the sample is commercially pure and composition should be independent of orientation. The interaction of dislocations with impurities in Ni200 would lead to local strain hardening, as observed by nanohardness testing. Surface asperities are also unlikely contributors as the measured surface roughness is low. The most likely subsurface defects in the material tested in this experiment, then, are dislocations.

The image quality and kernel average misorientation analysis suggests that local lattice curvature increases from the electropolished surface to the ion polished surface. It is likely that GND density also follows this trend. Figure 3.4a-c presents IQ maps obtained for each surface preparation condition. Darker grey shades in the maps denote lower IQ values. The IQ map of the electropolished surface has only slight grey-scale gradients, suggesting that the overall image quality is high; local grey-scale variations increase for the mechanically polished surface indicating a higher degree of lattice imperfections near the surface. The IQ decreases substantially for the ion polished surface suggesting that this technique imparts additional defects into the microstructure, increasing overall lattice imperfections.

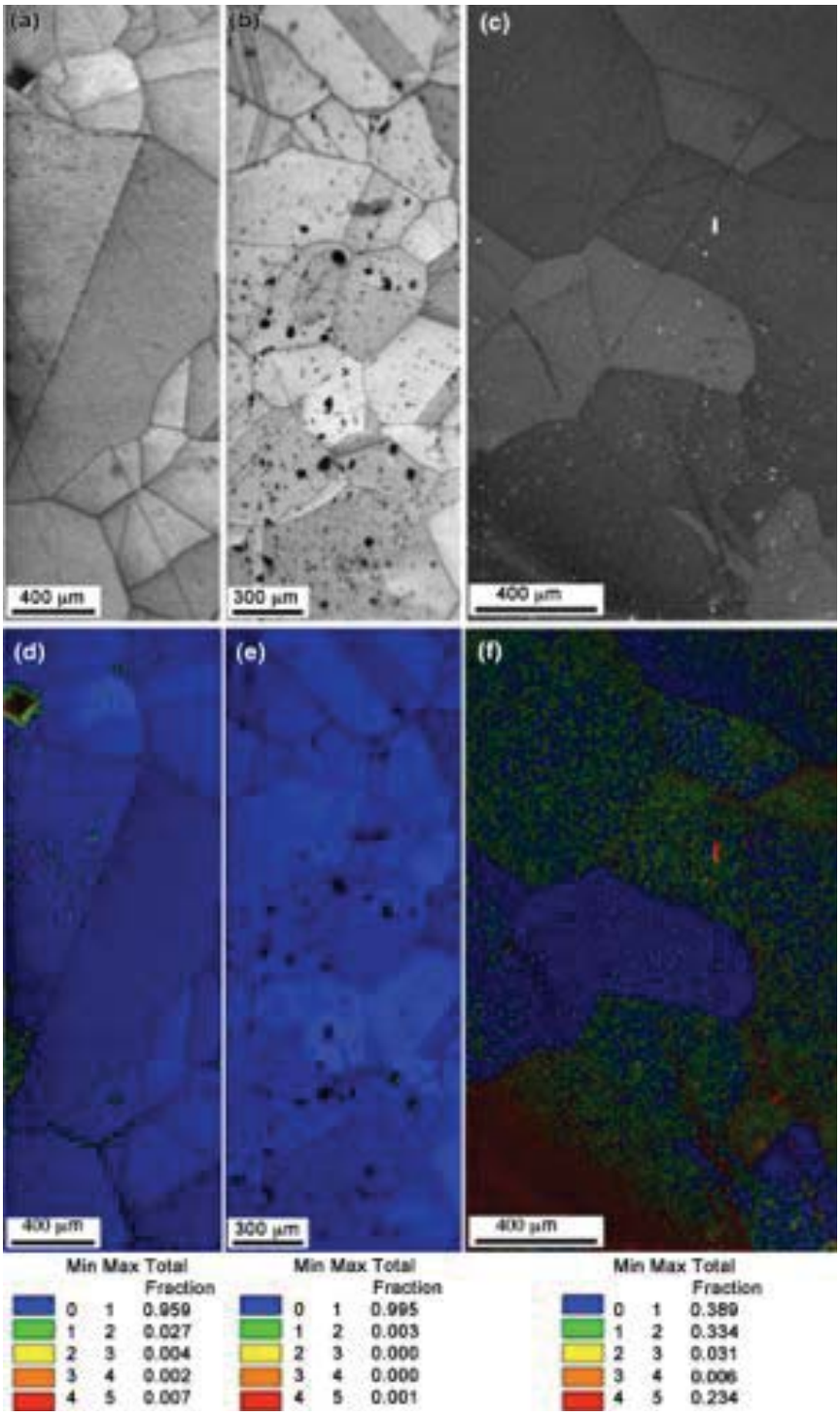

Figure 3.4 Image quality maps (a) through (c) and KAM maps overlaid on IQ maps (d) through (f) for electropolished, mechanically polished, and ion polished surfaces, respectively. Colored scales corresponding to the fraction of misoriented points are shown below their respective KAM maps.

Kernel average misorientation data can be combined with IQ maps to further assess changes in local lattice misorientation as a function of surface condition. Figure 3.4d-f shows the IQ maps overlaid with KAM data for the three conditions. The fraction of points with a misorientation between 0-1^{o} (blue points) decreases from the electropolished condition to the ion polished condition, suggesting that surface preparation techniques that result in additional lattice imperfections also result in a higher degree of local lattice curvature, which may be attributed to an increasing density of GNDs. The mechanically polished surface appears to have a higher fraction of points with 0-1^{o} misorientation than the electropolished surface, however this is likely a function of the step size used to collect the patterns. The patterns for the mechanically polished surface were collected using a 5 μm step size, while a 10 μm step size was applied to the electropolished surface. When applied to the same sampled area, larger step sizes have been shown to make the KAM appear worse.[58,59] This has been confirmed in this study by conducting EBSD scans on the ion polished surface at both 5 μm and 10 μm; the fraction of 0-1^{o} misorientations decreases when the step size is doubled. The step size effect may contribute to the apparent increase in local misorientation for the electropolished surface when IQ results suggest that this surface preparation results in fewer overall lattice imperfections. In sum, the combination of IQ and KAM data suggest that lattice imperfections and local misorientation, which is related to GND density, increase from an electropolished surface to an ion polished surface.

The Taylor relation estimation also indicates that bulk dislocation density is a function of surface preparation condition. Given the nature of indentation size effects, and because the Tabor relationship may not accurately capture the dislocation density of

the as-polished surface, these estimates will be upper bounds of dislocation density, since measured hardness decreases with increasing depth.[60,61] Increasing calculated dislocation density is observed from the electropolished and mechanically surfaces to the ion polished surface.

3.3.2 Yield Behavior

An optical micrograph of the as-ion polished and indented Ni200 sample highlighting the selected (001) grain is presented in Figure 3.2b. By testing the same (001)-type grain in each condition, the effect of defect density on yield behavior, independent of grain orientation, is obtained for three distinct surface preparation conditions. Representative load-depth curves generated by nanoindentation of the selected Ni200 grain for each surface preparation condition are shown in Figure 3.5a; initial yield point or 'pop in' events are magnified in Figure 3.5b. The load and depth at yield is recorded for each surface condition. Hertzian contact mechanics[18] can then be used to transform the data to units of stress, or pressure, for further analysis. To first order, the maximum pressure (p_o) under the indent at yielding can be estimated with:

$$p_o = \frac{3P}{2\pi a^2} = \left[\frac{6PE^{*2}}{\pi^3 R_i^2}\right]^{1/3}, \qquad \text{Equation 3.4}$$

where a is the contact radius, which can be rewritten in terms of reduced modulus, E^*, and instantaneous tip radius, R_i. For this analysis, the average measured indentation modulus, E^*, for the (001) type grain was used, derived from a classical Oliver-Pharr

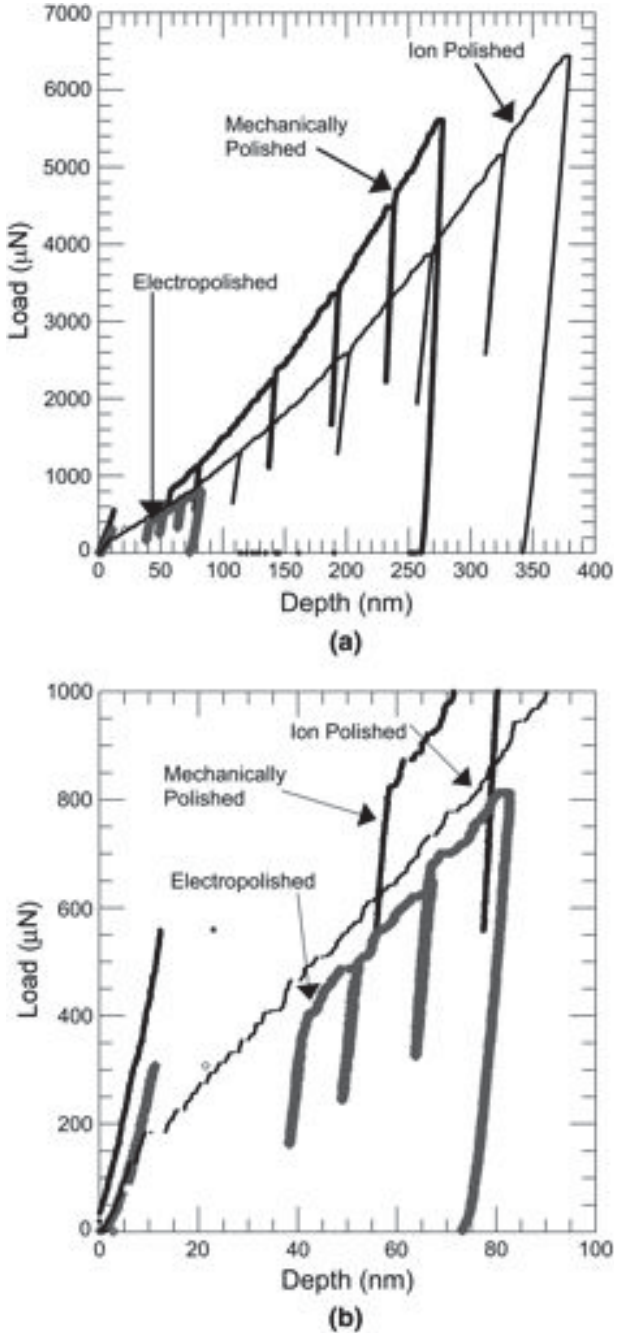

Figure 3.5 Representative load-controlled nanoindentation load-displacement curves from Ni200 with three surface preparations (a). A magnified view of typical pop-in events during the initial transition from elastic to plastic deformation is shown in (b). These curves were chosen to depict typical pop-in events rather than typical mechanical property measurements.

approach.[7] By using the load, P, and depth, δ, at the onset of yielding, the following calculation for instantaneous tip radius, R_i, represents the radius of the indenter at the moment of pop in,

$$R_i = \frac{9P^2}{\delta^3 16E^{*2}}. \quad \text{Equation 3.5}$$

Estimating the instantaneous radius in this way provides a first order method to account for the non-spherical shape of the Berkovich indenter tip. Additionally, Hertzian approximations are only valid for small strain criteria and can underestimate the stress field beneath an indentation.[12,14] Therefore, only yield-points with contact depths less than *R/3* were used for yield pressure calculations, ensuring that the low strain approximation is reasonable.

A cumulative fraction of events analysis was used to compare the distribution of yield pressures as a function of surface condition. Figure 3.6 shows typical p_o results for indents performed with a Berkovich indenter. For this type of analysis, a vertical line would represent perfectly reproducible results, while any variability in the data results in a wider range of pressures to achieve a cumulative distribution of one. Non-parametric statistics can be used as a quantitative measure of similarity between yield distributions.[62] The Kolmogorov-Smirnov (KS) test attempts to determine if two continuous, one-dimensional, non-parametric probability distributions differ. The test reports a p-value; small values indicate the null hypothesis (that the distributions are equal) should be rejected. When applied to the current yield distributions, the KS tests result in p-values between data sets on the order of 0.01, indicating the null hypothesis should be rejected,

these data imply that the distribution in yield are statistically different between sampled conditions.

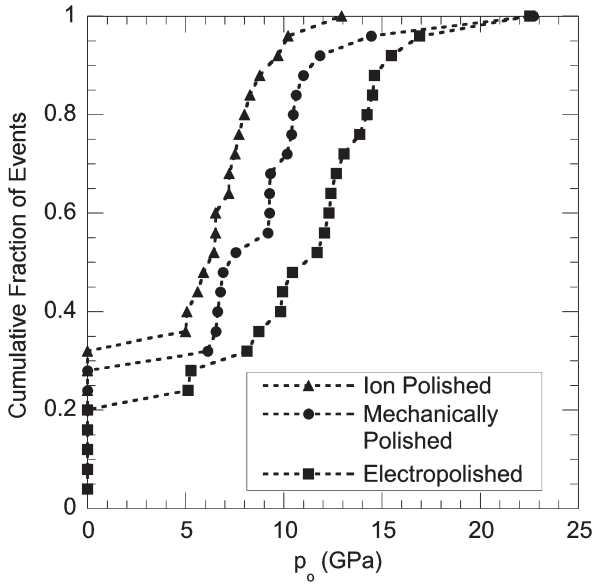

Figure 3.6 Cumulative distribution functions showing yield behavior for all three surface preparation techniques. Indents which did not exhibit a pop-in (p_o = 0 GPa) appear on the plot along the y-axis.

Since the yield pressure distributions are unique, comparing extreme values and trends should provide insight into yield mechanisms. In general, the largest pop-in pressures are achieved when indenting the electropolished surface, while lower maximum yield pressures occur for the ion polished surface. Decreasing yield pressure correlates with increasing near-surface dislocation density. Additionally, the measured hardness, *H*, determined using the classical Oliver-Pharr method,[63] increases with increasing amounts of surface damage. The electropolished sample displayed the lowest apparent hardness while the ion polished sample resulted in the highest apparent hardness, shown in Table 3.1. Near-surface dislocation networks likely result in local hardening, thereby increasing

apparent hardness. These networks may also act as dislocation sources, contributing to changing yield behavior.

Table 3.1 Nanoindentation hardness, H, calculated with the Oliver and Pharr Method, dislocation densities, ρ_{dln}, estimated from bulk hardness, mean yield pressures, p_{mean}, fraction of indentations that exhibited a measurable yield point, f_v, fraction of points with 0 to 1° misorientation determined by KAM analysis, and coefficient of variance, C_v, as a function of surface preparation technique.

	H (GPa)	ρ_{dln} (m^{-2})	p_{mean} *(GPa)*	f_y	*KAM Fraction*	C_v
Electropolishing	2.03±0.45	$7x10^{13}$	12.34	0.80	0.955	0.326
Mechanical Polishing	2.17±0.56	$8x10^{14}$	9.30	0.72	0.994	0.387
Ion Polishing	2.51±0.61	$1x10^{15}$	7.21	0.68	0.389	0.268

3.4 Discussion

3.4.1 Dislocation Density and Yielding

Figure 3.6 shows that the minimum yield pressure converges to a value of ~5 GPa for all surface preparation conditions. This minimum pressure, p_{min}, of ~5GPa is likely not an effect of surface dislocation density due to sample preparation. When the fraction of indents that do not show a distinct yield point is considered it could be inferred that instrument resolution may preclude the detection of pop-in events occurring at pressures much lower than 5 GPa. Nevertheless, in any indentation experiment there will exist a minimum critical yield pressure. This critical yield pressure will be dictated by proximity of a pre-existing dislocation to the indenter stress field. For this study, we assume plasticity is initiated by the activation of a pre-existing dislocation, rather than by dislocation nucleation. Because the indenter tip is blunt, the stress field beneath it is large, thus the probability that the stress field interacts with a pre-existing dislocation is a

function of the dislocation density.[43] Yield will occur at the critical pressure when a pre-existing dislocation is either shaped or spatially oriented such that it can be activated with a minimum applied stress.

Beyond the critical yield pressure and detectable p_{min}, higher pressures are required to cause yielding; in this situation, we assume that a critical resolved shear stress condition must be met locally to activate an existing dislocation source at some position under the indenter. However, this position, relative to the indenter surface, may not be the same when comparing different indentations. Once the critical shear stress is achieved, the dislocation loop expands rapidly resulting in pop in. Since the overall stress field around the indentation is typically higher than the stress required to maintain slip, the spatially resolved discrete dislocation that is activated continues to move away from the adjacent high-stress region, producing extensive plastic deformation under the indent and contributing to the range of yield pressures observed in Figure 3.6.

Of the three sample preparation methods tested, the electropolished sample required the highest pressure to initiate plastic flow (Figure 3.6). This suggests there is a low probability that a dislocation exists in the region beneath the indenter under the highest stress.[64] The electropolished surface has the lowest inferred initial dislocation density (Table 3.1), resulting in the lowest probability that a dislocation will be spatially oriented for activation at low pressures or small contact areas. The mechanically polished surface has a higher inferred initial dislocation density, resulting in a higher probability that a mobile pre-existing dislocation will be located in the high stress region. In this case, the average barrier for yielding decreases and typically lower pop-in pressures are recorded than for the electropolished surface. With the highest surface dislocation density,

the ion polished surface accommodates plastic deformation most easily. Multiple mobile dislocations likely exist in the indenter stress field and are easily activated. Additionally, the range of pressures that cause yielding (i.e. p_{max}-p_{min}) decreases with increasing defect density, suggesting that a decreasing pressure range corresponds with a lower likelihood of probing a single defect. The pressure range is indicative of the spatial variation of defects in the sampled volume.[64]

The calculated variation in maximum yield pressures, p_{max}, for the three conditions also suggests changes in the local deformation conditions. There is no statistically significant variation between p_{max} for the electropolished and mechanically polished samples. This indicates that maximum yield pressure is not a function of surface dislocation density but likely approaches the theoretical shear strength of the crystal, where dislocation nucleation, not activation, dominates the slip behavior.[20,29] The results from electropolished and mechanically polished samples agree with the theory of Wang et al.[41] that chemo-mechanical polishing with colloidal silica returns the surface to a near-electropolished state. In contrast, the recorded p_{max} for the ion polished surface is substantially lower, suggesting slip depends on surface defects generated during ion polishing rather than on intrinsic dislocations. If other defects, such as subsurface ion damage or surface asperities, interact with the indenter the material may yield at lower pressures. Measured roughness does not differ greatly among the three surface preparation conditions in the selected (001)-type grain. Since the asperity concentration is relatively constant, ion polishing likely creates other subsurface defects, such as those caused by ion damage, which can lower the stress needed to initiate plasticity. In fact, the generally smooth sigmoidal distributions observed for mechanically and electropolished

surfaces suggests that the same type of defect causes yield in both cases.[23] The yield point distribution for the ion polished surface is generally steeper and has less curvature than the mechanically and electropolished data, which may suggest that ion damage-induced defects may contribute to yield behavior.

3.4.2 Coefficient of Variance

As discussed above, the stochastic nature of the yield point phenomena observed during nanoindentation may be due, in part, to the likelihood of the indent interacting with a dislocation, which is directly related to an increased surface dislocation density from sample preparation.[34,41,65] This is not only true for nanoindentation; similar results have been seen for compression tests in sub-micron scale samples,[66] suggesting that any localized measurements of mechanical properties must be addressed in a statistical manner. Reports addressing this methodology in indentation[65,67] suggest that, when the sampled volume is much smaller than the defect density, as in the case of the ion polished surface, the yield behavior will have a small variation around a low mean value, representing the stress to activate existing defects. When the sampled volume is much larger than the defect density, as in the case of the electropolished surface, the yield behavior will have a small variation around a high mean value representative of the ideal flow strength of the material. When the sampled volume is on the order of the defect density, the variation in the measured flow strength is greatest, and will be centered on a mean that is between both extremes. This type of situation would be represented by the mechanically polished condition. For the current study the instantaneous tip radius at the yield point was between 1100 nm and 1250 nm; suggesting the volume of material

sampled in each case is effectively constant. Therefore, changes in defect density should impact both the mean and the variation. One way to quantify this behavior is the coefficient of variance, C_v, in yield pressure:

$$C_v = \frac{\sigma}{p_{mean}}, \quad \text{Equation 3.6}$$

where p_{mean} is the mean yield pressure and σ is the standard deviation of pressure. C_v is expected to be highest at intermediate defect densities and lower at the extremes. The coefficients of variance, as well as the standard deviations and mean pressures, follow this general trend. The same trend can be extracted from published data where applied load was varied while the size of the indenter remained nominally constant,[65] as well as from experiments in which the size of the indenter was varied on a fixed defect density.[64,67] While these data are not conclusive, they indicate that any predictive model addressing small-scale mechanical behavior should capture a similar trend in coefficient of variance.

Examining Table 3.1 shows several trends that may be useful for determining appropriate experimental conditions for assessing stochastic mechanical performance of materials. First, the dislocation density (as inferred from hardness once a well established plastic zone exists via the Taylor model) corresponds with the fraction of indentations that exhibit a yield point and the mean pressure at yield. Secondly, the KAM measurement of local lattice curvature (a point to point variation) roughly corresponds with the coefficient of variance in the yield point data. The combination of examining both the mean values of pressure and a measure of stochasticity can be used to select appropriate experimental methods that move towards validation of predictive materials

simulations. For instance, the radius of the indenter tip may be selected when performing nanoindentation; examination of a set of preliminary data that produces a high mean pressure but also a high C_v would suggest that a sharper tip would be more likely to probe the defect free region of the sample. These findings could be extended to a micro-pillar compression experiment where the volume of material under stress can be selected and defect density may be controllable by manufacturing method (deposited pillars should have a lower defect density than FIB-machined pillars). A test resulting in a high C_v would imply that a sampled volume on the order of the spacing between dislocations would be likely to generate stochastic results, while a more deterministic value of dislocation nucleation would occur if the sampled volume is much larger than the dislocation spacing.

3.5 Conclusions

Nanoindentation has been used to examine the effect of three specific surface preparation methods on the yield behavior of an FCC metal. Evaluation of the maximum pressure required for yield indicates that ion polishing likely causes the formation of additional near-surface defects from ion implantation, resulting in a reduction of the maximum yield pressure obtainable from this technique. The fraction of samples which exhibit yield correspond to inferred dislocation density from hardness measurements, while the use of a coefficient of variance appears to correspond more closely to the EBSD KAM measurement of local curvature. This suggests a coupled experimental approach can be used in selecting appropriate size tools for evaluating the mechanical behavior of materials that may, at intermediate defect densities and sizes, exhibit highly

stochastic properties. The KAM measurement coupled with Image Quality mapping in EBSD appears to be a viable non-destructive method for, to first order, identifying the spatial variations in dislocations that increase the variability in yield behavior under contact loading. As a final note, the KAM measurement, though powerful, should be cautiously applied as the technique assumes GND density is proportional to total dislocation density.

CHAPTER 4. DEFORMATION AND FRACTURE OF A MUDFLAT-CRACKED LASER-FABRICATED OXIDE ON TITANIUM

Previously published by The Journal of Materials Science*, Volume 48, pages 4050-4058, in June 2013.*

4.1 Introduction

Coloring the exposed surfaces of metallic materials by forming an oxide or nitride layer *via* laser irradiation is a well-established surface modification method.[68] Surface colorization of pure metals and alloys is typically a thermochemical growth process facilitated by the heat of absorbed laser light. Localized heating, provided by a focused laser beam, can lead to the growth of dielectric phases whose thickness is influenced by the laser process parameters. Most previous experimental and theoretical work on laser colorization involves continuous wave (CW) laser exposure. Studies have correlated optical properties (often determined by ellipsometry) with thickness and structure.[69,70] Recently, a few groups have pursued pulsed laser colorization,[71,72] because of its ability to promote surface oxidation with minimal impact to sub-surface volumes.[73] In general, this process involves sequential irradiation of a metal surface or evolving color layer with a train of light pulses. Models and experiments have focused on predicting the thickness of color layers by accounting for the repetitive rise in temperature, cooling rates after pulsing, and the gas diffusion coefficient into an irradiated target material.[74] Film color is intimately related to the layer thickness and the optical properties of a dielectric layer.

Oxide or nitride films formed on metallic substrates via pulsed laser irradiation are an example of a hard film-soft substrate system. Such systems are common as wear resistant coatings and as components in microelectromechanical systems (MEMS). However, due to the differences in thermal expansion coefficients between the substrate and film, the films are often susceptible to through thickness fracture from high residual stresses after formation. Films subjected to a tensile stress may fail due to delamination[75,76] or from crack propagation perpendicular to the surface. If there is some degree of uniaxiality in the film stress, or the fracture properties of the film are anisotropic, cracks may grow parallel to each other.[77,78] However, in general, cracks will propagate forming a two-dimensional array of islands; this failure mechanism is known as "mud flat" cracking, due to the similarity in appearance with the cracks found in drying mud.[79]

Nanoindentation is a powerful technique for investigating small material volumes.[63,80] Sudden excursions in depth (pop-ins) at low loads during load-controlled nanoindentation have been observed in substrate-film systems. Such load excursions in these systems have been ascribed to mechanisms such as oxide film fracture.[31,81–84] The technique is traditionally used to obtain mechanical properties of small volumes and can be applied in novel ways to evaluate film fracture behavior as well as residual film stresses *ex situ*.

For this study, the structure and properties of oxides fabricated on a titanium substrate with pulsed laser irradiation were characterized with a combination of microscopy, X-ray diffraction (XRD), and indentation techniques. Electron microscopy and diffraction probed phase, film thickness and microstructure. Atomic force

microscopy (AFM) was used to image surface topography. Mechanical properties were investigated with nanoindentation. High load nanoindentation with a large radius conical tip was utilized to study the fracture behavior of the oxide films. Finally, conducting indentation probed the correlation of mechanical and electrical properties.

4.2 Experimental Procedures

Four oxide coatings were fabricated on commercial purity Grade II titanium (henceforth Ti) substrates by rastering a 120 ns pulsed laser beam across polished surfaces in ambient atmospheric conditions. All oxides were created with an Er-doped, glass-fiber laser from SPI Lasers, Inc. operated at 5.6 W average power. A laser pulse frequency of 225 kHz was employed, and the focused laser beam was approximately Gaussian shaped with a $1/e^2$ width of 59 μm. Multiple overlapped laser scans created 4 x 4 mm areas for testing. Four laser scan rates, 130 mm/s 140 mm/s, 150 mm/s, and 160 mm/s, were chosen and hatch (centroid-to-centroid spacing) was 10 μm. Faster laser scan rates correspond with lower laser fluences. First order estimates of power dissipation suggest the near-surface sample temperature rises above the β-transus.

The resulting oxide phase was determined using grazing incidence X-ray diffraction (GIXRD) in a PanAnalytical Empyrean diffractometer with a Cu Kα source having a wavelength of 0.15418 nm. The microstructure and morphology of the laser oxides were then characterized using scanning electron microscopy (SEM), performed with a JEOL JSM-840A scanning electron microscope, transmission electron microscopy (TEM) using a FEI Titan G2 8200 aberration-corrected transmission electron microscope and AFM using a Bruker Multimode.

Nanoindentation measurements to determine mechanical properties were carried out with a Nanoindenter XP with a dynamic contact module (DCM) for low load testing, using both the quasistatic mode (QS) and the continuous stiffness module (CSM). A Berkovich probe with a radius of approximately 150 nm was used for mechanical property testing. Fracture behavior of the oxides was also examined with nanoindentation; a 90^{o} conical indenter tip with a nominal radius of 1μm was pressed in to the surface using the XP module with peak loads of 20 mN, 35 mN, 50 mN, and 80 mN. Indents were then imaged with a FEI Sirion FEG/SFEG scanning electron microscope and image-processing software was used to determine crack circumferences. Additionally, electrically conducting nanoindentation was employed to evaluate the electro-mechanical properties of the films, including the conductance and current-voltage (I-V) characteristics using a Hysitron Triboindenter 950 with electrical contact resistance (ECR) measurement capability and a boron-doped diamond Berkovich indenter. Electrical data was collected in voltage-source mode during the 10 mN hold segment of the loading cycle. Sweeps were 2 s long and were directed from -10 V to +10 V.

4.3 Results and Discussion

4.3.1 Phase, Microstructure, and Morphology

The oxides fabricated in this study were on the order of 200 nm thick. In comparison, the thickness of a typical native oxide film on Ti is generally on the order of 2-3 nanometers[85] while electrochemically grown oxides range from 10s to 100s of nanometers.[86] Though the oxides produced by laser irradiation are relatively thick, in comparison to the bulk substrate thickness they make up only a small fraction of the total

sample. Therefore, low-angle (5° incident angle) GIXRD was used for film analysis, revealing that the oxides are composed of TiO and Ti_6O (Figure 4.1a). GIXRD and TEM analysis identified the presence of a Ti_6O interfacial layer, which is essentially intercalated oxygen in the HCP α-Ti substrate. TiO comprises the majority of the film and has a face centered cubic structure and a lattice parameter of approximately 0.417 nm. Additionally, a thin overlayer of TiO_2 was detected; this layer is primarily responsible for determining film color.[87] Discontinuous Debye rings observed in an area detector image imply that the Ti substrate has a coarse grained microstructure. This structure was verified by TEM (Figure 4.1b). Conversely, the oxide film has a very fine grained structure; the oxide grain size, *D,* can be estimated using the Scherrer equation:[88,89]

$$D = \frac{0.9\lambda}{(\delta 2\theta)cos\theta}, \qquad \text{Equation 4.1}$$

where λ is the incident wavelength in nm, $\delta 2\theta$ is the full-width at half-maximum (FWHM) of the diffraction peak, and θ is the Bragg angle. The values are corrected for instrumental broadening by comparison with a standard cubic-TiO powder diffraction pattern. The true peak broadening is obtained from the following equation:

$$c = (b^2 - a^2)^{1/2}, \qquad \text{Equation 4.2}$$

where *c* is the true peak broadening, *b* is FWHM of experimental spectra, and *a* is the FWHM for a profile from the same reflection from a standard TiO powder sample.[90] Realizing that Equation 4.1 does not take in to account microstrain effects, and may thus underestimate the grain size, the grain size of the oxide is on the order of 5-11nm. The calculation supports the proposition that the fabricated oxides are nanocrystalline.

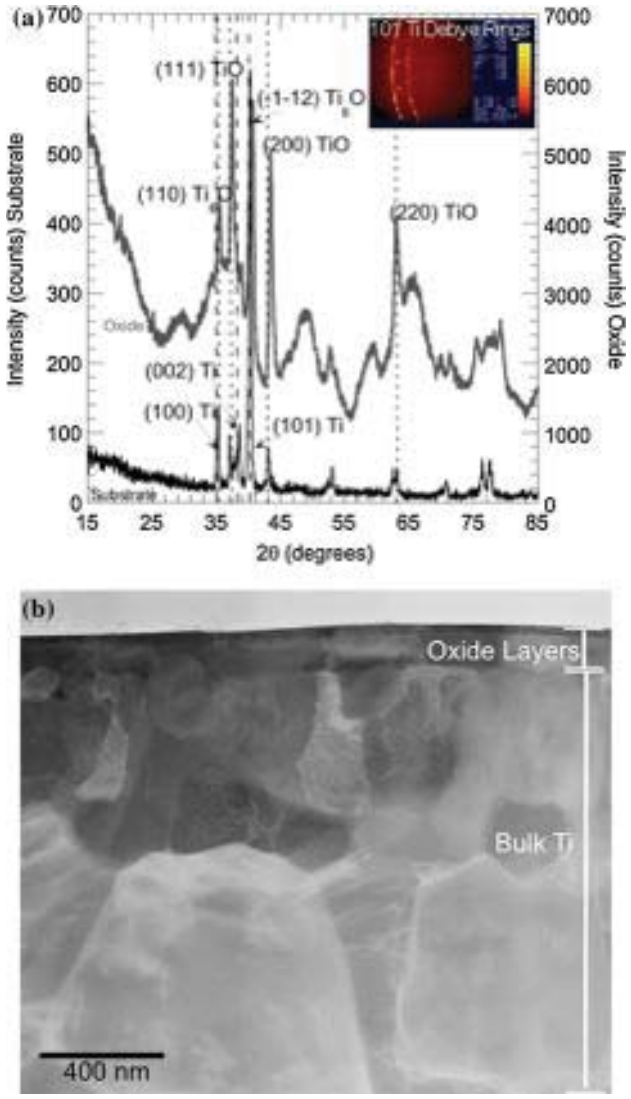

Figure 4.1 5° Grazing incidence XRD of a typical 225 kHz Ti oxide and a full $\theta/2\,\theta$ scan showing Ti substrate (a). Peak ID indicated predominant oxides consist of TiO and Ti_6O, which is essentially intercalated O on the Ti lattice. TEM image showing oxide layers (TiO over Ti_6O) atop bulk Ti (b).

The oxides have a topography consisting of a series of ridges and valleys. Figure 4.2 shows an AFM image and section analysis (4.2a) and an SEM micrograph (4.2b) of the surface of an oxide. A collection of interconnected cracks, resulting in the formation of islands of oxide, covers the surface. The pervasive mudflat cracking indicates the

oxides are stress-relieved; residual stresses that developed during fabrication, likely due to differences in thermal expansion coefficients between oxide and substrate, have been relieved through cracking. The average island diameter, or crack spacing, determined from line averages of SEM images similar to that shown in Fig. 2b, for all four oxides is 5.6±0.48μm.

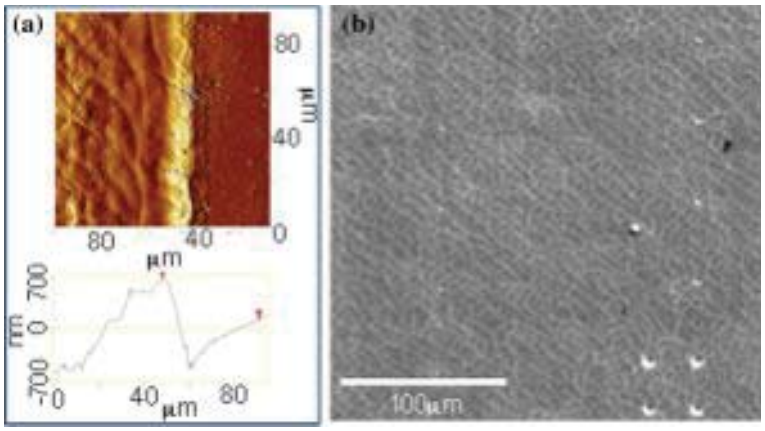

Figure 4.2 AFM image showing an oxide edge with respect to substrate as well as mud flat cracking and a corresponding section height analysis (a); SEM micrograph showing pervasive mudflat cracking across oxide surface, as well as a slight rippled appearance, evidence of ridge and valley topography (b).

4.3.2 Deformation and Fracture Behavior

Dynamic nanoindentation was performed using the CSM technique. For this experiment, the CSM tests were performed at a frequency target of 75 Hz and a depth target of 1 nm with a 350 nm limit, producing modulus, hardness, and stiffness values. Table 1 summarizes the average modulus and hardness values obtained in the range of $0.5 < a_c/h < 1.0$ where a_c is the contact radius and h is the film thickness. Contact radius is calculated using:

$$a_c = \sqrt{\frac{A}{\pi}}, \qquad \text{Equation 4.3}$$

where A is the contact area, determined via:

$$A = \frac{\pi}{4}\frac{S^2}{(\beta E_r)^2}. \quad \text{Equation 4.4}$$

In the prior equation, S, the harmonic contact stiffness is measured at each point during the indentation test and the reduced modulus, E_r, is computed with:

$$\frac{\mathbf{1}}{\boldsymbol{E_r}} = \frac{(\mathbf{1}-\boldsymbol{\nu^2})}{\boldsymbol{E}} + \frac{(\mathbf{1}-\boldsymbol{\nu_i^2})}{\boldsymbol{E_i}}, \quad \text{Equation 4.5}$$

where ν is Poisson's ratio of the sample (0.3), ν_i is Poisson's ratio of the indenter (0.07), E is the modulus of the sample, taken directly from continuous stiffness measurement, and E_i, is the modulus of the indenter (1141 GPa). In the chosen a_c/h range, the indentation depth is sufficient to overcome surface asperity effects, but shallow enough to avoid the influence of the more compliant substrate. The moduli reported in Table 4.1 are sample modulus values.

Table 4.1 Modulus and hardness of oxides tabulated as a function of scan rate.

Scan rate (mm/s)	*Modulus (GPa)*	*Hardness (GPa)*
130	217±12	16.4±0.5
140	215±25	15.4±0.95
150	214±10	15.1±2.2
160	213±9	19.0±1.9

Load-displacement data from quasi-static indentation are shown in Figure 4.3, performed in load control with a Berkovich indenter. Load excursion events, that is, a

sudden increase in depth with no increase in load, which are a result of oxide fracture, were evaluated to gain an understanding of the relative strengths of the oxides. The excursion load increases with increasing laser scan rate (Figure 4.4). The minimum critical load to initiate fracture is highly dependent on scan rate, while the maximum excursion load is less dependent on processing. The observation of excursion events at relatively low loads indicated that a fracture study could be successfully performed at higher loads with a tip of self-similar geometry.

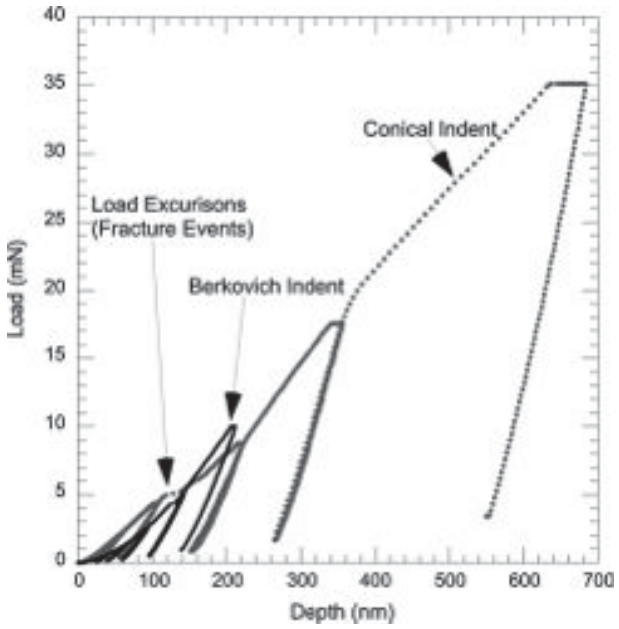

Figure 4.3 Example load-depth curves generated from Berkovich indentation (for mechanical property characterization) and conical indentation (for fracture study).

The presence of mudflat cracking and the observation of fracture-related excursion events indicate that direct calculation of film fracture toughness and residual stress, which caused the mudflat cracking, is viable. Pervasive mudflat cracking denotes that the oxide film was once under a significant stress, which has been dissipated via cracking, thus the film as-tested is assumed to be in a stress relieved state. Then, if it is

possible to calculate the fracture toughness from the stress-relieved film, that value can be combined with measured mechanical properties to calculate the stress required to initiate and propagate the observed fracture pattern, that is, the residual film stress that was present during growth and processing. This implicitly assumes that the fracture behavior measured at room temperature is similar to that when the films undergo mudflat cracking, which may be at an elevated temperature.

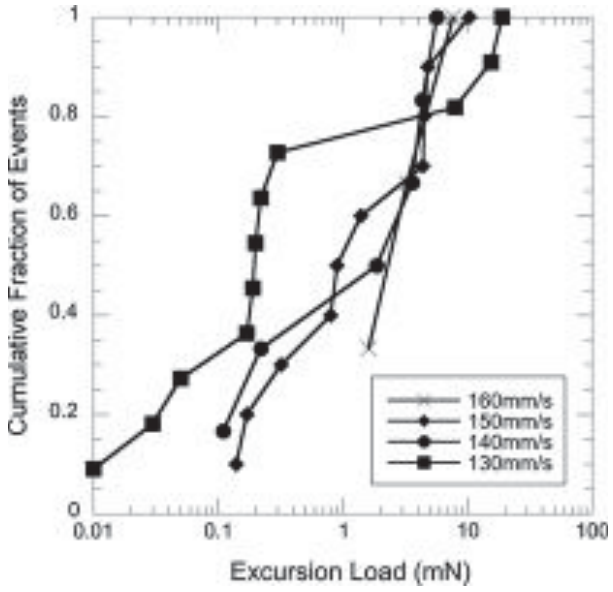

Figure 4.4 Cumulative distribution of load at discrete events, resulting from Berkovich indentation.

In order to investigate the fracture behavior of pulsed laser oxides, the films were indented with a conical tip of radius ~1 μm to maximum loads of 20 mN, 35 mN, 50 mN, and 80 mN. Load excursions in the load-displacement data indicated the initiation of an oxide fracture event (Figure 4.3). Cracked areas were measured using image analysis software and compared with contact areas calculated from load-displacement data. The

outermost circumferential cracks correspond with the circumference of the calculated plastic zone for indents at all four loads. The plastic zone is calculated as:[91]

$$c = \sqrt{\frac{3P_c}{2\pi\sigma_y}}, \quad \text{Equation 4.6}$$

where P_c is the critical fracture load, that is, the load at the initiation of an excursion event, and σ_y is the yield strength of the oxide, which is estimated from hardness, *H,* using Tabor's relation:[57]

$$\sigma_y = \frac{H}{3}. \quad \text{Equation 4.7}$$

Figure 4.5 shows a series of SEM micrographs of indents at various loads with obvious circumferential cracking. The contact areas at pop-in are typically much smaller than the outermost circumferential crack contact area. However, when inner circumferential cracks are observed, the contact areas measured for these cracks correlate well with pop-in contact areas.

The cumulative distribution of fracture loads resulting from conical indentation is shown in Figure 4.6. The critical load required to cause fracture is a function of processing parameters: faster laser scan rates require a higher applied load to cause through-thickness fracture. Similarly, faster laser scan rates have higher maximum fracture loads than their slower counterparts. A comparison of Figure 4.4 and Figure 4.6 gives insight into the mechanisms responsible for initiating fracture. If the observed indentation fracture initiated at the pre-existing mudflat cracks then low loads would be more similar for the conical indents, which have a larger sampled volume than Berkovich

indents. However, conical indentation produced pristine indents, regardless of proximity to a mudflat crack; indentation fracture is not determined by the existence of mudflat cracks. Variation in fracture load, then, is likely tied to existence of another kind of defect.

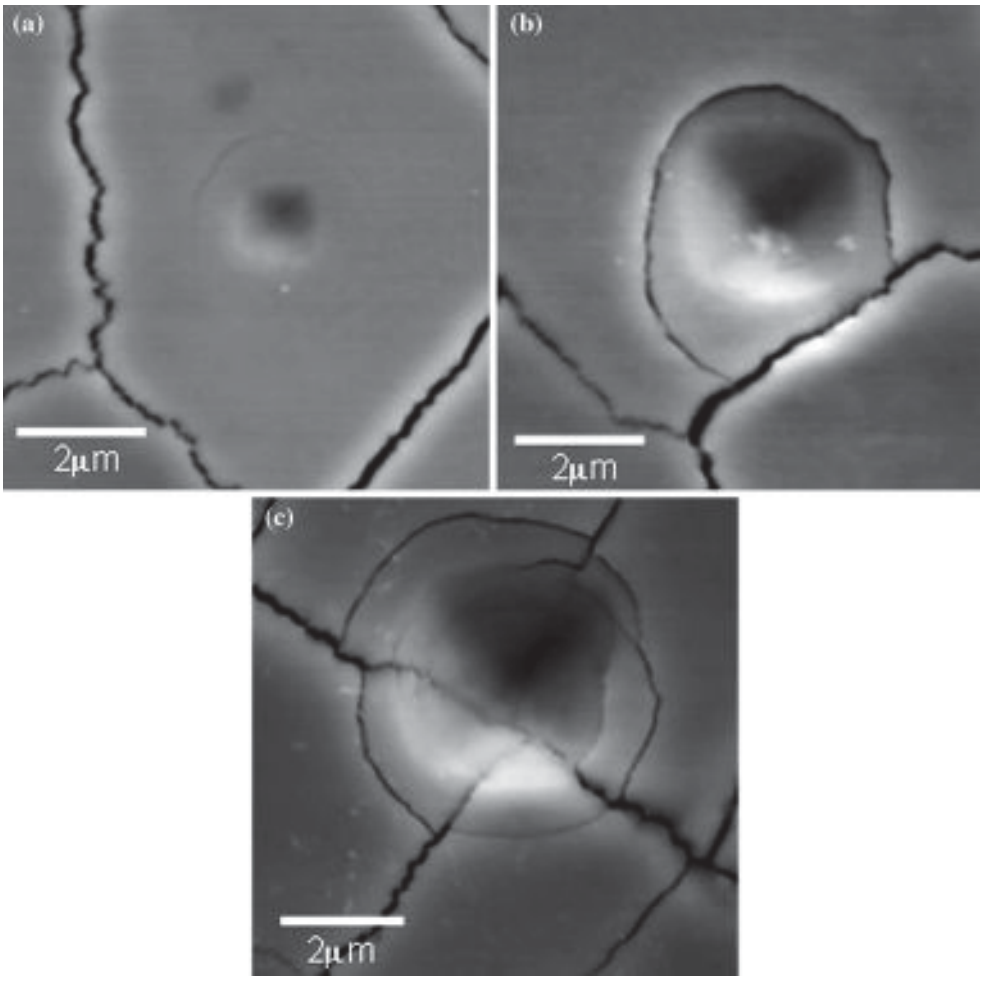

Figure 4.5 Micrographs showing typical oxide fracture morphology: circumferential cracking at the plastic zone radius of the indent, (all). Image (a) shows a complete circumferential crack surrounding a 20 mN indent in the middle of an oxide ‘‘island.’’ When indentation occurs on or near a pre-existing crack, the outermost circumferential crack may terminate as with the 50 mN indent in (b) or continue through that crack as with the 80 mN indent in (c). At higher indentation loads, nested cracks are visible (c), suggesting that through-thickness oxide fracture occurred at a load much less than the peak load, creating an ‘‘island’’ of oxide under the indenter, which continued to move with the indenter until peak load was reached.

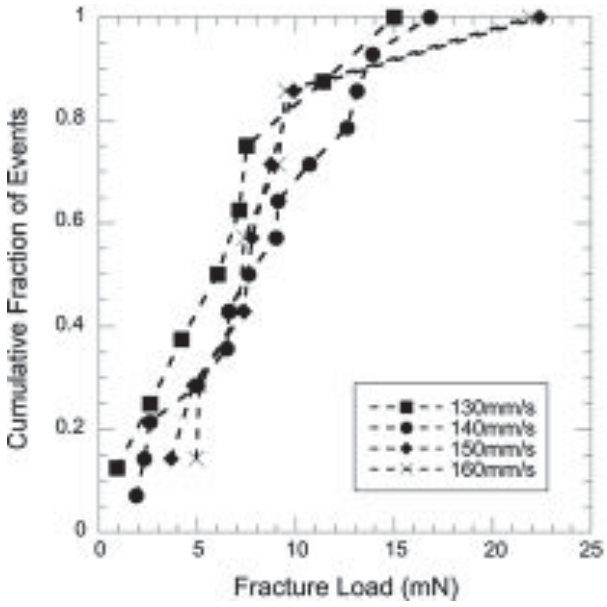

Figure 4.6 Cumulative distribution plot of fracture load, determined from excursions in conical tip load-depth data. Rates listed in the legend are the scan speeds used during laser-stimulated oxidation.

Since load at fracture can be used to calculate fracture toughness, Figure 4.6 indicates there should be a correlation between processing parameters and fracture toughness. An energy method[92] was employed to quantify the fracture toughness of the oxides. Through-thickness cracks likely occur at the elastic-plastic boundary of the substrate,[93] thus the film shrouding the plastic zone must deform to accommodate the indentation. Figure 4.7 is a schematic of the development of a through-thickness crack during indentation using a sphero-conical tip.

In addition to the size of the plastic zone, the energy required for deformation and film fracture is necessary to compute fracture toughness. Integration of the experimental load-displacement curves produced during indentation of the oxide film, until the onset of an excursion event, yield the total system energy, U_{system}:

$$U = \int_0^{\delta} P d\delta. \quad \text{Equation 4.8}$$

The total energy of the system is the superposition of the energy required to both fracture the film as well as plastically deform the substrate. Integrating the load-displacement curves produced during conical indentation of the substrate alone result in the energy required to deform the substrate, $U_{substrate}$. The integration is performed only up to the same depth as the critical fracture depth of the oxide to account for plasticity in the substrate during indentation of the oxide-substrate system, and is not the entire work of indentation for the entire load-depth curves shown in Figure 4.3 or the resulting indentation impressions in Figure 4.5. The amount of energy needed to fracture the film, U_{film}, can then be determined by subtracting the energy to plastically deform the substrate from the total system energy at the same depth:

$$U_{film} = U_{system} - U_{substrate}. \qquad \text{Equation 4.9}$$

The calculated film fracture energies are given in Table 4.2. The energy is dependent on the area produced from the initiation and propagation of a crack. It takes a critical amount of energy to produce the surface area of a new crack, which is the circumference of the crack multiplied by the film thickness. Assuming the majority of the energy goes into propagating the crack, and normalizing energy by the crack area results in the crack extension force, G:

$$G = \frac{U_{film}}{4\pi ch}, \quad \text{Equation 4.10}$$

where *c* is the plastic zone radius and *h* is the oxide film thickness. The crack extension force is modeled for a constant load fracture condition, assuming all strain energy is released during fracture. The denominator is doubled because two new surfaces are created during crack extension. Calculated crack extension forces are shown in Table 4.2.

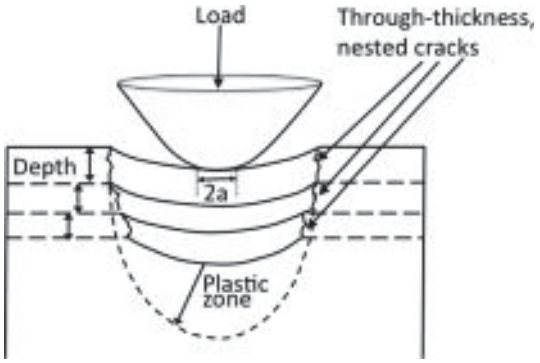

Figure 4.7 Schematic of through-thickness, nested cracked generated from high load nanoindentation.

Fracture criteria can be grouped in to two categories: energy methods and stress intensity methods. The two methods can be correlated by assuming the thin film is in a state of a plane strain; thus:

$$K = \sqrt{GE}, \qquad \text{Equation 4.11}$$

where *E* is the plane strain elastic modulus of the film and *K* is the stress intensity factor. Calculated values of *K* are collected in Table 4.2 as a function of scan rate. Contrary to the qualitative graphical analysis of fracture load, in general, the critical stress intensity decreases with increasing laser scan rate (decreasing laser fluence) and the calculated extension force and toughness values are similar to those calculated for titanium oxides in other studies.[92,94,95] This energy based fracture criterion analysis indicates that indentation

induced film fracture can be evaluated successfully for a system with an extensively pre-cracked film on a more compliant substrate. Additionally, while the statistics of load at fracture may be used to qualify the strength of a film, it may not be a good indication of the quantitative fracture toughness trend, thus a fracture mechanics calculation should be performed.

Table 4.2 Oxide thickness, h, fracture energy of the film U_{film}, crack extension force, G, stress intensity parameter, K, and residual stress, σ_0, of oxide films grown using different laser scan rates.

Scan Rate (mm/s)	*h (nm)*	*U_{film} (pJ)*	*G (J/m^2)*	*K (MPa√m)*	*σ_o (GPa)*
130	153	255	35.8	3.57	10.3±1.9
140	140	204	35.7	2.77	8.88±1.6
150	135	94	33.7	2.58	6.73±1.1
160	125	153	33.5	2.49	7.46±2.2

The energy-based analysis of thin film fracture is then used as an element in determining the residual stress of the oxide. Thouless[96] presented a comprehensive evaluation of the development and relaxation of stresses in thin films and through evaluating cracking as a method of stress relief developed a model relating film thickness, strain, and crack spacing. In the current study, the film thickness, h, and crack spacing, S, are measured, while the fracture toughness, K, is calculated. The strain in the film which results in mudflat or other regular cracking arrays, ε_o, is:

$$\boldsymbol{\varepsilon_0} = \sqrt{\frac{\boldsymbol{K_f(1-\nu_f)}}{\boldsymbol{(1+\nu_f)E_f h\left(\frac{S}{5.6h}\right)^2}}}, \qquad \text{Equation 4.12}$$

where E_f is the elastic modulus of the film and ν_f is Poisson's ratio of the film, in this case assumed to be 0.3. There are stress and strain discontinuities across the interface from the extrinsic film stress. We assume the coefficients of thermal expansion mismatch and modulus of the substrate and film are isotropic so that biaxial stress conditions apply. In this case, the residual stress, $\sigma_{o,}$ can be determined from:

$$\sigma_0 = \frac{E_f \varepsilon_0}{1-\nu_f}. \qquad \text{Equation 4.13}$$

Residual stresses formed during growth for each film are compiled in Table 4.2. In general, residual stress decreases with increasing laser scan rate (decreasing laser fluence). Oxides produced at faster laser scan rates likely have a higher concentration of point defects created from fast growth rates, which may decrease the residual stresses imparted during formation. The residual stresses are somewhat larger than values reported for thin films deposited with other techniques, many of which result in compressive stresses.[97,98] In this technique, tensile stresses were generated, which are relieved via mudflat cracking, suggesting this growth method differs from others reported, resulting in variations in residual stresses. However, oxide films can withstand very high residual stress and due to the film thickness, mismatch between thermal expansion coefficients and the speed of fabrication, the values are not unreasonable. Similarly high values have been observed with TiN films deposited via pulsed laser deposition.[99] It is important to note that this technique for calculating residual stress was chosen because of the unique processing conditions as well as the singular films that are produced. The harsh fabrication environment and thick substrate preclude the use of wafer curvature methods for determining residual stress. Another common procedure for ascertaining residual film

stress involves XRD; however this routine is not straightforward in this case because the films have a complex, non-stoichiometric phase. As residual stresses in other systems can impact film reliability,[100] a method that allows quantifying residual stress in these types of systems should be useful in future processing-structure-properties relationships for this class of materials.

4.3.3 Electrical Response During Contact Loading

Conducting nanoindentation involves pressing a conductive (boron-doped) diamond Berkovich indenter into a sample at a constant load/unload rate while applying a voltage and monitoring the resulting current flow through the sample/indenter to determine current-voltage characteristics.[101] Current-voltage measurements are obtained from the hold segment of a 10 mN indent. Figure 4.8 presents the I-V data normalized by oxide thickness As shown in Figure 4.8, faster laser scan rates create more conductive oxides. Conductance is not dependent on oxide thickness, therefore another aspect of oxide structure must control the observed electrical response. Furthermore, the asymmetry of the I-V sweeps about zero suggest the formation of Schottky barrier due to unequal amounts of holes and electrons (the charge carriers) in the oxide. This correlation may indicate that defects, such as vacancies, in the oxide are the source of the increased conductance. The pure FCC phase of TiO is metastable and non-stoichiometric with a distorted NaCl structure resulting in vacancies in both the cation and anion partial lattices. Up to 15% of both Ti and O sites are vacant.[102] Based on mechanical properties and fracture behavior, faster laser scan rates are predicted to contain a higher concentration of defects. Increased current flow may also result from a higher vacancy concentration,

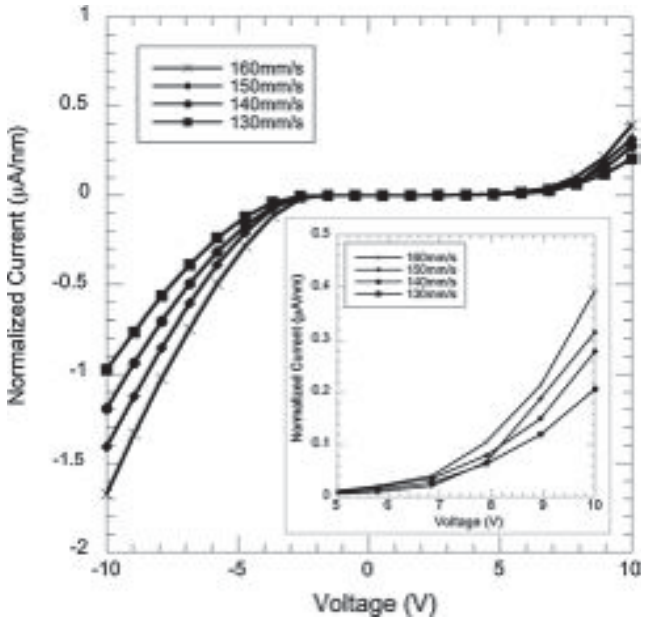

Figure 4.8 Current–voltage (I–V) sweeps normalized by oxide thickness (inset shows zoomed view of positive maximum) produced with conducting indentation, at constant load, demonstrate that faster laser scan rates correlate with higher conductance. Conductance is not dependent on thickness, which suggests it is dominated by defect concentration.

which increases with increasing O:Ti ratios, or other defects associated with fast deposition rates. Conductivity, σ_i, is related to concentration of carriers by:[103]

$$\sigma_i = \frac{c_i z_i^2 e^2}{kT} D_r, \qquad \text{Equation 4.14}$$

where c_i is the concentration of carriers, in this case vacancies, z_i is the valence, e is the charge on an electron, k is Boltzman's constant, T is the absolute temperature, and D_r is the random diffusion coefficient. By assuming z_i, e, k, T, and D_r remain constant for all four oxides, a qualitative comparison can be made between concentration and conductivity. Concentration is proportional to conductivity, thus, as conductivity, or in the case of this study, conductance, increases, the concentration of vacancies increases.

Unlike previous experiments with laser-fabricated oxides on stainless steel substrates,[104] there is no distinct correlation between oxide fracture load or stress intensity parameter and measured maximum current. Since conductance is related to carrier concentration, this analysis indicates that the defect structure of an oxide, in particular the vacancy concentration, which is dependent on laser processing parameters, may play an important role in the electromechanical properties of the film.[105,106]

4.4 Summary and Conclusions

Phase, microstructure, deformation, and fracture behavior of pulsed laser-grown metal oxide films on titanium were investigated using a combination of electron microscopy, X-ray diffraction, scanning probe microscopy, and nanoindentation. The key findings are as follows:

1. Oxides grown in this manner are nanocrystalline and composed of three phases: an interfacial layer of Ti_6O, a mid-layer of TiO, and a thin outer layer of TiO_2. The high residual tensile stress is relieved through cracking, producing a mudflat-cracked surface. The oxides are brittle, with a hardness on the order of 16GPa and a modulus of ~200GPa.
2. Statistical and numerical analysis of nanoindentation data demonstrates that faster laser scan rates (i.e., lower laser fluence) lead to oxides that fracture at higher loads for a given contact probe. However, the slower scan rates produce oxides with an overall higher fracture toughness.
3. The combination of oxide properties and surface crack spacing provides a method for determining residual stresses, which form during growth of these films. The

high residual stresses are tensile and generally decrease with increasing laser scan rate.

4. Conducting nanoindentation manifests a correlation between processing parameters and oxide conductance—faster laser scan rates (lower laser fluence) correspond with higher conductance, likely due to the presence of defects, particularly vacancies.

In summary, the hardness and elastic modulus of oxides grown in ambient atmosphere with the pulsed laser method are relatively insensitive to processing parameters within the range of this study. However, the electro-mechanical properties and fracture behavior of the oxides do appear to correlate with processing conditions, suggesting that overall reliability will be impacted by the complex structure of the oxide formed in this novel process.

CHAPTER 5. MECHANICAL AND ELECTROMECHANICAL BEHAVIOR OF OXIDE COATINGS GROWN ON STANLESS SLEEL 304L BY NANOSECOND PULSED LASER IRRADIATION

Previously published by Surface & Coatings Technology*, Volume 235, pages 860-866, in November 2013.*

5.1 Introduction

Laser exposure of oxidizing metals such as copper,[107] vanadium,[108] titanium,[70,73] and stainless steels[69,109,110] in air results in the growth of discernable, highly colored layers. Surface laser-irradiation induces a pyrolytic reaction whereby a metal substrate undergoes a high-temperature chemical reaction with the ambient atmosphere resulting in the growth of a film composed of elements from the substrate in combination with gasses from the environment.[68] Various process gasses have been used, including air and nitrogen, resulting in the growth of oxides or nitrides on metal substrates after gas-phase transport, chemisorption, diffusion, and surface chemical reactions.[68] Such highly colored, robust films may find use as unique authenticity markings in welded or sealed components.

Previous studies concerning laser marking of stainless steel indicate that a variety of colors can be achieved[69,111] and that a multi-phase structure may ensue from surface pyrolytic reactions.[111,112] The thickness, phase, and composition of oxide films grown on austenitic stainless steel 304L vary as a function of laser processing parameters. Thicker oxides result in a “duplex” phase structure with a Cr-rich interfacial layer and an Fe-rich

overlayer. Thin oxides consist of a single Cr-rich layer. Generally, laser-heating causes melting of the stainless steel 304L substrate and Cr diffuses from the substrate to the oxide leading to a Cr-denuded zone to depths slightly less than the melt-zone depth.[111]

Nanoindentation is a viable method for studying the mechanical behavior of films such as those grown in this work.[63,80] Nanoindentation is traditionally used to obtain mechanical properties of small volumes, but can be applied in innovative ways to evaluate film fracture behavior and residual film stresses *ex situ*[113] or electromechanical behavior *in situ*.[101] Sudden excursions in depth (pop-ins) at low loads during load-controlled nanoindentation in substrate-film systems are often ascribed to oxide film fracture.[31,81–84] Indentation experiments using a conductive stage/tip system allow for the investigation of the combined electrical and mechanical response of bulk and film/substrate materials systems.

Most thin film nanoindentation studies involve films grown by physical vapor deposition, chemical vapor deposition, or electroplating. The mechanical properties of oxides fabricated by pulsed laser irradiation have not been studied in detail. Our study investigates classical thin-film properties of coatings made using a different far-from-equilibrium growth technique as well as develops novel test techniques. This study focuses on linking the mechanical and electromechanical properties of oxides produced on SS 304L using pulsed laser irradiation.

5.2 Experimental Procedures

Fifteen oxide coatings were fabricated on polished austenitic stainless steel 304L substrates by rastering a 120 ns pulsed laser beam across surfaces in ambient atmospheric

conditions. All oxides were created with an Er-doped, glass-fiber laser from SPI Lasers, Inc. operated at 5.6 W average power and pulse frequency of 225 kHz with scan speeds ranging between 30-600 mm/s. The focused laser beam was approximately Gaussian with a $1/e^2$ width of 59 μm. Multiple overlapped laser scans with a centroid-to-centroid (hatch) spacing of 10 μm created 4 x 4 mm areas for testing. Faster laser scan rates correspond with lower laser fluence (energy density).

The resulting oxide thickness, microstructure, phase, and composition of these films, evaluated with extensive coupled scanning transmission electron microscopy (STEM) and energy dispersive spectroscopy (EDS), have been reported previously.[104,111] Nanoindentation measurements to determine mechanical properties were conducted with a Nanoindenter XP with a dynamic contact module (DCM) for low load testing, using both the quasistatic mode (QS) for load-controlled testing and the continuous stiffness module (CSM), with tests performed at a frequency target of 75 Hz and a depth target of 1 nm with a 350 nm depth limit, producing stiffness, modulus, and hardness values. A Berkovich probe with a radius of approximately 150 nm was used for mechanical property testing. Fracture behavior of the oxides was also examined with nanoindentation; a 90^o conical indenter tip with a nominal radius of 1 μm was pressed in to a surface using the XP module with peak loads of 20 mN, 35 mN, 50 mN, and 80 mN. Indents were then imaged with FEI Sirion and JEOL JSM7600F scanning electron microscopes (SEM), and image-processing software was used to determine crack circumferences. Finally, electrically-conducting nanoindentation was employed to evaluate the electromechanical properties of certain films, including the conductance and polarization (I-V) characteristics, using a Hysitron Triboindenter 950 with electrical

contact resistance (ECR) measurement capability and a boron-doped diamond Berkovich indenter. Electrical data was collected in voltage-source mode during the 10 mN hold segment of the loading cycle. Potential sweeps were 2 s long and were directed from -10 V to +10 V.

5.3 Results and Discussion

5.3.1 Oxide Film Morphology and Composition

The oxides grown in this study range in thickness between < 20 nm to 490 nm, as measured using cross-sectional scanning electron microscopy, and have a topography consisting of a series of ridges and valleys. Laser fluence dictates film thickness; oxides grown at faster scan rates (lower fluence) are thinner than those fabricated at slower scan rates. Figure 5.1a presents an SEM micrograph of an oxide fabricated at an average laser power of 5.6 W and a scan speed of 30 mm/s resulting in an average thickness of 489 nm, which is representative of the typical surface topography; the inset is an atomic force microscopy (AFM) reconstruction highlighting a single ridge and valley period. The rippled topography is a result of overlapping laser passes and is thus less obvious as oxide thickness decreases.

Surface channel cracking is observed on oxides with thicknesses greater than 100 nm. Figure 5.1b, which presents an oxide grown at 5.6 W average laser power and scan speed of 47 mm/s, resulting in an average thickness of 405 nm, highlights the typical crack morphology observed on thick oxides. Pervasive, interconnecting, through-thickness cracks typically develop in a strained film as a means to relieve residual film stresses resulting from differences in coefficients of thermal expansion between the

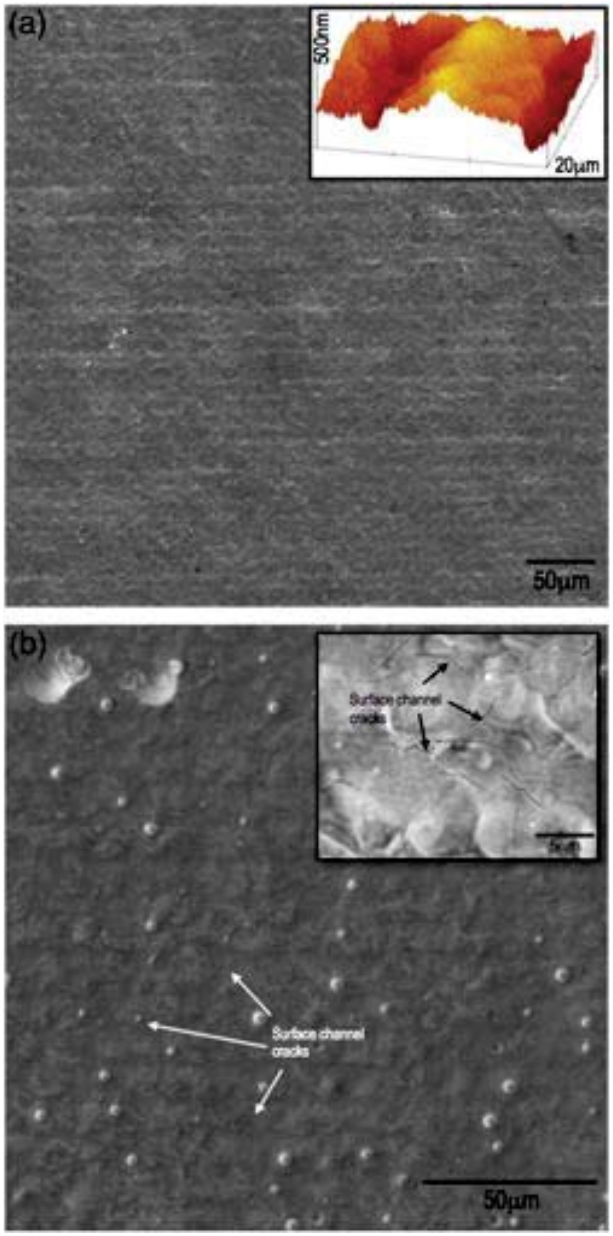

Figure 5.1 SEM image showing rippled surface topography. Right inset is an AFM reconstruction of a single ridge-valley period. This oxide layer was made using an average power of 5.6 W and a scan speed of 30 mm/s, yielding an average oxide thickness of 489 nm (a). SEM micrograph showing pervasive surface cracks formed post-processing to relieve residual film stress (b). This oxide layer was made using an average power of 5.6 W and a scan speed of 47 mm/s, resulting in an oxide 405 nm thick, on average.

substrate and the film.[113,114] It is likely that residual stress increases as oxide thickness increases, as has been observed in laser-fabricated films on Ti substrates;[113] however, it is also possible that stress is constant and strain energy increases with thickness, as fracture can be an energy driven process. Below an oxide thickness of ~100 nm (corresponding to a laser scan rate of ~400 mm/s) channel cracking is not observed. Away from indents, Figure 5.2(a)-(e) shows the reduction in the quantity of channel cracks with decreasing film thickness.

STEM and EDS analysis indicate that the oxide phase structure changes at thicknesses less than 200 nm (corresponding to a scan rate of >250 mm/s).[111] As shown in Figure 5.3a, oxides with thicknesses greater than ~200 nm develop a two-phase structure consisting of a Cr-rich interfacial layer containing Mn and an Fe-rich overlayer. This two-phase structure is identified only as a mixed oxide in the STEM image, but the compositional differences are clearly discernible in the inset EDS map in Figure 5.3a. Grazing incidence x-ray diffraction (Figure 5.3b) and micro-X-ray diffraction indicate the Cr-rich phase is likely $MnCr_2O_4$ and the Fe-rich oxide cap is likely magnetite, Fe_3O_4.[104] Conversely, at thicknesses less than ~200 nm, the films are a single Cr- rich oxide layer containing some Mn and Fe with no Fe-rich oxide cap.

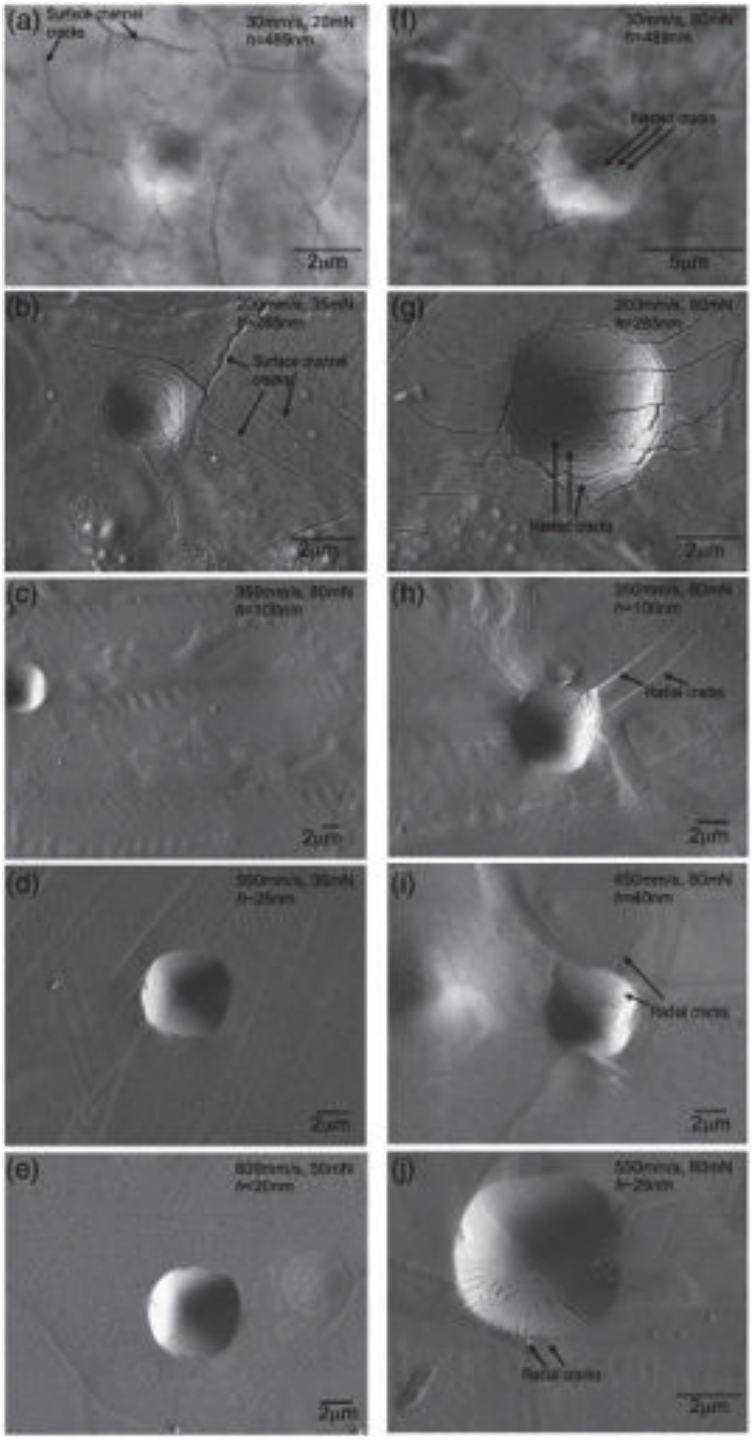

Figure 5.2 SEM micrographs of high load nanoindents and surrounding areas showing the reduction in surface channel cracking away from indents with decreasing film thickness, h, (a)–(e) as well as the shift from circumferential cracking to radial cracking as thickness decreases (f)–(j).

(a)

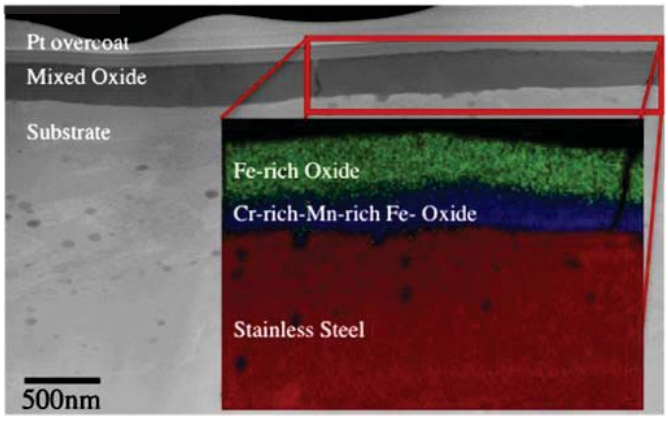

(b)

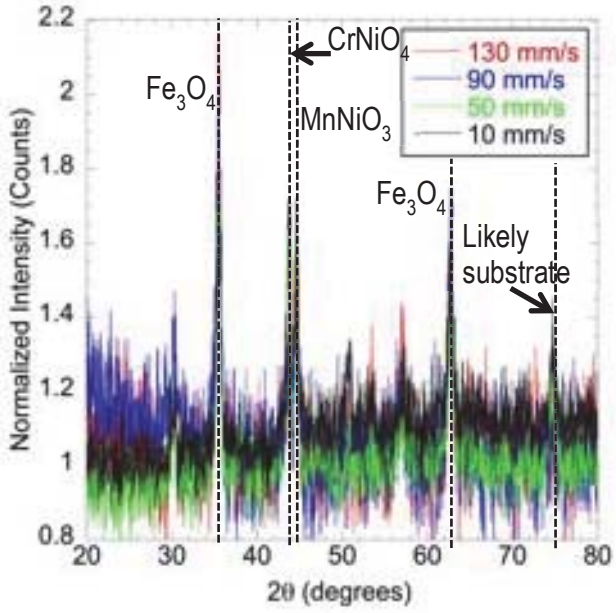

Figure 5.3 STEM imaging reveals a well-defined interface between substrate and oxide (identified as a mixed oxide in the micrograph), but corresponding EDS obviates two distinct layers within the 'mixed oxide' with a composition gradient between the Cr-rich interfacial layer and the Fe-rich overlayer of a thick oxide (a). This particular coating was made using an average power of 5.6 W and 47 mm/s, resulting in an average oxide thickness of 405 nm. Grazing incidence x-ray diffraction indicates the Cr-rich phase is likely $MnCr_2O_4$ and the Fe-rich oxide cap is likely magnetite, Fe_3O_4 (b).

5.3.2 Oxide Film Mechanical Properties and Fracture Behavior

Mechanical behavior of laser-fabricated oxides was probed using both dynamic and quasi-static nanoindentation methods. Dynamic nanoindentation was performed using the CSM technique, producing stiffness, modulus, and hardness values at every point throughout the test. Since these properties vary throughout the thickness, and can be influenced by surface asperities and roughness as well as the substrate, it is important to define a condition for comparing properties among samples. For this study, we have selected the comparative parameter to be the contact depth of the indentation for which the ratio between the contact radius, ac, and the film thickness, h, is in the range of 0.5-1.0. This selection of depth to extract properties for the variety of films was made to minimize the effects of surface asperities (deeper indentations reduced asperity effects) and substrate properties (deeper indentations are more influenced by the modulus and hardness of the substrate).[115,116] Table 5.1 summarizes the average hardness and modulus values obtained in the range of $0.5 < a_c/h < 1.0$. Contact radius is calculated using:

$$a_c = \sqrt{\frac{A}{\pi}}, \qquad \text{Equation 5.1}$$

where A is the projected area of the elastic contact, determined via:[63]

$$A = \frac{\pi}{4}\frac{S^2}{(\beta E_r)^2}. \quad \text{Equation 5.2}$$

The constant β has traditionally been used to account for stiffness deviations as a result of axial asymmetries of pyramidal indenters, and for Berkovich indenters is usually taken as

1.034. *S*, the harmonic contact stiffness is measured at each point during the indentation test and the reduced modulus, E_r, is computed with:

$$\frac{1}{E_r} = \frac{(1-\nu^2)}{E} + \frac{(1-\nu_i^2)}{E_i}, \quad \text{Equation 5.3}$$

where ν is Poisson's ratio of the sample (0.3), ν_i is Poisson's ratio of the indenter (0.07), E is the modulus of the sample, taken directly from continuous stiffness measurement, and E_i, is the modulus of the indenter (1141 GPa). Using this method to define a region for reporting properties (a_c/h) makes the critical assumption that modulus remains constant, which, of course, is not necessarily true for a film/substrate system. However, calculated film properties are relatively constant, and the film modulus is similar to (but lower than) the modulus of the underlying substrate, as reported in Table 5.1.

Table 5.1 Hardness, modulus, and H/E ratio of oxides tabulated as a function of laser scan rate and average oxide thickness. Values reported for contact radius to film thickness (a_c/h) ratios between 0.5 and 1.0.

Laser Scan Rate (mm/s)	*Thickness (nm)*	*Average Hardness (GPa)*	*Average Modulus (GPa)*	*H/E*
30	489	9.2±1.0	155±7	0.059
47	405	10.7±1.9	155±9	0.069
80	403	9.8±1.3	159±9	0.062
175	302	10.4±1.1	157±5	0.066
200	285	9.9±1.2	157±9	0.063
225	196	10.3±0.9	157±7	0.066
250	150	10.8±1.8	155±10	0.069
300	147	7.3±0.9	146±15	0.050
350	100	8.3±2.0	159±16	0.052
400	84	6.3±1.2	150±17	0.042
450	65	4.9±0.6	141±12	0.035
500	40	4.7±1.4	148±18	0.022
*550	~25	3.3±1.3	147±10	0.022
#600	<20	N/A	N/A	N/A

Therefore, to first order, the method appears to be reasonable in defining a consistent depth range for comparing properties among the various films. Interestingly, the hardness of the films begins to decrease as thickness drops below 150 nm, with the greatest decrease in hardness occurring as thickness decreases below 84 nm. This thickness range corresponds with the disappearance of oxide channel cracking, as noted in Figure 5.2. Oxide films that could be used as authenticity markers would need to be robust and resist wear and fracture. While high hardness is emphasized as a classical determinant of wear resistance,[117] researchers have shown that the ratio of hardness to elastic modulus (*H/E*) is often a better measure of wear resistance than hardness alone.[118–120] The calculated *H/E* ratios for the oxides in this study are included in Table 5.1. Again a sharp decrease in *H/E* occurs below thicknesses of 84 nm, as hardness drops. While high hardness is often desirable for wear resistance, superhard or ultrahard films are also often brittle; in many cases a protective coating which is both reasonably tough and wear resistant is required. A high *H/E* ratio is typically an indicator of high wear resistance; in this study thicker films are likely less susceptible to wear than thin oxides.

High-load, quasi-static indentation tests can be used to obtain a semi-quantitative understanding of both oxide fracture behavior and film toughness. A conospherical indenter tip with a radius of 90^{o} was chosen to apply the loading condition to the thick, hard oxide films on a more deformable stainless steel substrate, because this system is well-approximated by a model spherical loading of a hard elastic plate on a soft, yielding substrate,[93] represented schematically in Figure 5.4. When loaded, the plate (film) undergoes elastic deformation until brittle fracture, while the substrate is displaced plastically at relatively high loads.[93] Typically, large, circumferential cracks will occur at

the plastic zone radius.[113] This is indeed observed for oxides in this study with thicknesses greater than 100 nm. In contrast, spherical loading of a thin hard film on a compliant substrate results in plastic deformation of the film-substrate system; the majority of the energy is dissipated by the substrate and the film conforms to the plastic deformation of the substrate. The film may undergo radial cracking, as observed in this study for films less than 100 nm thick. The stress tensor beneath the indent dictates the type of cracking initiated; radial tensile stresses are responsible for initiating circumferential cracks, while circumferential tensile stresses are responsible for radial cracks.[121]

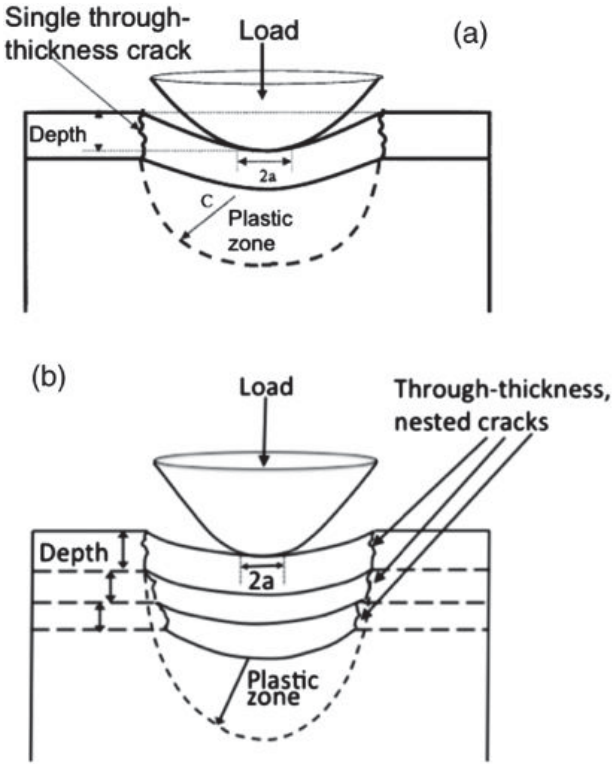

Figure 5.4 Schematic showing fracture of a hard film on a soft substrate at low maximum loads (a) where a single through-thickness fracture event occurs, and at high maximum loads (b) where nested cracking can occur.

As evident in Figure 5.2(f)-(j), thicker oxides display circumferential cracking. The corresponding load depth curves for these indents exhibit pop-ins, or a sudden increase in depth with no corresponding increase in load. These discrete events have been linked to oxide fracture.[81,83,84,113] The schematic in Figure 5.4a shows a single circumferential crack occurring at the indent contact radius, representative of the cracking observed on indents with lower peak loads (20 mN-35 mN), while Figure 5.4b is a schematic of the nested cracking often observed for indents with higher peak loads (50 mN-80 mN). Nested cracking develops when through thickness fracture occurs at a load less than the peak load; the indenter continues to press into the sample but the effective indenter radius is now the radius of the fractured oxide "island" beneath the tip. Additional through-thickness fracture events may occur before the peak load is reached, resulting in multiple concentric circumferential cracks, which are visible throughout the indent. Image processing software was used to measure the fracture area observed with SEM. In general, the outermost circumferential cracks correspond with the calculated contact area; for inner circumferential cracks, fracture contact areas correlate with the contact area at the initiation of the pop-in, calculated via Equation 2. Figure 5.5 exemplifies the correlation between pop-ins and observed fracture for indents in a 403 nm (80 mm/s scan rate) and a 405 nm (47 mm/s scan rate) oxide. This analysis suggests load excursions recorded beyond the elastic zone are most likely film fracture events.[83] Furthermore, no spallation of the oxide is observed even when nested, concentric cracking occurs at the highest indentation loads, indicating that the film is well adhered to the steel substrate and interfacial fracture does not occur. This is substantiated by the limited delaminations observed by FIB sectioning and SEM imaging.

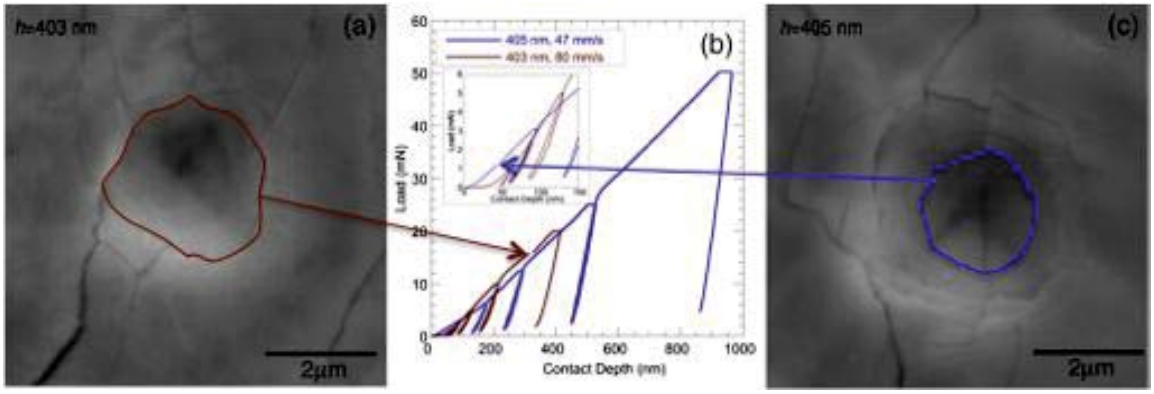

Figure 5.5 Circumferential cracks at the indent contact radius correspond to load-depth excursion at higher loads (a), while inner, nested cracks in high-load indents correlated with excursions at low loads (c).

A clear shift in fracture mechanisms occurs at a thickness of ~100 nm, below which circumferential cracking is eliminated. It is likely that the controlling stress for initiation of fracture shifts from radial tensile to circumferential tensile as the oxide thickness decreases, resulting in the preferential development of radial, as opposed to circumferential cracks. Michler and Blank[121] investigated the stress fields required to proceed from initiation of circumferential cracks to initiation of solely radial cracks as the film thickness, *h*, to indenter radius, *R*, ratio decreased for thin hard films on compliant substrates, finding small *h/R* ratios led to a network of radial and circumferential cracks. In the current study, the continual decrease of thickness leads to (1) the total disappearance of circumferential cracks and formation of radial cracks followed by (2), a sharp decrease in radial crack length until no cracking is observed for the thinnest oxides (fabricated at scan rates > 550 mm/s). The critical thickness for changing fracture mechanism is the same as that at which surface channel cracking ceases to develop, suggesting that the lower residual stress experienced by well-adhered thinner oxides may impact their toughness.

Additionally, X-ray micro-diffraction[111] indicates that within the identified critical thickness range the oxide phase may cease to be a duplex $MnCr_2O_4$ / Fe_3O_4 layered structure as observed for thick oxides, and instead consist of a single Mn-rich layer (possibly $MnCr_2O_4$). Magnetite and chromite phases are predicted to have slightly different fracture toughness values,[122] which may further impact the observed increase in plastic deformation without fracture of thin oxides.

5.3.3 Electrical Performance of Oxides During Contact Loading

Conducting nanoindentation involves pressing a conductive (boron-doped) diamond Berkovich indenter into a sample at a constant load/unload rate and monitoring the resulting current flow through the sample/indenter to determine current-voltage (I-V) characteristics.[101] Figure 5.6a shows the loading regime and resulting load-depth curve for a typical conducting indentation test, while Figure 5.6b presents the I-V data normalized by oxide thickness. The inset of Figure 5.6b is a log plot of the positive maximum of the polarization curves, clearly indicating faster laser scan rates (reduced laser fluence) result in more conductive oxide films. Since polarization data have been normalized by oxide thickness, but conductance still varies as a function of laser fluence, another aspect of oxide structure, aside from thickness, must control the observed electrical response. Furthermore, the asymmetry of the I-V sweeps about zero suggest the formation of a Schottky barrier due to unequal concentrations of holes and electrons (charge carriers) in the oxide. Based on mechanical properties and fracture behavior, faster laser scan rate oxides are predicted to contain a higher concentration of point defects, such as vacancies.

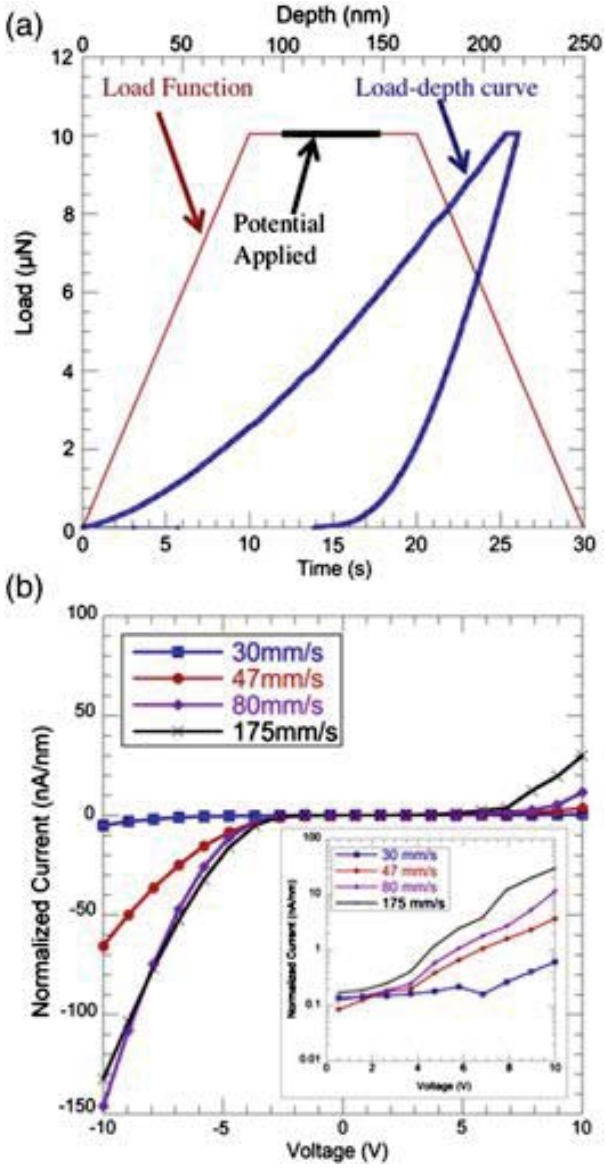

Figure 5.6 Loading regime used for conducting indentation, showing applied potential and resulting load–depth record (a). Polarization curves for 225 kHz oxides, normalized by thickness are presented in (b); the inset shows a log plot of positive maxima. Conductance is not a function of thickness, thus the dependence on scan rate must be linked to defect density.

Conductivity, σ_i, is related to carrier concentration by:[103]

$$\sigma_i = \frac{c_i z_i^2 e^2}{kT} D_r, \qquad \text{Equation 5.4}$$

where c_i is the concentration of carriers, in this case vacancies, z_i is the valence, e is the charge on an electron, k is Boltzmann's constant, T is the absolute temperature, and D_r is the random diffusion coefficient. By assuming z_i, e, k, T, and D_r remain constant for all oxides, a qualitative comparison can be made between concentration and conductivity. Finally, resistance spreading is unlikely to affect results as the contact area and total sampled volume are small and the volume of conductive substrate is constant for every test. Concentration is proportional to conductivity, thus, as conductivity, or in the case of this study, conductance, increases, the concentration of vacancies is predicted to increase.

5.4 Conclusions

Mechanical properties, fracture behavior, and electromechanical response of oxides fabricated on stainless steel 304L using a 120 ns-pulsed infrared fiber laser at an average power of 5.6 W, a pulse frequency of 225 kHz, and scan rates between 30-600 mm/s were investigated by coupling local deformation methods with high resolution microscopy. Thick films (h > 200 nm) exhibit pervasive channel cracking, which develop as a mechanism for relieving residual film stress due to laser processing. Channel cracking is gradually reduced as thickness decreases until it is no longer apparent on films with h < 100 nm. This critical thickness range also corresponds to a shift in fracture mechanism from radial tensile stress controlled (circumferential cracks) to circumferential tensile stress controlled (radial cracks). Because indenter radius is nominally constant, the shift in mechanism is likely controlled by oxide thickness. Additionally, within this critical thickness range the overall oxide composition changes; thick oxides have a duplex structure consisting of $MnCr_2O_4$ and Fe_3O_4, however, thin

oxides lack the Fe_3O_4 overlayer. Differences in film phase may also impact the shift in fracture mechanism, which is an indication of the toughness of the oxide. Fabricating robust, crack-free films to be employed as passive authenticity identifiers using nanosecond-pulsed laser irradiation requires tailoring of laser processing parameters to achieve specific toughness and residual film stress conditions. Pulsed laser irradiation is suitable for creating passive identification structures on stainless steel, however the thinner films, which are likely more resistant to film failure during contact loading may exhibit lower *H/E* ratio which means they are more susceptible to wear. Therefore, choosing the appropriate processing conditions for creating tamper-proof seals will require considering whether the primary failure mechanism is wear or environmental degradation.

CHAPTER 6. ENVIRONMENTAL RESISTANCE OF OXIDE COATINGS GROWN ON STAINLESS STEEL 304L AND CPII TITANIUM BY NANOSECOND PULSED LASER IRRADIATION

6.1 Introduction

Oxide films that could be used as authenticity markers must be mechanically robust, well-adhered to the substrate, and must develop an oxide-substrate system that is resistant to degradation in the projected exposure conditions. The most aggressive anticipated service condition is the marine environment, thus immersion testing in a simulated seawater solution and salt spray testing were selected to qualitatively capture the performance of the oxide-tagged stainless steel 304L and CP grade II Ti under such conditions. Anodic polarization was employed to gain quantitative insight into the localized corrosion behavior of the oxide-substrate systems. It is well known that grade II Ti is resistant to corrosion in NaCl solutions; conversely austenitic stainless steels are susceptible to pitting in chloride containing environments.[123] Recent investigations of the corrosion behavior of laser-treated stainless steels suggest that corrosion resistance depends on structure, morphology, and Cr concentration of the laser-treated area.[124–126] However, the environmental resistance of colored laser-fabricated oxide tags has not been well-studied, therefore, the results of the current investigation will be interpreted in terms of previous studies of the phase, structure, deformation, and fracture of these film systems.

6.2 Experimental Procedures

6.2.1 Stainless Steel

Austenitic stainless steel 304L substrates, with a composition in wt.% of 18.11% Cr, 8.00% Ni, 1.63% Mn, 0.42% Si, 0.14% Mo, 0.083%N, 0.025% S and P, 0.023% C, with the balance as Fe, were prepared for laser processing by metallographic grinding with 180 grit SiC paper and polishing with 9, 6, and 3 μm diamond suspension. Final cleaning involved rinsing in Lenium^{TM} degreasing solvent, followed by acetone, and then alcohol. Final sample dimensions were 12.5 × 12.5 × 3.4 mm. An Er-doped, pulsed fiber laser from SPI Lasers was used to irradiate the polished substrates in ambient atmospheric conditions, stimulating oxide growth. Laser marking involved irradiation at focus using a pulse frequency of 225 kHz and a pulse duration measured to be 119 ns. The beam exiting the fiber was collimated and directed through a variable beam expander onto two Nutfield steering mirrors and then focused onto the metal surface using a Linos f163 f-theta lens. The beam was approximately Gaussian with a $1/e^2$ beam width equal to 59 μm at focus. A Dataray WinCamD camera and z-stage confirmed that the Rayleigh length was N1 mm, which is larger than the variation in working distance for leveled metal samples. The relative humidity in the laboratory was ~30% during laser marking. Scanning the focused laser beam over a specimen at constant speed created each oxide tag. Upon the completion of a given line, the beam was blanked and then returned to the beginning of a neighboring, adjacent line offset by 10 μm. This offset, referred to as hatch spacing, provides a substantial beam overlap of adjacent lines and a uniform fluence within a given feature. Three sets of samples for environmental resistance evaluation were fabricated following an identical laser process.

The first set of samples, used for immersion testing, consisted of four SS 304L substrates with four oxide patterns fabricated on the surfaces (henceforth quad-oxide samples); a schematic of this sample configuration is shown in Figure 6.1a. Average laser power and pulse frequency remained constant on each stainless steel substrate, while laser scan speed varied for each oxide square within a substrate sample. Each oxide square had an area 4 mm x 4 mm. The second and third sample sets, designed for salt spray testing and anodic polarization, consisted of 12 individual oxide patterns fabricated on each SS 304L substrate. All oxides were fabricated at an average power of 5.6 W and a pulse frequency of 225 kHz resulting in areas of 6 mm x 6 mm. Scan rates varied from 30-600 mm/s. This configuration is illustrated schematically in Figure 6.1b. Table 6.1 summarizes the oxide processing conditions.

Immersion testing was conducted by submerging the four quad-oxide samples in a simulated seawater solution (pH 6) per the ASTM G31 standard[127] for 25 days. The solution was not de-aerated. SS 304L substrates were enameled to ensure that only the laser modified oxide surfaces were exposed to the environment. At the conclusion of the exposure period, samples were removed, rinsed with deionized water, and dried for 24 hours prior to microscopy.

Salt spray testing was then conducted on the 12 individual oxide samples. A polished blank SS 304L specimen was included in the test matrix as a control sample. All stainless steel substrates were enameled to ensure that only oxide areas were exposed to the salt air environment. Salt spray exposure was performed in accordance with the ASTM B117 standard[128] for 168 hours. Samples were rinsed and dried for at least 24 hours prior to microscopy.

Finally, anodic polarization tests were conducted on an untreated stainless steel blank and on oxides fabricated at 30 mm/s, 300 mm/s, 350 mm/s, and 500 mm/s to evaluate the localized corrosion behavior of the oxide-substrate system. These oxides were selected as a representative subset of the oxides exposed to salt spray testing. Anodic polarization tests were performed with a conventional three-electrode cell, with a Pt counter electrode and a Ag/AgCl reference electrode, using a Gamry DC105 corrosion test system. Polarization curves were produced in a 3.5% NaCl solution, which was not de-aerated, at a sweep rate of 0.5 mV/s after stabilization of the open circuit potential.

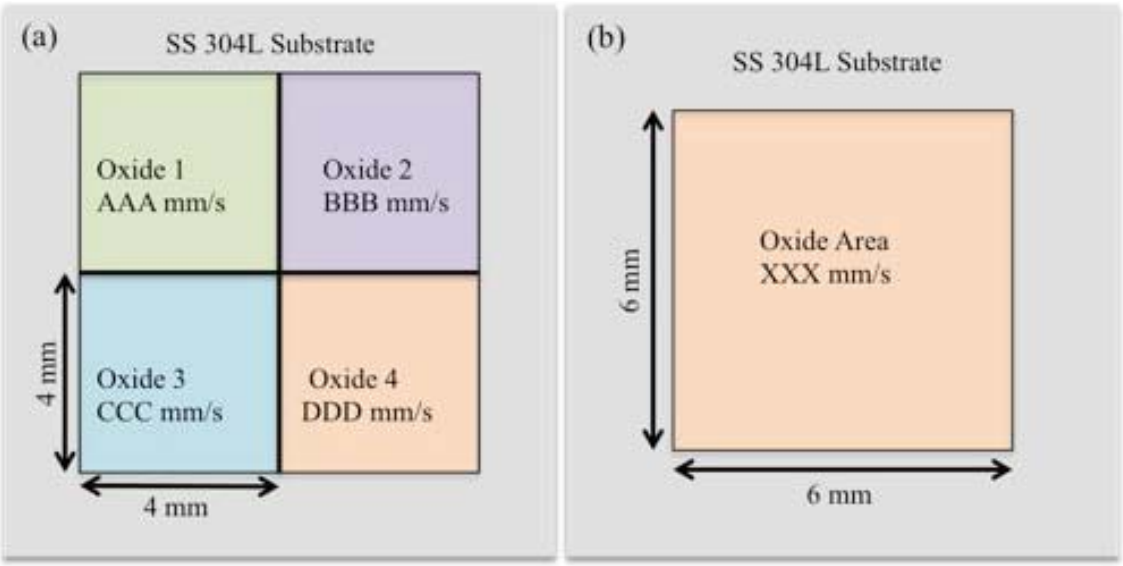

Figure 6.1 Schematic illustration of laser-fabricated oxide samples showing quad-oxide configuration for immersion testing (a) and single oxide configuration for salt spray exposure and anodic polarization (b).

Laser-fabricated oxides were imaged optically before and after environmental exposure. After exposure, the corrosion product and visible laser-fabricated oxides were imaged with electron microscopy using a Philips XL-40 FESEM; samples were then cleaned with oxalic acid to remove any corrosion product and imaged again. Certain

oxides were selected for post-mortem cross-sectional energy dispersive spectroscopy (EDS) to evaluate composition gradients, prior to oxalic acid cleaning. Using an FEI Quanta 3D Field Emission Gun Dual Beam SEM, trenches were milled in the samples with the focused ion beam (FIB). Cross-sectional EDS mapping was then conducted with Oxford Instruments data collection software.

Table 6.1 Processing conditions and resulting film thicknesses for two sets of oxide samples. All oxides fabricated at an average laser power of 5.6 W. All salt spray samples manufactured at a laser pulse frequency of 225 kHz.

Immersion Test Samples			Salt Spray Test Samples	
Laser Pulse Frequency (kHz)	*Laser Scan Rate (mm/s)*	*Thickness (nm)*	*Laser Scan Rate (mm/s)*	*Thickness (nm)*
225	30	489	30	489
225	47	405	47	405
225	80	403	80	403
225	175	302	175	302
250	10	#	200	285
250	50	#	225	196
250	90	#	250	150
250	130	#	300	147
275	10	#	350	100
275	50	#	400	84
275	90	#	450	65
275	130	#	500	40
350	40	#		
350	50	#		
350	60	#		
350	70	#		

6.2.2 Titanium

Commercially pure, grade 2 (ASTM B265) titanium substrates were prepared for laser color marking with conventional metallography to obtain a surface roughness (Sa) of 2-10 nm. Sample dimensions were 12.5 × 12.5 × 3.4 mm. Prior to laser processing,

each specimen was cleaned by rinsing in Lenium™ degreasing solvent, followed by acetone and alcohol. Ti samples were then irradiated in air using an SPI Lasers Er-doped pulsed fiber laser having a fundamental wavelength, $\lambda = 1064$ nm, following the same procedure enumerated in the previous section.

Six laser scan speeds—90 mm/s, 110 mm/s, 140 mm/s, 170 mm/s, 200 mm/s, 300 mm/s— were used to fabricate three identical sets of samples for salt spray exposure and anodic polarization testing. Average laser power and pulse frequency were kept constant at 7.6 W and 225 kHz, respectively. The approximate thickness of each coating has been previously investigated by Adams et al.;[87] Figure 6.2 is a replication of their findings.

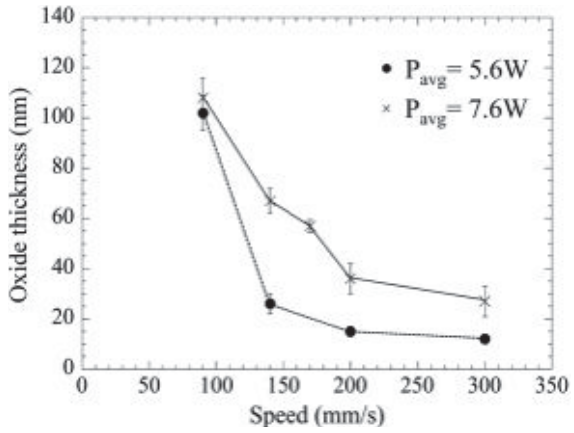

Figure 6.2 Plot of average oxide layer thickness measured by TEM. Reported values are the combined thickness of TiO_2 capping layers and underlying TiO. Results are plotted versus laser scan speed for different average powers; oxides used in the current study were grown at 7.6 W. Used with permission from: Adams, D. P. *et al.* Nanosecond pulsed laser irradiation of titanium: Oxide growth and effects on underlying metal. *Surf. Coatings Technol.* **248,** 38–45 (2014).

Two sets of identical samples were prepared for salt spray testing; in one case, the visible Ti substrate metal was coated with enamel to prevent interaction of the substrate with the environment during exposure, the second set of samples were exposed in the as-

fabricated condition. An untreated Ti sample was included as a control. Salt spray exposure was performed in accordance with the ASTM B117 standard[128] for 168 hours. Samples were rinsed and dried for at least 24 hours prior to microscopy.

The final six specimens, along with a blank Ti sample, were reserved for anodic polarization to evaluate the pitting corrosion resistance and general localized corrosion behavior of the oxide-substrate system. Anodic polarization tests were performed with a conventional three-electrode cell, with a Pt counter electrode and a Ag/AgCl reference electrode, using a Gamry DC105 corrosion test system. Polarization curves were produced in a 3.5% NaCl solution, which was not de-aerated, at a sweep rate of 0.5 mV/s after stabilization of the open circuit potential.

6.3 Results and Discussion

6.3.1 Stainless Steel Immersion Testing

A total of 16 oxides fabricated at four laser pulse frequencies and a range of scan rates were exposed to an aggressive simulated seawater environment. After 48 hours exposure a corrosion product had begun to deposit on the majority of the oxide areas; only the 225 kHz/175 mm/s, the 350 kHz/60 mm/s, and the 350 kHz/70 mm/s oxides were free of any visible corrosion product. After 25 days exposure, a thick corrosion product covered all oxide areas. Table 6.2 summarizes the development of corrosion products during immersion testing. Optical micrographs obtained before and after exposure are presented in Figure 6.3. The corrosion product visible in Figure 6.3e-h was identified by low angle X-ray diffraction (Bruker GADDS) as an iron chloride hydrate. . The corrosion product deposited on top of the laser-oxide areas; the laser-fabricated oxide

is clearly visible in the SEM image of a post-exposure FIB cross-section (Figure 6.4a). The corrosion product was not well-adhered to the oxide, flaking off easily when imaged with a high energy electron beam or after oxalic acid cleaning, revealing the laser-fabricated oxide still present on the metal surface. These results suggest that the corrosion product results primarily from corrosion of the underlying steel substrate, rather than severe dissolution of the laser-oxide coating.

Table 6.2 Development of corrosion product during immersion testing is tabulated by processing conditions.

Laser Pulse Frequency (kHz)	*Laser Scan Rate (mm/s)*	*Corrosion Product—48 hrs*	*Corrosion Product—25 days*
225	30	Yes	Yes
225	47	Yes	Yes
225	80	Yes	Yes
225	175	No	Yes
250	10	Yes	Yes
250	50	Yes	Yes
250	90	Yes	Yes
250	130	Yes	Yes
275	10	Yes	Yes
275	50	Yes	Yes
275	90	Yes	Yes
275	130	Yes	Yes
350	40	Yes	Yes
350	50	Yes	Yes
350	60	No	Yes
350	70	No	Yes

Subsequent post-mortem cross-sectional EDS provides a qualitative description of composition as a function of depth. EDS mapping (Figure 6.4a) detects a discernible difference in Cr, Fe, and O content throughout the substrate and into the laser-oxide and corrosion product; linear point profiling (Figure 6.4b) of an as-received oxide mounted in cross-section confirms EDS mapping and shows a decreasing Cr concentration moving

from the bulk substrate towards the oxide interface. Cr is depleted from the substrate to a maximum depth of ~2 μm (depletion depth varies with oxide thickness), confirming previous STEM EDS results.[111] Because stainless steel derives its corrosion resistance from the formation of a continuous Cr_2O_3 layer when Cr is dispersed throughout the matrix at a concentration of greater than approximately 12%, depletion of solute Cr below this critical concentration leads to decreased corrosion resistance.[129,130] Thus, the deposition of a corrosion product on top of the laser-oxides indicates that enough Cr is depleted from the substrate melt-zone during laser processing to reduce the Cr concentration below ~12 wt. % making the SS 304L susceptible to chloride attack.[131]

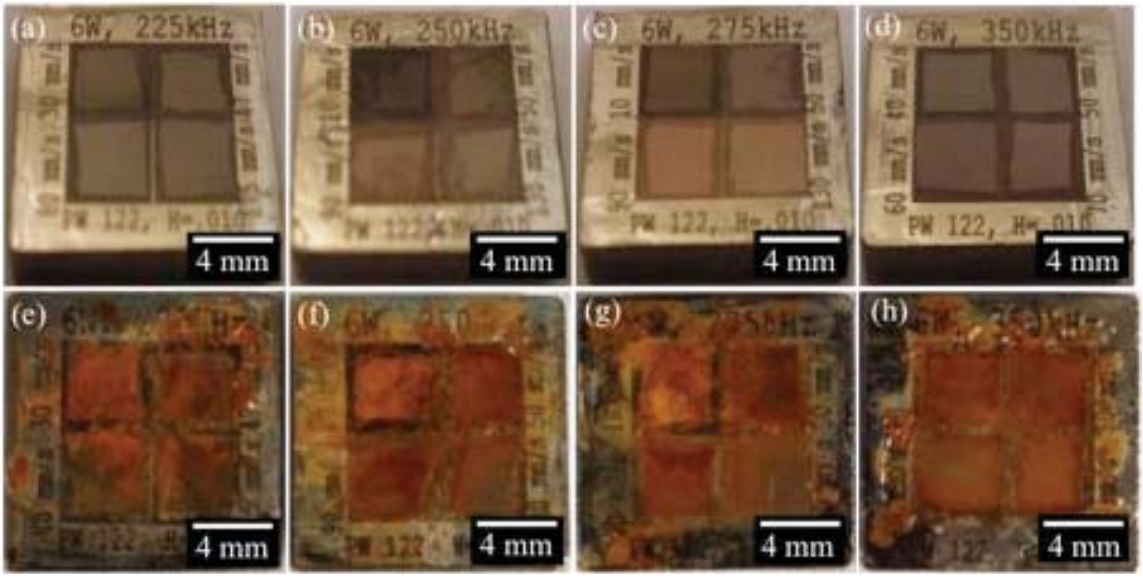

Figure 6.3 Quad-oxide samples before (a-d) and after (e-h) immersion in simulated seawater solution for 25 days. Uniform corrosion product suggests oxides are non-protective, likely due to the presence of through-thickness cracks, allowing exposure of Cr-depleted substrate to chloride containing environment.

The observed extensive corrosion of the laser-modified stainless steel substrate supports previous assertions that oxides fabricated on SS 304L via certain laser irradiation parameters are non-protective. Heterogeneities, such as cracks formed as a means to

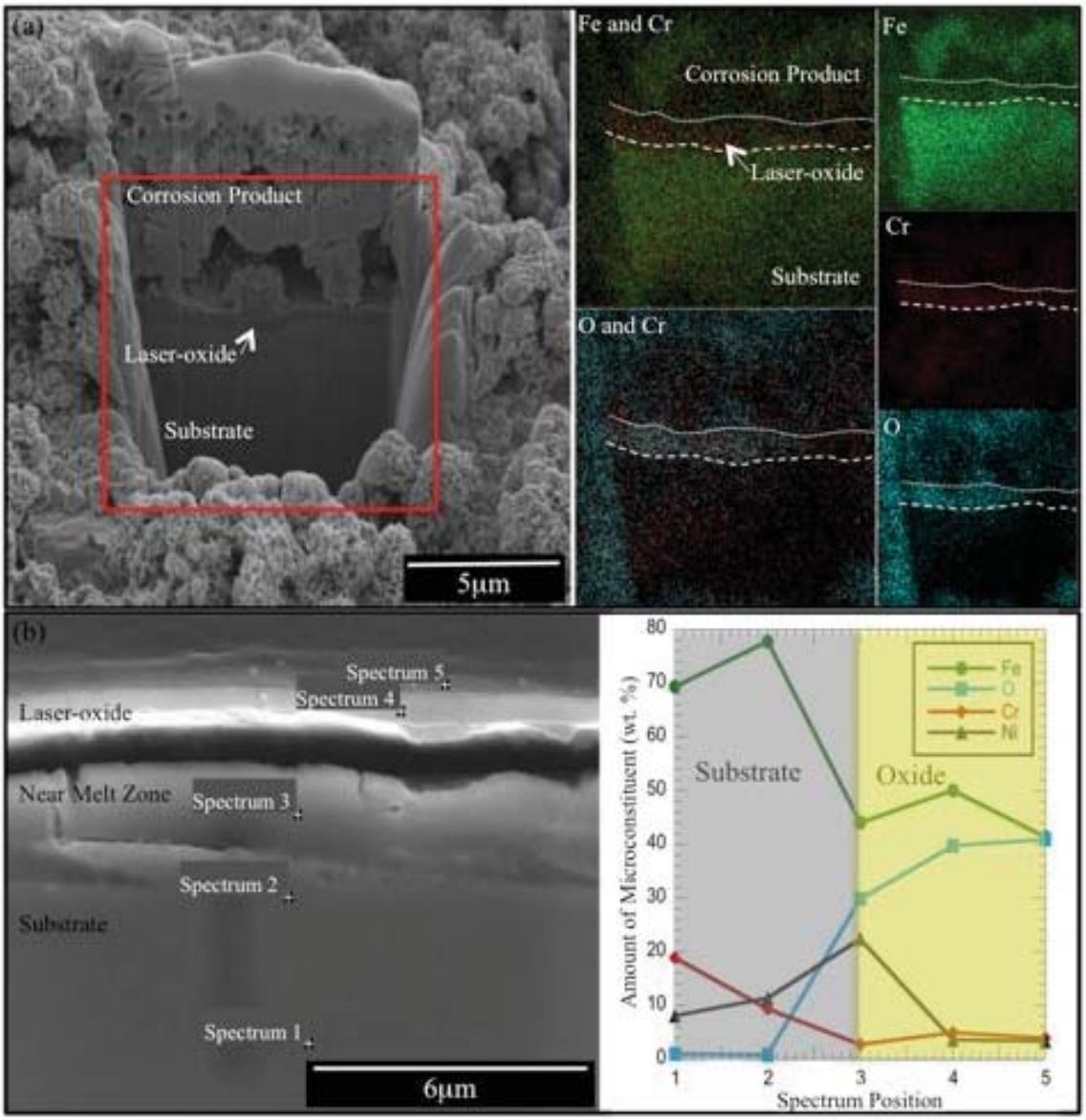

Figure 6.4 (a) Electron micrograph showing FIB cut cross-section through corrosion product, oxide, and substrate, with resulting EDS maps of the region (same scale as cross-section). Regions between white dotted lines indicate the laser-fabricated oxide. (b) Linear EDS point profiles of a metallographic cross-section of an as-fabricated oxide. EDS data indicates substrate melt zone is depleted of Cr immediately beneath the oxide.

relax residual tensile stress in the oxide films hinder the ability of the oxide to function as a barrier for the underlying substrate metal. Because all visible substrate is enameled prior to immersion, the pre-existing surface cracks that pervade the oxide area provide the only path for exposure of the Cr-depleted substrate to the aggressive environment. As described in a previous publication,[132] the degree of oxide channel cracking depends on coating thickness, thus it is likely that susceptibility to corrosive attack also depends on oxide thickness and the Cr-depletion depth.

6.3.2 Stainless Steel Salt Spray Testing

In order to verify the proposition that laser processing parameters, and thus oxide thickness, directly impact the corrosion resistance of a particular oxide-substrate system, 12 oxides were fabricated for salt spray testing. An average laser power of 5.6 W and pulse frequency of 225 kHz were chosen to enable a coupled comparison with other published data.[111,132] Table 6.1 summarizes the oxide thicknesses, measured with TEM on FIB cross-sections, as a function of laser scan rate. A qualitative assessment of the severity of corrosion, based on the extent of the corrosion product developed, as a function of oxide thickness suggests that systems composed of thick oxides (> 200 nm) as well as thin oxides (< 80 nm) are susceptible to chloride attack while oxides on the order of 100-150 nm thick are protective. The variation in extent of corrosion product developed as a function of oxide thickness is highlighted in Figure 6.5; micrographs of six oxides as well as a micrograph of the uncoated SS 304L blank are presented for comparison.

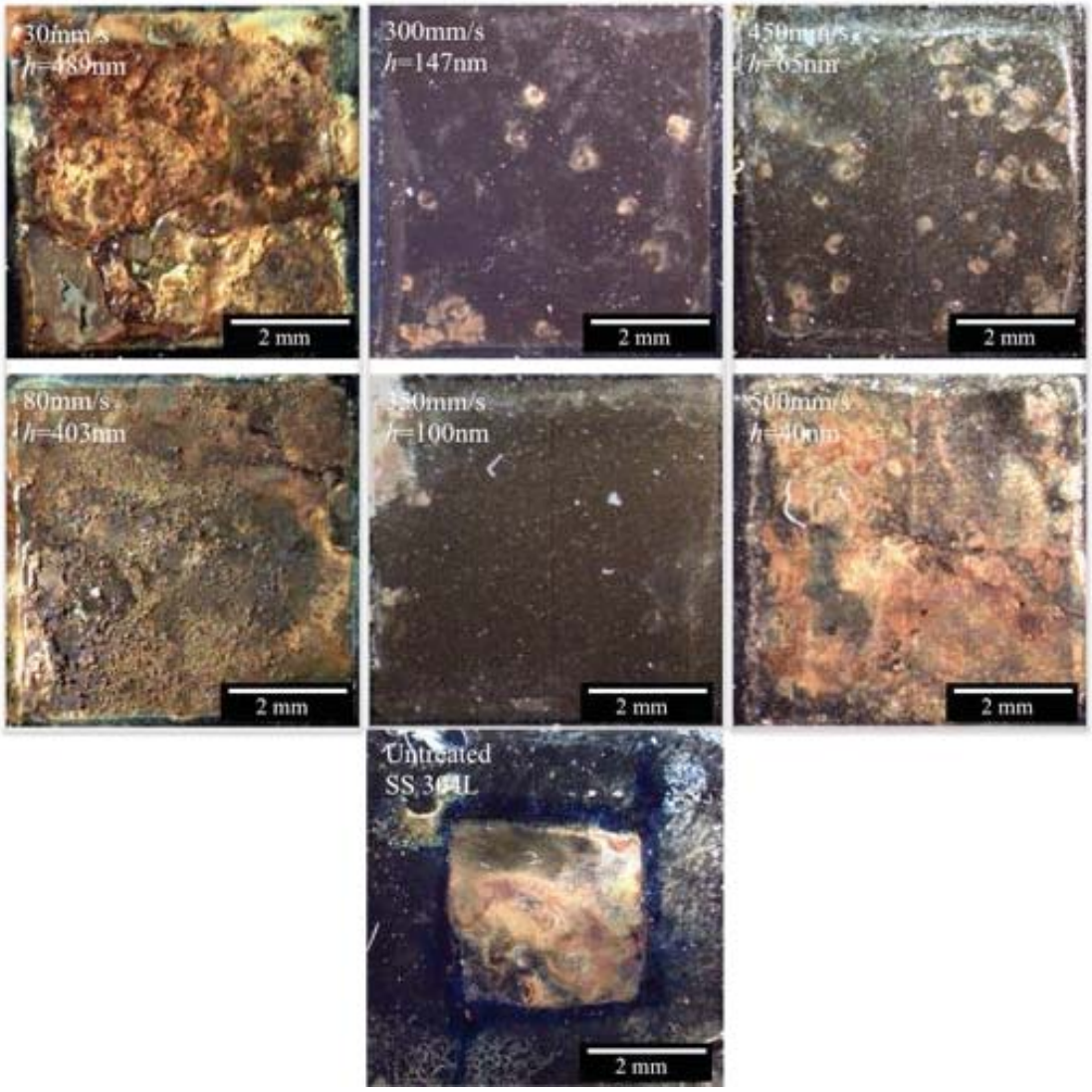

Figure 6.5 Optical micrographs of corrosion product developed on six oxides subjected to 168 hours of salt spray exposure indicate severity of substrate corrosion correlates with oxide thickness and degree of though-thickness channel cracking.

Integrating the current salt spray study with a previous fracture behavior investigation by Lawrence et al.[132] provides insight into the coupling of laser-oxide structure with environmental resistance. Laser-formed oxides with thicknesses greater than ~150 nm suffer from pervasive channel cracking. Through-thickness cracks provide a path for exposure of the substrate immediately beneath the oxide to the aggressive

environment. The Cr-depleted SS 304L substrate is susceptible to chloride attack and thus an extensive corrosion product deposits on top of the exposed area.

Electron microscopy of oxide surfaces after salt spray exposure and subsequent cleaning to remove excess corrosion product reveal the development of pits at triple points or other crack junctions, as shown in Figure 6.6a-b, and widening of surface channel cracks as in Figure 6.6c. These post-mortem observations seem to support through thickness cracks as the likely ingress path for chloride ions. Additionally, in cases where the entire oxide area is not covered by a corrosion product, rings of corrosion product are evident around pits formed at crack junctions (Figure 6.6a) indicating that the first corrosion product is likely formed around these weak points. In some cases, removal of the thick corrosion product reveals oxide degradation, but not complete dissolution, in the vicinity of widened cracks or pits, as in Figure 6.6c, indicating that channel cracks are weak points in the film where corrosion of both the substrate and oxide can proceed. Based on these observations, we can propose the following mechanism: (1) pits develop at channel crack junctions, (2) pits grow and cracks widen with continued exposure, (3) surface dissolution proceeds as additional pits form and cracks widen, (4) substrate corrosion likely accompanies (3) and causes deposition of a corrosion product on top of the laser-fabricated oxide, initially in rings around open pits. Schematics of degradation processes are shown in Figure 6.6d-e. Other investigators have also correlated the corrosion susceptibility of coated steels to coating thickness[133] and to residual film stresses and degree of film cracking.[134] Chou et al. found that salt spray testing led to increased corrosion rates for TiN-coated 304L below a critical thickness, while Shieu et

al. determined that the propensity for film cracking increases with residual film stress, which leads to increased corrosion rates in NaCl environments.

In the current study, laser-oxides with thicknesses less than ~100 nm have no visible channel cracking, suggesting the films are thin enough to avoid significant residual stresses and thus deform in union with the stainless steel substrate. Such thin oxides, with a likely composition of $MnCr_2O_4$,[111] do not serve at as a protective barrier preventing corrosion of the Cr-depleted substrate and it is possible the films are susceptible to degradation in a chloride-rich environment. Thin oxides may be unprotective due to high defect densities; defects can act as easy diffusion paths for the aggressive species. A previous investigation of electrical properties of these films suggested that oxides fabricated at fast laser scan rates, which results in very thin films, have a lower electrical resistivity.[132] In contrast with fracture behavior, film conductance does not depend on oxide thickness; rather, increasing defect density (which corresponds to increasing charge carrier concentration) is identified as the cause. Other investigations have linked the electrical and chemical properties of passive films and thermally grown oxides on stainless steel.[135–139] Guo et al.[136] found that that the electrical conductivity of passive films on a duplex stainless steel varies as a function of film thickness and composition; films less than 5 nm thick are p-type semiconductors and have a higher Cr:Fe ratio than 5 nm thick films, which are n-type semiconductors. Hakiki et al.[135] notes that the electronic structure of relatively thick thermally grown oxides (TGO) on 304 stainless steel is similar to that found for thin passive films. The TGO films are dual phase, with a Cr- and Fe-rich inner layer and an Fe-rich outer layer, with different semiconductivities. The authors found that both TGO and passive films reveal similar

capacitance despite different thicknesses and donor densities, similar to the results of the current study. In the current investigation, thin oxides are fabricated at very high laser scan rates and are thus thought to contain a larger defect density than oxides fabricated at slower laser scan rates. Defects, acting as charge carriers, may also enhance diffusion of the aggressive species to the Cr-depleted substrate,[140] increasing the likelihood of corrosion. Thus, it is specific processing parameters that affect the defect structure in the oxide, leading to poor corrosion resistance, rather than the thickness of the oxide films.

Conversely, laser-formed oxides with thicknesses of ~100-150 nm are protective. These films have thicknesses below the critical thickness for through-thickness channel cracking. They are continuous, well-adhered coatings, likely with a relatively low defect density. These oxides are also likely single-phase coatings with a Cr-rich composition containing some Mn and Fe and may, therefore, be inherently resistant to atmospheric chloride attack. Thus, in the absence of any pre- or post-processing to avoid the development of a Cr-denuded zone in SS 304L substrates, protective oxides can be fabricated under laser processing conditions which result in coating thicknesses in the range of 100-150 nm.

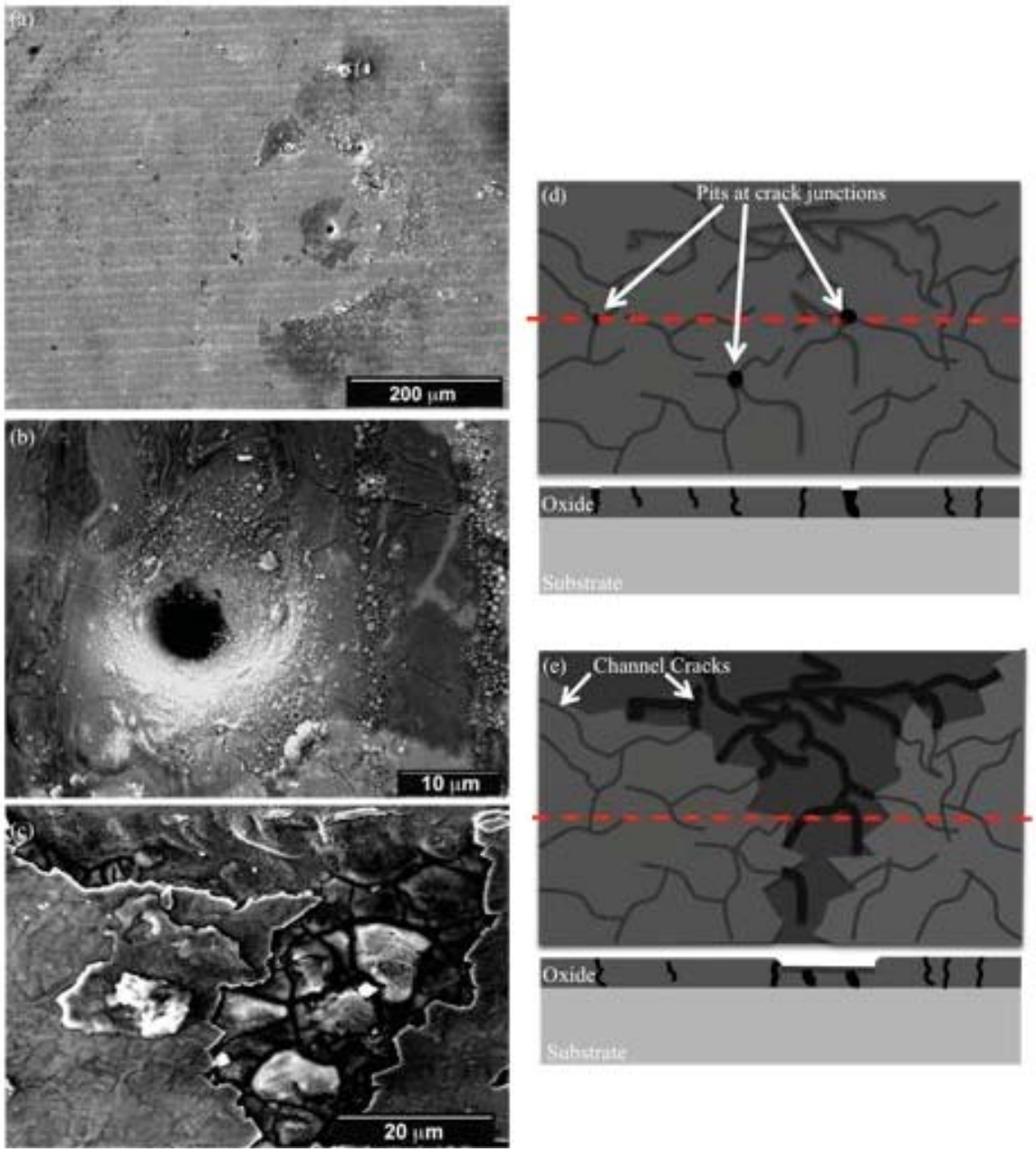

Figure 6.6 Electron micrograph of two pits in a 175 mm/s oxide (a). Apparent horizontal lines on the surface reflect the laser scan direction. Pits form at the intersection of channel cracks, as shown in (b). A schematic of this process is shown in (d). Salt spray exposure also causes widening of channel cracks and subsequent "flaking-off" of the oxide as evident in the SEM image in (c) and accompanying schematic (e). Cross-sections shown below plan-view schematics in (c) and (e) are taken along dashed lines.

6.3.3 Potentiodynamic Testing of Stainless Steel

Figure 6.7 summarizes the anodic polarization curves for the un-treated SS 304L and four oxides fabricated at laser scan speeds of 30 mm/s, 300 mm/s, 350 mm/s, and 500 mm/s, resulting in oxide thicknesses of 489 nm, 147 nm, 100 nm, and 40 nm, respectively.

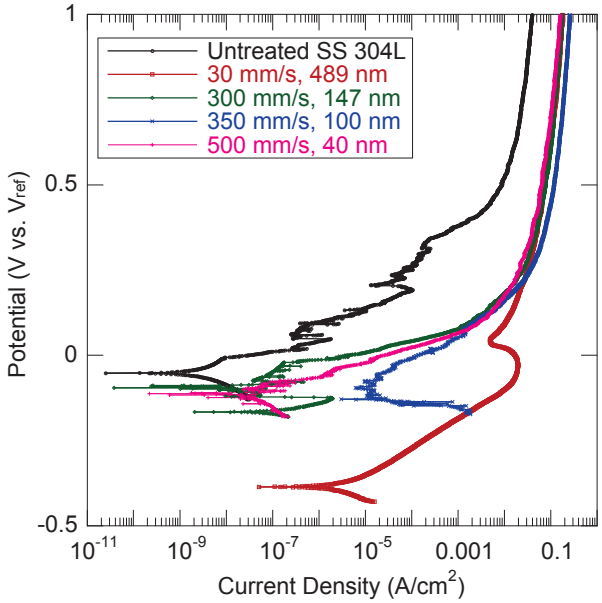

Figure 6.7 Anodic polarization curves of an untreated SS 304L sample, as well as four laser-fabricated oxide samples, a subset of the samples subjected to salt spray testing.

Oxides with thickness of 147 nm, 100 nm, and 40 nm have anodic current densities and corrosion potentials slightly lower than those of the untreated SS 304L, indicating the oxide-substrate systems are more susceptible to localized corrosion. Corrosion potential appears to vary directly with oxide thickness; thicker oxides are the most susceptible to pitting corrosion. In contrast with the immersion and salt spray tested samples, anodic polarization causes degradation of the oxide film and localized corrosion of the substrate, likely through pitting or a crevice corrosion mechanism. As expected, the

untreated SS 304L exhibits pitting. Figure 6.8 compares optical micrographs of oxide areas before and after anodic polarization and shows the degree of local corrosion observed for the oxides and untreated SS 304L. In light of post-mortem microscopy, the propensity for a thick oxide to pit tracks with the prevalence of channel cracks. Notably, no corrosion product was observed to accompany local corrosion. In sum, the 147 nm and 100 nm thick oxides appear more resistant to degradation than the 40 nm oxide. The 489 nm begins to dissolve immediately after the corrosion potential is reached. The corrosion potential for this oxide shifts to a more cathodic value than that of the thinner oxides, reflecting a higher corrosion rate, consistent with salt spray test results. Again, it is likely that the larger Cr-denuded zone generated during fabrication of the 489 nm oxide results in a substrate more susceptible to chloride attack and the channel cracks found in the oxide allow the electrolyte to penetrate the oxide, exposing the Cr-depleted substrate. It is also possible that this process leads to crevice-type corrosion resulting in spallation of the oxide film (Figure 6.8i-j). Similar observations have been recorded by Pacquentin et. al.[124] for SS 304L modified with laser surface melting using an ytterbium-doped nanosecond pulsed laser.

The authors note that when LSM results in the growth of an oxide with a thickness on the order of 300 nm, the film is mudflat cracked and a chromium depletion zone was detected immediately beneath the oxide. Passive behavior disappears and the pitting potential of this sample becomes more negative than for untreated samples or those with oxide coatings on the order of 100 nm.

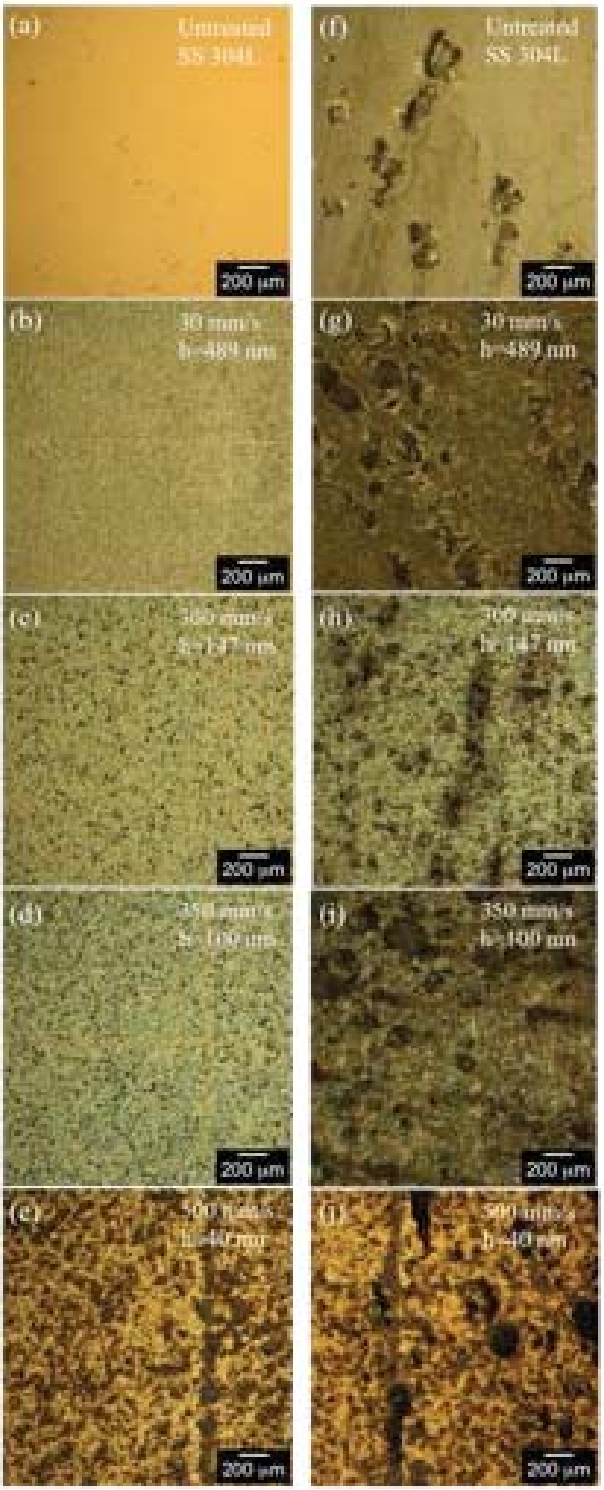

Figure 6.8 Optical micrographs of samples subjected to anodic polarization. Images (a-e) show sample surfaces prior to polarization, images (d-j) show degradation of surface (pitting) after anodic polarization.

6.3.4 Titanium Salt Spray Testing

Exposure to 5% NaCl fog for 168 hours caused no discernible degradation of the laser-fabricated oxide, nor any corrosion of the Ti substrates. Figure 6.9 presents optical micrographs of selected as-fabricated samples after salt spray exposure, while Figure 6.10 shows higher magnification optical micrographs of selected oxides before and after exposure. No oxide color change occurs, the highly polished surface finish of the Ti substrates is not diminished, and no corrosion product has developed. Though it is well known that grade II titanium is resistant to chloride attack, this study confirms that laser processing does not alter the substrate in such a way that would make the oxide-substrate system susceptible to corrosion.

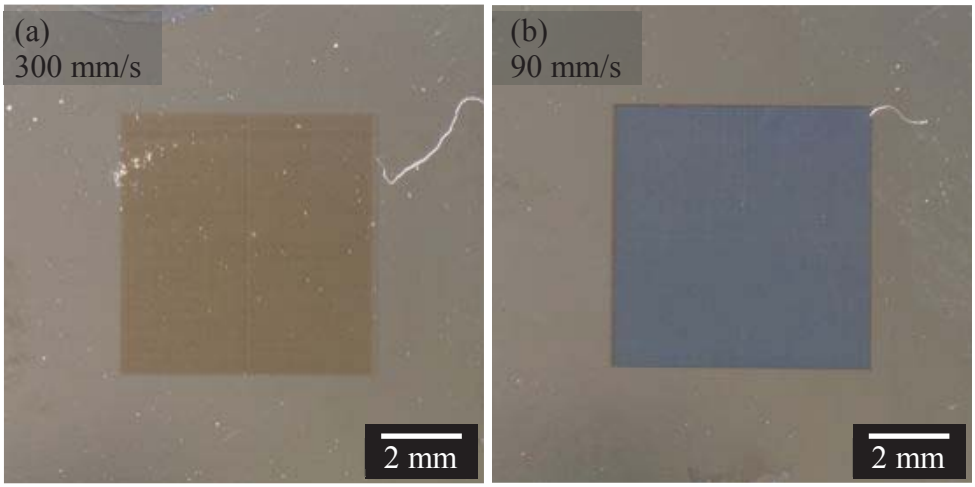

Figure 6.9 Optical micrographs of two oxides fabricated on Ti after salt spray exposure. These micrographs are representative of the response of all oxide systems. Neither the Ti substrate nor the oxides have degraded after 168 hours of salt fog exposure.

Additionally, it is important to note that though the oxides are pre-cracked (as shown previously in Figure 4.2), these through-thickness channel cracks do not affect the corrosion resistance of the system. Previous investigations have shown that CPII Ti can

be susceptible to crevice corrosion in NaCl environments;[141] the channel cracks in the coatings currently under investigation do not, however, appear to create a situation whereby crevice corrosion can proceed.

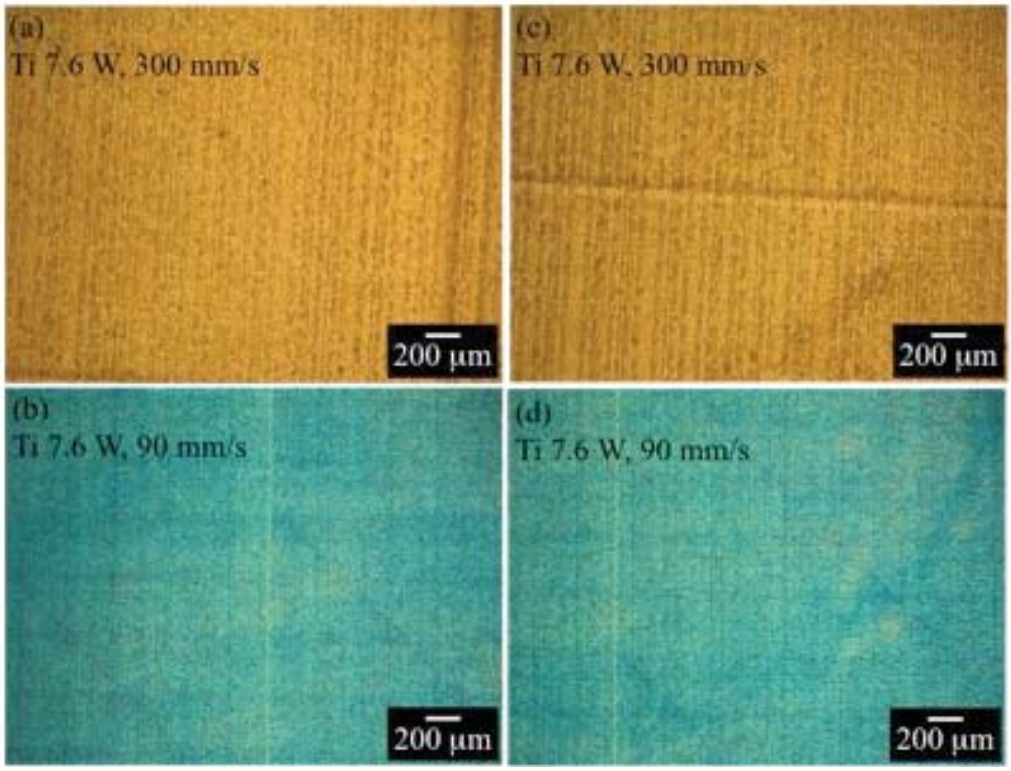

Figure 6.10 Higher magnification optical micrographs of two laser-fabricated oxides on Ti before (a-b) and after (c-d) salt fog exposure. No color change or corrosion product is detected on the surface.

6.3.5 Potentiodynamic Testing of Titanium

Figure 6.11 summarizes the anodic polarization curves for the untreated Ti and six laser-fabricated oxides. Corrosion potential increases directly with oxide thickness (inversely with laser scan speed) and, in all cases, is anodic to the untreated base material. Also, the anodic current densities for all the coated samples are greater than that of the untreated substrate. Though Ti is resistant to corrosion in chloride containing solutions,

the polarization data suggests that thicker oxides would provide an additional protective barrier in anticipated service environments. Similar results have been observed by other researchers investigating surface modification of Ti titanium alloys with plasma-spray coatings and thermal oxidation.[142,143]

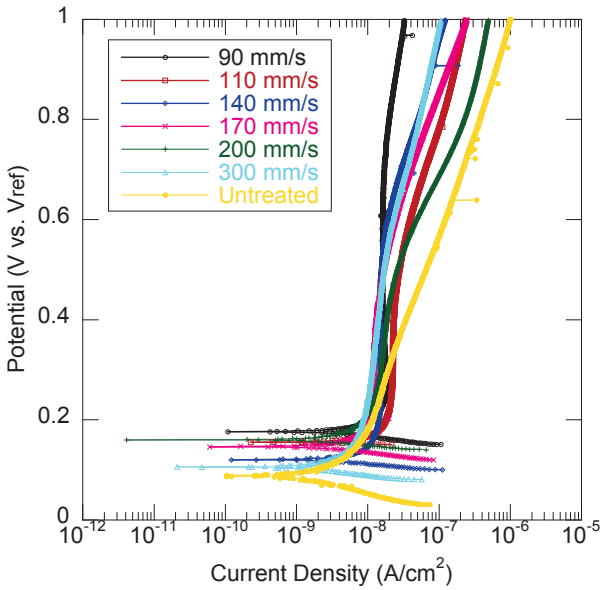

Figure 6.11 Anodic polarization curves of an untreated CPII Ti substrate as well as six laser-fabricated oxides.

6.4 Conclusions

Corrosion resistance of a novel oxide-substrate system fabricated via nanosecond pulsed laser irradiation of SS 304L and CPII Ti substrates in chloride containing environments, similar to marine conditions, has been investigated through immersion testing, salt spray exposure, and anodic polarization in NaCl solution. Environmental exposure results are interpreted in terms of previous investigations of oxide structure and fracture behavior.

1. Laser grown oxides on CPII Ti are resistant to degradation in chloride containing environments. Crevice corrosion is not a problem despite pervasive channel cracks in oxide surfaces. Oxides increase anodic current density and corrosion potentials of the oxide-substrate system.
2. Laser grown oxides on SS 304L with thicknesses greater than 150 nm are generally non-protective in chloride-containing environments, likely due to the presence of through-thickness cracks, allowing exposure of the Cr-depleted substrate to the aggressive environment. High temperature laser processing leaves a Cr-denuded zone in the substrate that extends to about half of the melt zone depth; this Cr-depleted substrate microstructure is susceptible to corrosion in chloride environments, thus a corrosion product deposits atop the exposed laser-formed oxide areas.
3. Laser-oxides on SS 304L with thicknesses less than ~100 nm are a single-phase $MnCr_2O_4$ and do not contain through-thickness cracks[132], but do not prevent corrosion of the Cr-depleted stainless steel substrates. These films likely have high defect densities that may act as short circuit diffusion paths for the aggressive species, enabling corrosion of the Cr-depleted substrate.
4. Oxide coatings grown on SS 304L with pulsed laser irradiation in ambient environments that have thicknesses in the range of ~ 100-150 nm are protective in aggressive chloride environments. Oxides in this thickness range are single-phase and not mudflat-cracked and as such are resistant to atmospheric chloride attack, but still susceptible to localized electrochemical corrosion.

Thus, nanosecond pulsed laser irradiation can be successfully employed to fabricate robust, protective oxide coatings on both CPII Ti and SS 304L substrates. Processing parameters can be tailored to achieve continuous, well-adhered oxides with a phase structure that is resistant to degradation in chloride containing environments despite the existence of a Cr-depleted region in the stainless steel substrate microstructure. Further pre- or post-processing may be employed to reduce the detrimental effect of Cr-diffusion during laser processing, thereby increasing the thickness range for robust, protective coatings.

CHAPTER 7. DEVELOPING MECHANICALLY AND ENVIRONMENTALLY STABLE OXIDES ON STAINLESS STEEL USING NANOSENCOND PULSED LASER IRRADIATION

7.1 Introduction

Highly colored films fabricated using nanosecond pulsed laser irradiation are under investigation for use as authenticity markings[144,145] as a protection against counterfeiting, and as a method for monitoring degradation in welded or sealed components, provided they are mechanically robust and do not degrade the overall system resistance to harsh environments.

Oxide films that could be used as authenticity markers must adhere strongly to the substrate and lead to a substrate-oxide system that is both mechanically robust and resistant to degradation in the projected exposure conditions. The most aggressive anticipated service condition is the marine environment; a previous study (Chapter 6) evaluated the environmental stability of laser-fabricated oxides on 304L stainless steel. Austenitic stainless steels are susceptible to pitting in chloride-rich environments.[146] Various investigations of the corrosion behavior of laser-treated stainless steels suggest that corrosion resistance depends on structure, morphology, and Cr concentration of the laser-treated area.[124–126] The data evaluated in Chapter 6 confirmed that oxide structure and base metal Cr concentration impact the corrosion susceptibility of oxides grown on

SS 304L using nanosecond-pulsed laser irradiation. The current study focuses on a first step towards mitigating the corrosion caused by Cr depletion and severe oxide channel cracking by altering the laser treatment process. Working from an understanding of effect of oxide thickness on residual stress, individual layer thicknesses are kept small, but multiple layers are grown in a single exposure area. The effect of this layering process is investigated in terms of surface structure and morphology, color, mechanical properties, and corrosion resistance.

7.2 Experimental Procedures

Austenitic stainless steel 304L substrates, with a composition in wt.% of 18.11% Cr, 8.00% Ni, 1.63% Mn, 0.42% Si, 0.14% Mo, 0.083%N, 0.025% S and P, 0.023% C, balance Fe, were prepared for laser processing by metallographic grinding with 180 grit SiC paper and polishing with 9, 6, and 3 mm diamond suspension. Final cleaning involved rinsing in Lenium^{TM} degreasing solvent, followed by acetone, and then alcohol. Final sample dimensions were 12.5 × 12.5 × 3.4 mm. An Er-doped, pulsed fiber laser from SPI Lasers was used to irradiate the polished substrates in ambient atmospheric conditions, stimulating oxide growth. This infrared laser (1064 nm wavelength) was operated with a pulse duration of 120 ns, an average power of 5.6 W, a pulse frequency of 225 kHz, and scan speeds of 475 mm/s and 550 mm/s. The focused laser beam was approximately Gaussian with a $1/e^2$ width of 59 μm. Multiple overlapped laser scan lines with a centroid-to-centroid (hatch) spacing of 10 μm created square oxide areas. A single oxide fabricated with a laser scan speed of 475 mm/s has a thickness of ~50 nm. Oxides with total thicknesses of 100 nm, 200 nm, and 300 nm were developed by sequential

irradiation of the same 6 mm x 6 mm area, creating films of 2 layers, 4 layers, and 6 layers, respectively. A single oxide film fabricated at 550 mm/s is approximately 25 nm thick. At this scan rate, films with total thicknesses of 75 nm, 125 nm, and 300 nm were fabricated by irradiating the same area, building layered films consisting of 3 layers, 5 layers, and 12 layers.

Instrumented nanoindentation, employed to measure mechanical properties of the as-fabricated oxide films, was conducted with a Nanoindenter XP with a dynamic contact module (DCM) for low load testing, the continuous stiffness module (CSM), with tests performed at a frequency target of 75 Hz, a depth target of 1 nm, and depth limits at least 200 nm larger than the total film thickness. A Berkovich probe with a radius of approximately 150 nm was used for mechanical property testing. Dynamic indentation measures contact stiffness, S, from which reduced modulus, E_r, can be determined knowing that:[7]

$$S = \beta \frac{2}{\sqrt{\pi}} E_r \sqrt{A}, \qquad \text{Equation 7.1}$$

where A is the contact area and b is a constant which has traditionally been used to account for stiffness deviations resulting from axial asymmetries of pyramidal indenters, and is generally taken as 1.034 for Berkovich indenters. The sample modulus, E, is then computed by:

$$\frac{1}{E_r} = \frac{(1-\nu^2)}{E} + \frac{(1-\nu_i^2)}{E_i}, \quad \text{Equation 7.2}$$

where ν is Poisson's ratio of the sample (0.3), ν_i is Poisson's ratio of the indenter (0.07), and E_i, is the modulus of the indenter (1141 GPa).

Optical interferometry was conducted to measure surface roughness of the oxide samples using an ADE Phase Shift white light interferometer. Images were collected at a magnification of 1 with a 10X objective. Values for average roughness, RMS roughness, and peak-to-valley distance were recorded.

A Varian, Inc. Cary 5000 UV-visible-IR spectrophotometer was used to analyze the reflectance of the oxide coatings; Cary WIN UV Color software was then used to evaluate chromaticity. For this analysis, samples were fixtured within an internal diffuse reflectance accessory such that the specularly reflected beam was detected. A reduced slit was employed to ensure only the reflectance of the laser-fabricated oxide was measured. Reflectance was monitored over a range of incident wavelengths from 350-850 nm. CIE 1931 photopic observer and D65 illuminant standards were utilized for this evaluation.

Anodic polarization tests were conducted on an untreated stainless steel blank and on all layered oxides to evaluate the pitting corrosion resistance and general localized corrosion behavior of the oxide-substrate system. Anodic polarization tests were performed with a conventional three-electrode cell, with a Pt counter electrode and a Ag/AgCl reference electrode, using a Gamry DC105 corrosion test system. Polarization curves were produced in a 3.5% NaCl solution, which was not de-aerated, at a sweep rate of 0.5 mV/s after stabilization of the open circuit potential.

Salt spray exposure was performed in accordance with the ASTM B117 standard[128] for 168 hours. A polished blank SS 304L specimen was included in the test matrix as a control sample. All stainless steel substrates were enameled to ensure that only oxide areas were exposed to the salt air environment. Samples were rinsed and dried for at least 24 hours prior to microscopy.

Interferometry and spectrophotometry were conducted on the specimens after electrochemical testing, following the methods described previously.

7.3 Results and Discussion

Hardness and elastic modulus values of layered laser-fabricated oxides obtained with dynamic nanoindentation are collected in Table 7.1. Since mechanical properties of thin films can vary with film thickness, and can be influenced by surface asperities and roughness as well as substrate properties, a condition for comparing properties among samples must be defined. Consistent with previous investigations of laser-fabricated oxides[113,132], we have selected this comparative parameter as the indentation contact depth for which the ratio between the contact radius, a_c, and the film thickness, h, is in the range of 0.5–1.0. Selecting depth as a comparative parameter for extracting film properties minimizes the effects of surface asperities and substrate properties.[115,116] For this analysis, contact area is determined from:

$$a_c = \sqrt{\frac{A}{\pi}}, \qquad \text{Equation 7.3}$$

where A is the projected area of the elastic contact and is calculated by solving Eq. (1) for A. For both laser scan rates used in this study, modulus decreases slightly as the total film thickness/number of layers decreases. The thinnest films also have the lowest hardness values, but, interestingly, the mid-thickness films (4 layers for 475 mm/s, 5 layers for 550 mm/s) are slightly harder than the thickest films. Quasistatic, load-controlled indentation

was performed to check this result—consistent values and trends are obtained with both techniques.

Table 7.1 Modulus and Hardness values calculated from continuous stiffness nanoindentation.

No. Layers	*Modulus (GPa)*	*Hardness (GPa)*
	475 mm/s	
6 layers	165.75±12.2	9.8±1.7
4 layers	158.7±15	10.7±1.8
2 layers	143.2±17	8.3±1.5
	550 mm/s	
12 layers	173.8±12	9.6±1.5
5 layers	161.5±21	10.2±1.6
3 layers	135.3±17	7.3±1.8

Optical interferometry reveals that the surface roughness of the oxides is inversely proportional to the number of layers in the film both in the as-fabricated and corroded states. Roughness increases dramatically after anodic polarization. Values for the average roughness, *Ra*, RMS roughness, *Rq*, and peak-to-valley distance, *PV*, are collected in Table 7.2. In general, the RMS roughness value is about 20% greater than the *Ra* value, because *Rq* is weighted by large values of peak height and valley depth. The disparity between peak height and valley depth increases substantially after anodic polarization, due to the degradation of the oxide layer and resulting pits or crevices, as shown in Figure 7.1. The *PV* values post-polarization correspondingly increase. However, the *PV* increase is less dramatic for the oxides fabricated at 475 mm/s than the oxides fabricated at 550 mm/s.

Spectrophotometry data is used to calculate chromaticity values for each of the layered oxides. Chromaticity is a quality of color determined by hue and intensity,[147] and

Table 7.2 Values for the average roughness, *Ra*, RMS roughness, *Rq*, and peak-to-valley distance, *PV,* measured with optical interferometry.

No. Layers	*Pre/Post Polarization*	*Ra*	*Rq*	*PV*
	475 mm/s			
6	Pre	0.2152	0.2729	2.676
6	Post	0.3578	.4503	7.407
4	Pre	0.2453	0.3134	3.531
4	Post	0.4805	0.6308	16.11
2	Pre	0.2521	0.3204	2.831
2	Post	0.3131	0.4413	18.17
	550 mm/s			
12	Pre	0.3187	0.4077	3.724
12	Post	0.3223	0.4130	4.902
5	Pre	0.2246	0.2858	2.580
5	Post	0.4460	0.5956	9.271
3	Pre	0.1857	0.2372	3.137
3	Post	0.3031	0.4350	13.12

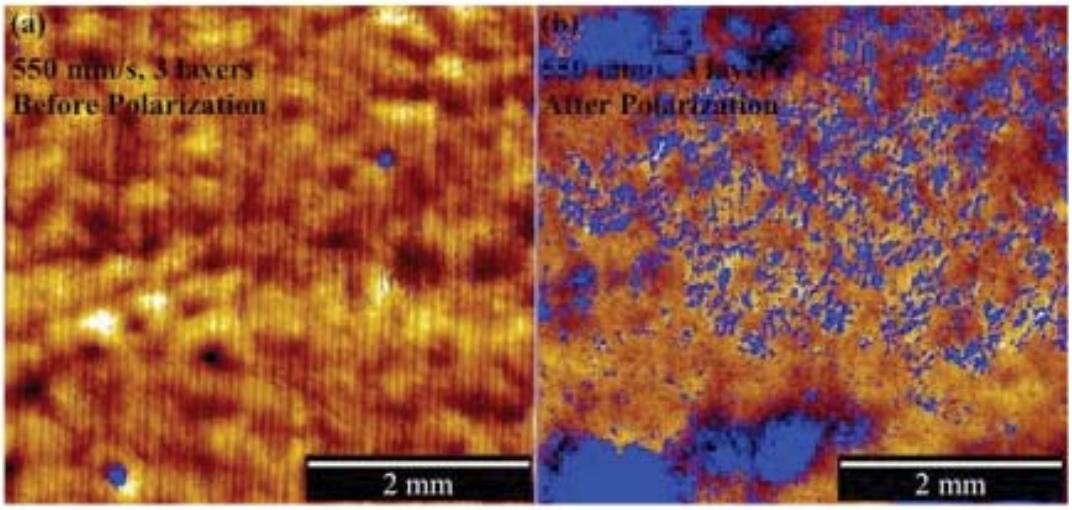

Figure 7.1 Optical interferograms of a 550 mm/s, 3 layer oxide before (a) and after (b) anodic polarization, showing increase in roughness from pitting.

as Cartesian coordinate values are easily calculated, chromaticity information could be archived as a mechanism for counterfeit detection.[111] The x- and y-chromaticity coordinates, determined by implementing a CIE 1931 standard photopic observer and

D65 illuminant standard, are plotted in Figure 7.2, and are overlaid on the CIE 1931 color space.[148,149] As indicated by Adams et al.[111] untreated 304L stainless steel substrate

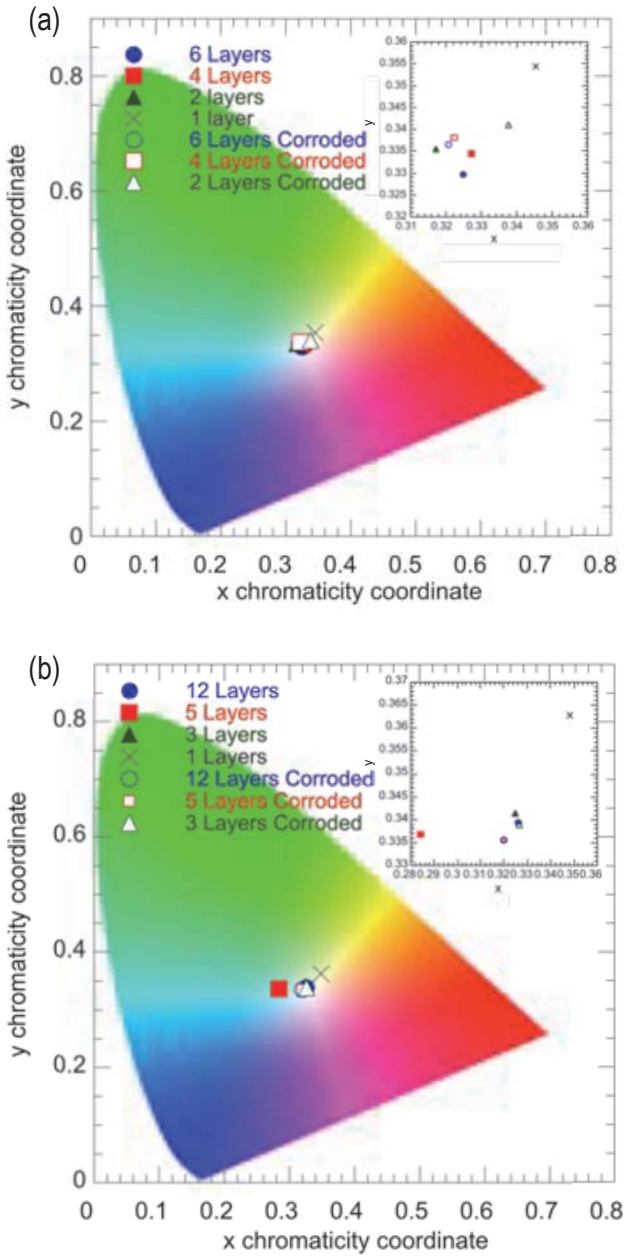

Figure 7.2 X- and y-chromaticity coordinates for 475 mm/s layered oxides (a) and 550 mm/s layered oxides, before and after anodic polarization are overlaid on the CIE 1931 color space.

has chromaticity of x=0.315, y=0.334; chromaticity values which lie in the interior of the CIE color space are unsaturated. Anodic polarization results in a shifting of chromaticity values. Both x- and y-coordinates decrease after polarization of oxides grown using a scan speed of 550 mm/s. Conversely, for oxides grown at 475 mm/s the y-coordinates increase, the x-coordinate of the 2 layer film increases, and x-coordinates of the 4 layer and 6 layer films decrease. The total shifts are minimal, but correspond to film degradation during anodic polarization.

Potentiodynamic anodic polarization curves of oxides grown at a laser scan rate of 475 mm/s and 550 mm/s are presented in Figure 7.3a and 7.3b, respectively. The anodic polarization curve for untreated SS 304L is included for comparison on both plots. The untreated SS 304L behaves as a typical passive metal subjected to pitting corrosion.[150] Stainless steel is known to be susceptible to pitting at low potentials in chloride containing solutions; in this case, pitting effectively begins at 0 V vs. Ag/AgCl. Furthermore, anodic current densities at the highest polarization potentials are large and limited by concentration polarization phenomena.

Oxides grown at both 475 mm/s and 550 mm/s show no improvement in localized corrosion resistance compared with the untreated steel, as the corrosion potentials for all laser-treated samples are more cathodic than for the virgin SS 304L. Additionally, all laser treated samples show an increase in anodic current densities compared with the untreated material and are concentration polarization limited at large polarization potentials. Comparing the oxides fabricated at 550 mm/s reveals that the breakdown potential for the 3-layer film is slightly more noble than for the 5-layer film, both of which are more noble than the virgin SS 304L. In contrast, the 12-layer film shows only

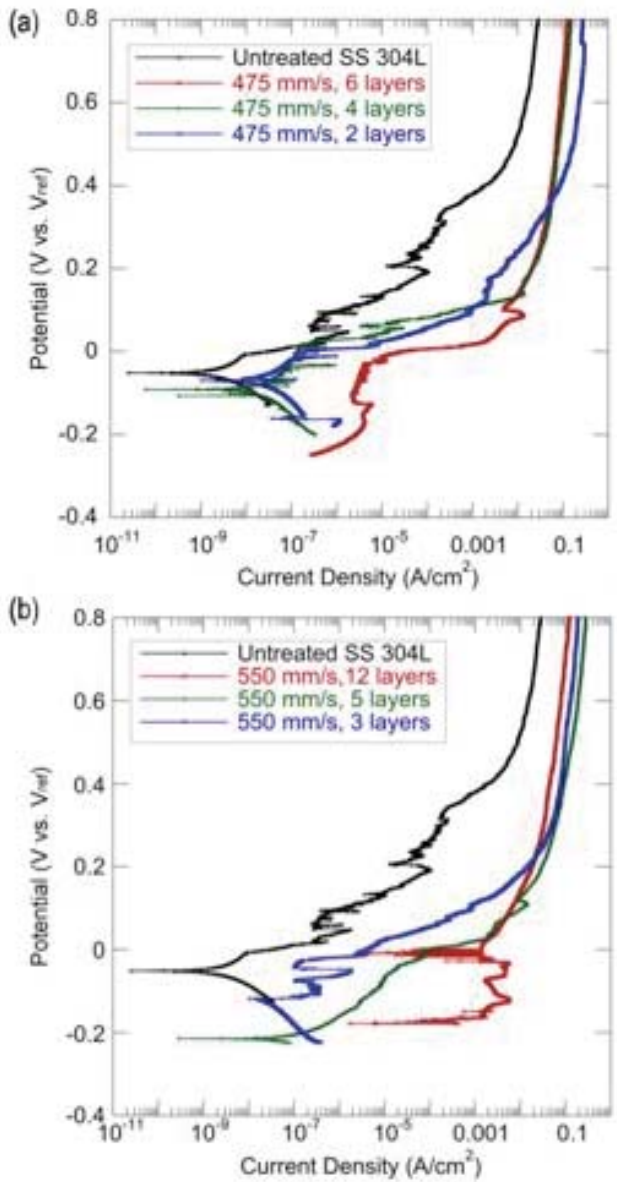

Figure 7.3 Anodic polarization curves generated for layered oxide films fabricated at 475 mm/s (a) and 550 mm/s (b).

active behavior, which is once again concentration polarization limited. Oxides grown at 475 mm/s behave similarly; the breakdown potential for the 4-layer film is greater than the 2-layer film, both of which are greater than the 6-layer film and the untreated SS 304L. The 6-layer film appears to passivate just slightly prior to reaching the breakdown

potential. While the anodic current densities for the 475 mm/s oxides are larger than the untreated steel, they are generally lower than the anodic current densities measured for the 550 mm/s oxides. Similarly the cathodic shift in corrosion potentials is less pronounced for the 475 mm/s oxides than for the 550 mm/s oxides. Thus, in general, oxides fabricated at 475 mm/s are more resistant to localized corrosion than oxides grown at 550 mm/s.

Optical micrographs of the layered oxide films before and after anodic polarization, shown in Figure 7.4 (475 mm/s) and Figure 7.5 (550 mm/s), confirm the electrochemical data. In general, oxide degradation is more severe for oxides grown at 550 mm/s. The pits formed are larger and/or more prolific for the 550 mm/s films. Pitting is more severe for oxides with 3 and 5 layers than for the 12-layer film. Pit morphology is impacted by exposure direction—samples were suspended vertically, thus pits are elongated. Fewer pits are observed for oxides grown at 475 mm/s; those that are observed are less severe than the pits that develop in the 550 mm/s oxides.

Salt spray testing results generally follow the same trends observed in anodic polarization. A corrosion product deposits on the surface of all oxides, as shown in Figure 7.6a-c and Figure 7.7a-c. The most pervasive corrosion product developed on the surface of the 5-layer and 12-layer oxides. The deposition of a corrosion product indicates that the oxides are not impervious to chloride containing solutions and the substrate melt zone is likely still depleted of Cr after laser processing, even for the thinnest films. However, comparing Figure 7.6a-c and Figure 7.7a-c with Figure 6.5 it is evident that corrosion of the substrate is, in general, less severe.

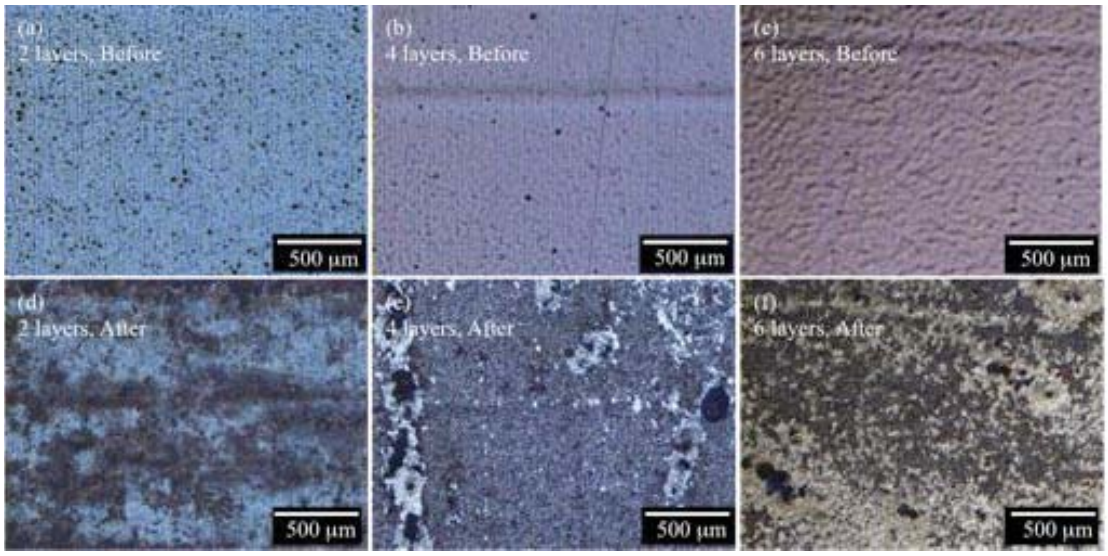

Figure 7.4 Optical micrographs of 475 mm/s layered oxides before (a-c) and after (d-f) anodic polarization in 3.5% NaCl solution.

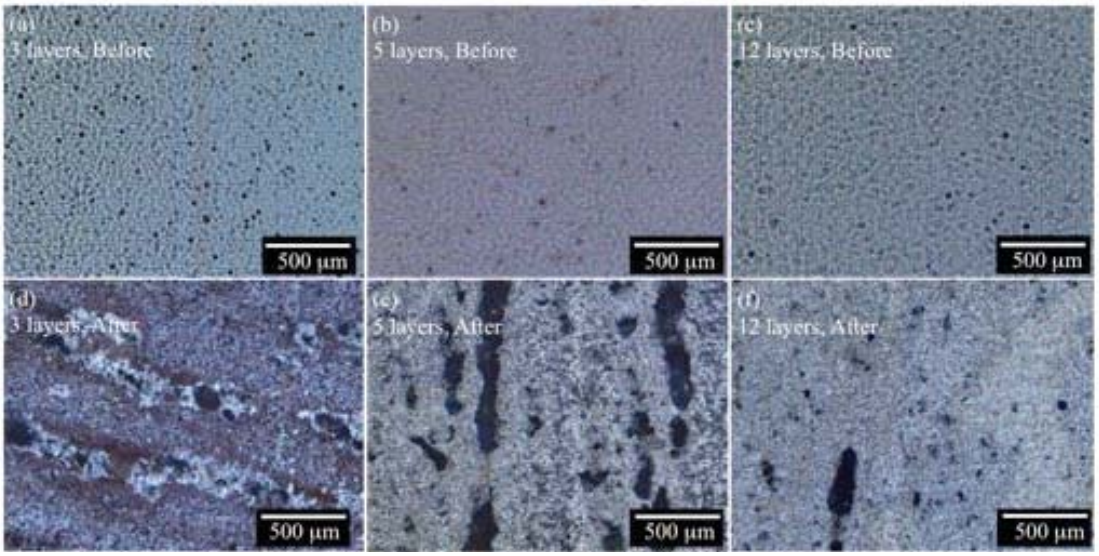

Figure 7.5 Optical micrographs of 550 mm/s oxides before (a-c) and after (d-f) anodic polarization in 3.5% NaCl solution.

Furthermore, upon inspection of Figure 7.6d-f and Figure 7.7d-f, it is clear that the laser-fabricated oxide is still intact after the corrosion product has been removed from the surface, although the surface reflectance is changed due to degradation. The

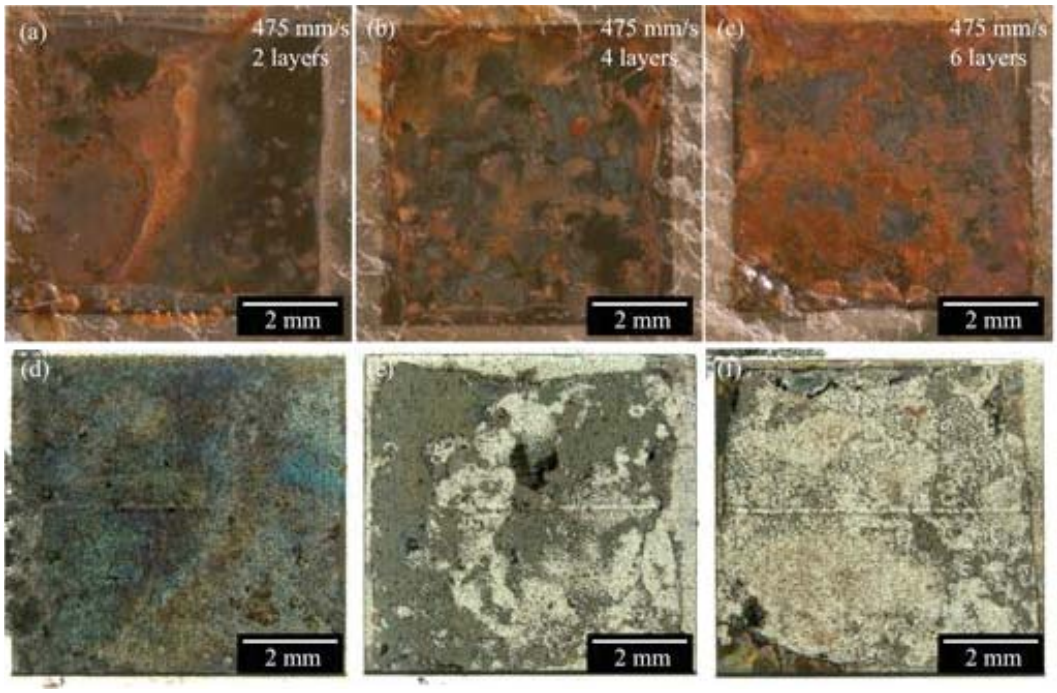

Figure 7.6 Optical micrographs of 475 mm/s layered oxides after 168 hours of salt fog exposure (a-c) and after removing the corrosion product with oxalic acid cleaning (d-f).

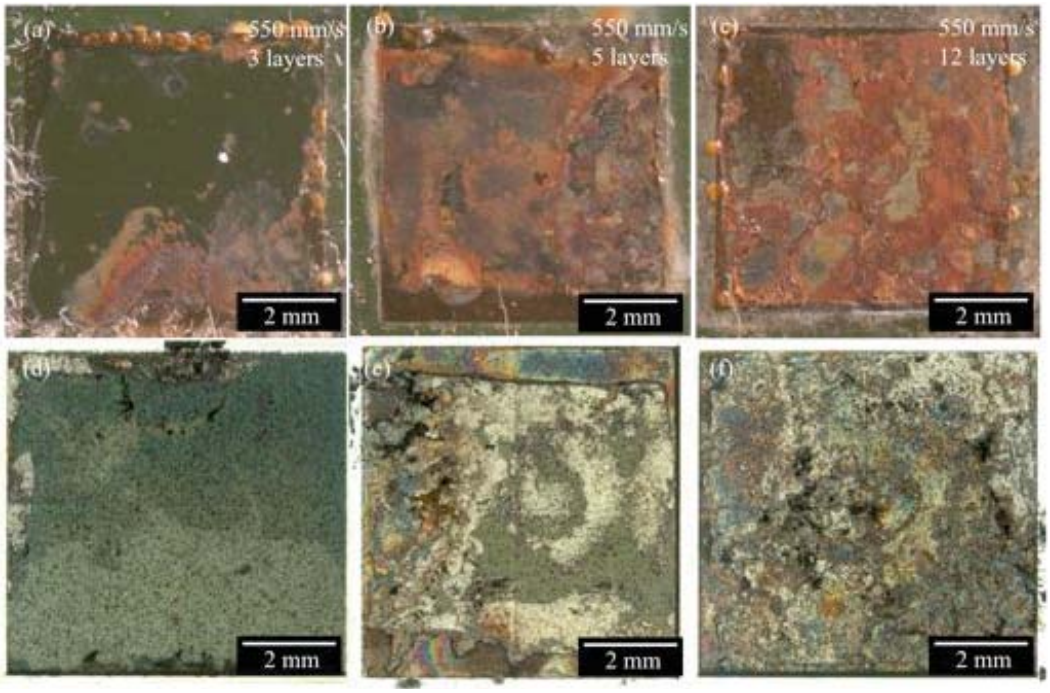

Figure 7.7 Optical micrographs of 550 mm/s layered oxides after 168 hours of salt fog exposure (a-c) and after removing the corrosion product with oxalic acid cleaning (d-f).

samples were cleaned with a natural source of oxalic acid, which is commonly used as a rust remover. This process removed the rust-like corrosion product deposited on top of the oxides, but leaves the oxides intact, indicating that while the oxides are not impenetrable for chloride ions, which can result in substrate corrosion, the coatings do resist chloride degradation to varying degrees. The 3-layer film is the only coating that does not appear to have suffered any dissolution after exposure. Additionally, closer inspection of the oxides with electron microscopy show similar behavior to that seen in the single layer films—namely that channel cracks are the likely points of ingress for corrosive ions, which can cause crack widening, pit development, and some oxide degradation, in addition to substrate corrosion, likely by a crevice mechanism. Figure 7.8 presents electron micrographs of oxides cleaned after salt fog exposure; the 3-layer film shows no discernible surface dissolution but the channel cracks are clearly visible, while surface degradation is obvious for the 12-layer film. In contrast with the single-layer films, all the layered-oxide films manifest channel cracking. Though the residual stresses in these films have not been investigated, the presence of cracks seems to contribute to film degradation and substrate corrosion.

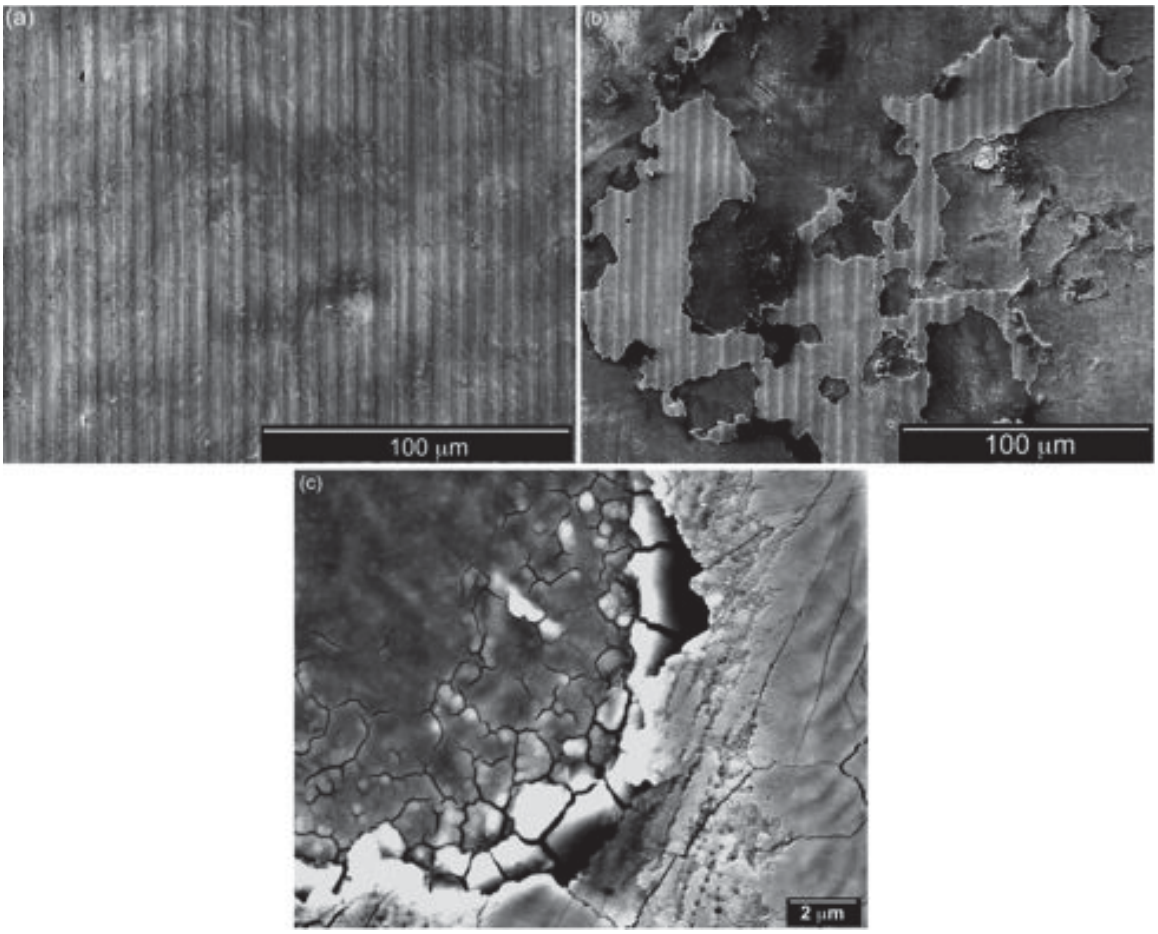

Figure 7.8 Electron micrographs of a 3-layer oxide (a) and a 12-layer oxide (b) after salt fog exposure and subsequent oxalic acid cleaning. No surface degradation is apparent for the 3-layer film, conversely, the 12-layer coating shows severe oxide dissolution; surface channel cracks are still apparent, as shown in (c).

7.4 Conclusions

In an effort to tailor laser processing in order to mitigate the corrosion caused by Cr depletion in the melt zone generated by laser heat input, multi-layered oxides were fabricated on SS 304L. Individual layer thicknesses were kept small, but total layer thickness encompassed the range of thicknesses generated previously for single layer

films. Surface structure and morphology, color, mechanical properties, and corrosion resistance of layered oxides were interrogated.

1. Layered films grown using a laser scan rate of 475 mm/s tend to be more resistant to both localized and general corrosion than oxides fabricated with a scan rate of 550 mm/s.
2. Though the Cr-depleted substrates are still susceptible to corrosion in a chloride-containing environment, any corrosion product that deposits on the surface of the oxides can be removed by cleaning with oxalic acid. Importantly, the laser-fabricated oxide is still present after salt spray exposure and cleaning, suggesting that the oxide is relatively stable in harsh conditions.
3. As with previously investigated single-layer films, layered oxides are considerably harder than the substrate. The overall surface roughness is inversely proportional to oxide thickness and increases after anodic polarization. Additionally, the chromaticity of the oxides changes slightly after localized corrosion, but a general trend may be extracted allowing the chromaticity of the films to be archived.

Nanosecond pulsed laser irradiation can be successfully employed to fabricate layered oxide coatings which are both mechanically robust and resistant environmental degradation.

CHAPTER 8. HYDROGEN-INDUCED MECHANICAL PROPERTY EVOLUTION IN NICKEL

8.1 Introduction

Safe and effective storage and transport of gaseous hydrogen is a vital step towards utilizing hydrogen as an energy carrier. Degradation of metallic systems exposed to hydrogen, especially those used in pressure vessels, tanks, and pipelines can lead to unexpected catastrophic failures. Hydrogen has been linked to a decrease in ductility, fracture strength, and fracture toughness in many metals, i.e., the well-known phenomenon of hydrogen embrittlement, and has resulted in loss of life in engineering failures in the energy industry. Current theories regarding the specific mechanisms associated with hydrogen embrittlement can be grouped into three classifications: (1) hydride formation, where brittle hydride precipitates ease fracture by providing a low energy path, (2) hydrogen-enhanced localized plasticity, where hydrogen impacts local instabilities associated with plastic flow, and (3) decohesion mechanisms where hydrogen at interfaces lowers cohesive strength. The first mechanism has been established as operative when hydrides are thermodynamically stable in materials, or can be stabilized by an applied stress. Materials which suffer from hydrogen-enhanced localized plasticity (HELP) fracture via a highly localized plastic deformation, as compared to embrittlement mechanisms.[151] This mechanism suggests that failure in the presence of hydrogen proceeds by locally ductile processes and that hydrogen enhances rather than retards the

motion of dislocations. In many structural materials, such as high strength steels and nickel-based alloys, hydrogen embrittlement is characterized by decohesion on grain boundaries or interfaces, resulting in low-toughness intergranular fracture in non-hydride forming systems; embrittlement occurs without significant plastic deformation.[152–155] These observations led to the postulate that solute hydrogen decreases the cohesive force, and corresponding surface formation energy, required to separate the crystal along a crystallographic plane, grain boundary, or particle/matrix interface. This postulate, called the hydrogen enhanced decohesion (HEDE) mechanism suggests that dislocation motion is limited to maintain atomically sharp crack tips (though dislocation motion may work to increase stress at decohesion sites by strain gradient hardening[156,157] or similar processes). Hydrogen acts directly at the crack tip and surface diffusion from adjacent parts of the fracture surface is responsible for maintaining the crack tip hydrogen concentration.[157] The interstitial hydrogen concentrations and corresponding elastic stresses required to produce decohesion ahead of a crack are likely quite high; debate surrounds whether they can be achieved simultaneously.[158] However, it may be possible to satisfy the requirements for HEDE at a number of microstructural sites such as: atomically sharp crack tips where surface hydrogen is adsorbed, at positions of maximum hydrostatic stress, or at particle-matrix interfaces ahead of a crack.[159]

Direct experimental evidence for HEDE is difficult to attain due to the lack of techniques for observing atomic-scale events in bulk material. However, high hydrogen concentrations have be observed at critical locations, such as grain boundaries and particle-matrix interfaces[160,161] resulting in increased intergranular fracture in some systems.[162,163] Easier field-evaporation of surface atoms during field-ion microscopy of

Fe using hydrogen as an imaging gas has also been reported supporting the hypothesis that hydrogen can weaken interatomic bonds,[164] thereby reducing cohesive strength. Furthermore, atomistic models suggest that the interatomic bond strength may be weakened by the presence of hydrogen between atomic planes in Al[165] and that solute hydrogen leads to reduction of fracture toughness in high-strength alloys.[166] Fractography utilizing TEM foils has revealed atomically brittle intergranular fracture in materials with impurity segregation at grain boundaries,[167] and atomistic modeling efforts indicate that segregation of S weakens interatomic bonds in Fe and Ni.[168] It is reasonable to extend a similar weakening effect to a small, easily diffusible atom such as hydrogen.

Realizing that a "one size fits all" mechanism explaining observations of hydrogen embrittlement is unlikely, this study seeks to identify specific processes leading to degradation in the presence of hydrogen in an effort to understand the interrelationships between the proposed mechanisms. A model material system, namely commercially pure Ni-201 is chosen for this investigation because it is a representative system for important engineering alloys such as nickel-based superalloys and austenitic stainless steels and because its stacking fault energy is sufficiently high so as to allow dislocation cross-slip. With these material attributes in mind, material response can be predicted for the dominant embrittlement mechanisms, allowing the net mechanism to be identified more easily. For example, if HELP is the dominant mechanism, it is likely that hardness would increase and dislocation cross-slip would be restricted. Conversely, if HEDE is dominant, an overall decrease in bulk modulus (which is inversely related to the compressibility and thus directly related to the cohesive energy of atomic bonds) may be observed. Given the expected responses, nanoindentation is identified as an ideal experimental method to

probe local material response and slip-boundary interactions in the presence of hydrogen, as it has been used to investigate small-volume material behavior in a variety of materials, including Ni and other alloys cathodically charged *in-situ*.[169–171] Thus, bulk and shear modulus are calculated from elastic modulus measured with nanoindentation as a function of crystallographic orientation for a small volume of a polycrystalline metal sample. Additionally, dislocation nucleation and motion as a function of orientation and charging condition are probed by analyzing the load-depth response during an instrumented indentation test.

8.2 Experimental Procedures

Experiments were conducted on Ni-201, a commercially pure nickel alloy supplied by ATI Allegheny Ludlum, with impurities (in wt.%) of 0.01 C, 0.01 Mn, < 0.01 Fe, 0.05 Si, < 0.01 Cu, and < 0.001 S. An alloy with an ultralow sulfur concentration was chosen for this investigation in order to mitigate sulfur segregation effects, which can be pronounced in Ni.[162] The as-received Ni-201 plate was annealed at 900^{o}C for 1 hr to encourage grain growth. Three small specimens were then cut from the annealed plate. Samples 1 and 2 were prepared by grinding through 1200 grit SiC papers, polishing through 1 μm diamond polish, followed by a final polish with 0.02 μm colloidal silica suspension, while sample 3, prepared later, was ground through 1200 grit SiC papers, polished through 1 μm diamond polish, and finally vibropolished with 0.02 μm colloidal silica. Microstructure was characterized using electron backscatter diffraction (EBSD) orientation mapping conducted with a Phillips XL-40 field emission scanning electron microscope at 30 kV. Grain orientations were determined using TSL OIM data collection

and analysis software; grains with near-(001), (101), and (111) orientations were selected for investigation from samples 1 and 2, while grains with intermediate orientations were located in sample 3. Figure 8.1 shows sample grain boundary misorientation maps obtained via a Hough-based EBSD analysis of large area (~1.5 mm x 2 mm) scans utilizing 4 x 4 detector binning and a hexagonal grid with a step size of 10 μm. Nanoindentation measurements to determine mechanical properties were performed using a Nanoindenter XP equipped with a nominally 150 nm radius Berkovich probe. Stiffness, modulus, and hardness values were obtained through dynamic indentation using the continuous stiffness module (CSM) at a frequency target of 20 Hz, displacement target of 1 nm, and a 1500 nm depth limit. Indents were arranged in 7 x 7 arrays with a 25 μm spacing, ensuring no indent was affected by the plastic zone of a previous indent.

Atomic hydrogen was dissolved into the three specimens, as well as two additional specimens for LECO analysis, by thermally charging in high-pressure hydrogen gas. The specimens were inserted into a thick-walled stainless steel (A-286) pressure vessel and then placed in a furnace. Residual gases were removed from the sealed pressure vessel and gas-handling manifold using a purging and evacuating sequence. Three purge/evacuation cycles were conducted with helium, followed by three cycles with hydrogen. Once the purging/evacuation cycles were completed, the pressure vessel was heated and filled with 99.9999% hydrogen gas. Charging was conducted at elevated temperature to enhance hydrogen diffusion, thereby minimizing charging times, but temperatures were limited to avoid thermally activated microstructural changes in the nickel. Based on previous work[172] a charging cycle was selected to achieve a hydrogen concentration of ~2000appm. Samples were charged at a hydrogen gas pressure of 82

MPa and a temperature of 200°C for 280 hrs. Hydrogen-charged specimens were stored at subfreezing temperature until indentation could be performed, and samples for LECO hydrogen analysis were transported in dry ice, to minimize hydrogen loss. Indentation was again performed in the selected grains with the method described previously.

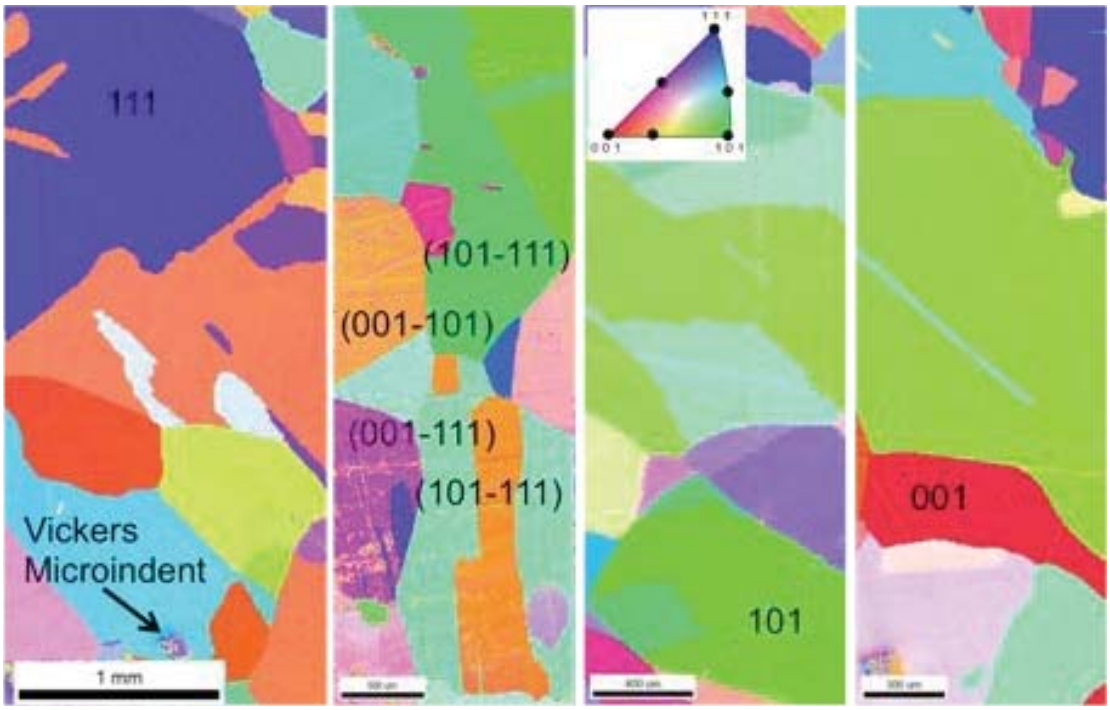

Figure 8.1 Inverse pole figure maps indicating grain orientations. Grains selected for indentation have been labeled with their approximated orientations. Their locations have been marked on the inset stereographic triangle.

8.3 Results

LECO analysis determined the average bulk hydrogen concentration in the samples to be 16.06 at. % (2000 appm). Due to hydrogen egress a concentration gradient will develop between the surface and the bulk, thus the relatively shallow depths probed by nanoindentation will have a concentration less than the bulk. Previous calculations have estimated that the hydrogen content will decrease to approximately half the bulk

concentration at ~13 μm from the surface. Though it is difficult to determine the hydrogen concentration in the volume beneath each indent, all indents detected appreciable changes in mechanical properties in the hydrogen-charged condition, thus it is reasonable to assume dissolved hydrogen impacts material properties.

Dynamic nanoindentation was performed by the CSM technique. Table 8.1 summarizes the average elastic modulus and hardness values before and after hydrogen charging. Elastic modulus shows a pronounced decrease in the presence of hydrogen, on the order of 22%, while indentation hardness appears to be relatively insensitive to hydrogen. In order to avoid surface asperity and tip imperfection affects, modulus and hardness values were tabulated in a range where the plot of the ratio of load over stiffness squared, P/S^2, vs. indentation depth, d, was approximately constant; an example is shown in Figure 8.2. Oliver and Pharr[7] suggested this procedure as a calibration on fused silica to remove load frame compliance effects working from the proposal that at depths greater than a few hundred nanometers, where hardness and modulus should be independent of

Table 8.1 Hardness, H, and elastic modulus, E, of Ni-201 samples before and after hydrogen charging as a function of crystallographic orientation. Theoretical indentation modulus, M, is included for comparison with measured values prior to charging. Modulus decreases after hydrogen charging, while hardness, which decreases only slightly, is relatively insensitive to hydrogen content. Values are averaged for more than 35 indents per grain. Measured elastic modulus values differ from theoretical values by about 3%.

Orientation	Theoretical Modulus (GPa)	Modulus (GPa)		Hardness (GPa)	
	Calculated	*Before H*	*H-charged*	*Before H*	*H-charged*
001	194	202±7	155±12	2±0.2	2±0.2
101	215	209±6	171±15	2±0.1	2±0.2
111	222	224±7	180±33	2±0.2	2±0.9
001-111		221±17	179±19	3±0.5	2±0.3
001-101		228±16	177±21	3±0.2	2±0.3
101-111		224±12	190±24	3±0.3	2±0.3
101-111		218±21	189±18	3±0.4	2±0.2

depth, P/S^2 should also be constant according to:

$$\frac{P}{S^2} = \frac{\pi}{(2\beta)^2}\frac{H}{E^2}. \quad \text{Equation 8.1}$$

In Eq. (1) H is the sample hardness, E is the elastic modulus, and β is a constant which has traditionally been used to account for stiffness deviations resulting from axial asymmetries of pyramidal indenters, and is generally taken as 1.034 for Berkovich indenters. This procedure reveals that data taken at shallow depths should be ignored due to measured hardness variation resulting from tip imperfections. At large indentation depths, geometrical similarity of the pyramidal indenter as well as homogenous "bulk-like" properties of the sample ensure that the mean pressure or calculated hardness remains essentially constant with depth. In general, P/S^2 data became constant at indentation depths greater than ~200 nm, thus only hardness and modulus values collected for indent depths greater than 200 nm were analyzed.

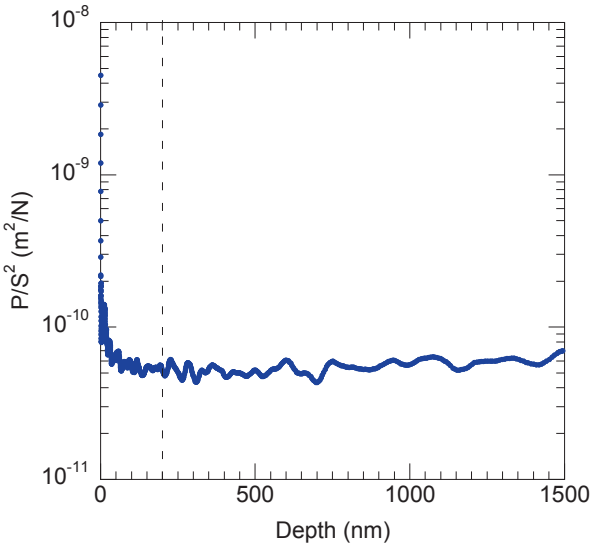

Figure 8.2 Plot of P/S^2 as a function of indentation depth. Data below 200 nm (marked with dashed line) were not analyzed for average mechanical properties.

Additionally, because these indentation experiments were performed within individual grains of a cubic crystal, the elastic properties will be highly anisotropic. Traditional indentation contact mechanics analyses were developed for isotropic materials, thus it is important to correct for the anisotropy of measured properties. Vlassak and Nix[173] have shown that the indentation modulus can be calculated for arbitrary anisotropic solids. They calculated the contact stiffness for a flat triangular punch and a half space for various anisotropic materials. Their formulae are employed here to derive theoretical indentation moduli for specific grain orientations and indenter geometries; these theoretical values are compared to experimentally measured moduli to verify that the measured values are reasonable. Indentation modulus, *M,* for a solid with cubic crystal symmetry is calculated from:

$$M = 1.058\,\beta_{hkl}\left(\frac{E}{1-\nu^2}\right)_{isotropic}, \qquad \text{Equation 8.2}$$

where the pre-factor 1.058 is a stiffness adjustment for tips with a triangular geometry, E is the elastic modulus, and β_{hkl} is a correction factor calculated by:

$$\beta_{hkl} = a + c(A - A_o)^B. \qquad \text{Equation 8.3}$$

In the above formula, A is the anisotropy factor, and a, c, B, are constants determined from the Poisson's ratio in the cube directions. M has been calculated for each of the cube directions in Ni using tabulated values for elastic modulus,[17] and are compared with modulus values measured for uncharged grains in Table 8.1. Measured elastic modulus values differ from the theoretical value by about 3%, indicating that: (1) comparing measured modulus values will provide an accurate assessment of property changes as a

function of hydrogen charging, and that (2) it is reasonable to use the measured elastic modulus values to calculate the bulk and shear modulus of Ni for further analysis.

The observed decrease in modulus with no corresponding increase in hardness indicates that hydrogen may adversely affect the strength of atomic bonds in this material (quantified by comparing bulk modulus) while also impacting the motion of dislocations causing plastic deformation (compared by evaluating shear modulus), before and after hydrogen exposure. Based on the relationship between elastic modulus, E, and Poisson's ratio, υ, the bulk modulus, B, was calculated with:

$$B = \frac{E}{3(1-2\upsilon)}, \qquad \text{Equation 8.4}$$

while the shear modulus, G, of each indented grain was calculated using:

$$G = \frac{E}{2(1+\upsilon)}. \qquad \text{Equation 8.5}$$

Calculated bulk and shear modulus values are tabulated as function of orientation before and after hydrogen charging in Table 8.2. As with measured elastic modulus, calculated bulk and shear modulus tend to decrease by approximately 22% in the presence of hydrogen. The dramatic change in mechanical properties in the presence of hydrogen can be identified in the disparity in unloading slopes of two representative load-depth curves, shown in Figure 8.3.

Table 8.2 Bulk modulus, B, shear modulus, G, calculated from elastic moduli in Table 8.1, as well as interatomic spacing, r_0, and number of pop-ins, as a function of charging condition. Shear modulus decreases, while interatomic spacing correspondingly increases when Ni-201 is hydrogen charged. Additional pop-in events are required to achieve full plasticity in the presence of hydrogen.

Orientation	B (GPa)		G (GPa)		R_0 (GPa)		No. of Pop-ins	
	Before H	*H-charged*	*Before H*	*H-charged*	*Before H*	*H-charged*	*Before H*	*H-charged*
001	168.8	129.6	132.3	101.8	0.0099	0.0128	17	18
101	174.2	142.6	136.9	112.1	0.0096	0.0116	17	18
111	186.3	149.8	146.7	117.7	0.0089	0.0111	15	18
001-111	183.8	149.8	177.5	117.7	0.0091	0.0111	11	14
001-101	190.7	147.6	149.9	116.0	0.0087	0.0113	11	15
101-111	186.7	158.8	153.9	124.8	0.0085	0.0105	10	14
101-111	181.1	157.8	142.3	123.9	0.0092	0.0106	11	17

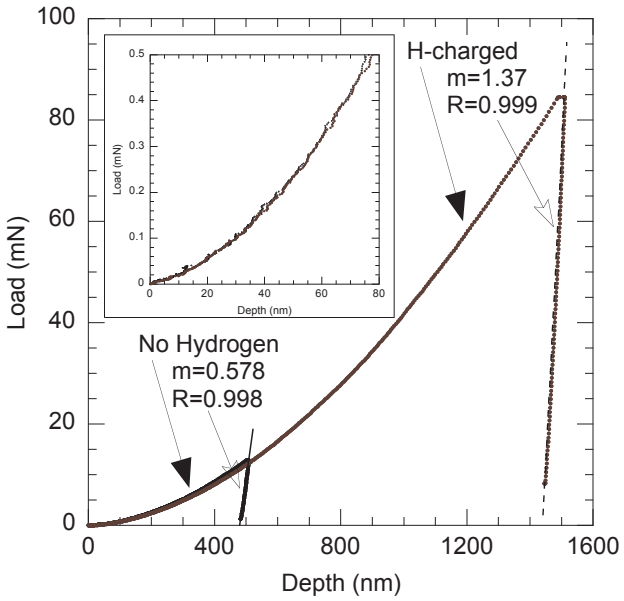

Figure 8.3 Representative load-depth curves generated to evaluate unloading slopes with respect to hydrogen content. The slopes have been labeled for each curve, the unloading slope changes when the microstructure is saturated with hydrogen, indicating that a clear difference in mechanical properties should be observed. Additionally, the loading slope varies little between conditions indicating hardness varies only slightly with hydrogen charging, and always decreases.

8.4 Discussion

8.4.1 Correlation of Bulk Modulus and Cohesive Energy

The cohesive energy and bulk modulus are important quantities in determining the stability of atomic structures under various conditions. Cohesive energy, in physical terms, is the "energy that must be added to the crystal to separate its components into neutral free atoms at rest, at infinite separation, with the same electronic configuration".[174] In terms of metallic crystal structure, the cohesive energy indicates the force required to separate a crystal along atomic planes, interfaces, or grain boundaries. Realizing that most plastic failures occur by shearing atomic planes, and resistance of a material to imposed stresses arises from the strength of interatomic bonds, comparison of the bulk modulus provides a method for linking macroscale behavior with microscale phenomena.

Previous studies[175,176] have attempted to relate cohesive energy to the bulk modulus (inverse of compressibility) of materials with multiple crystal structures and bond types, but a more direct correlation was found by comparing the cohesive energy density (energy per atomic volume) with the bulk modulus.[177] Changes in bulk modulus, resulting in variations in interatomic bond length should alter the energy of the interactions (i.e. cohesion) as well as the volume of material experiencing a force. This should consequently affect the cohesive energy density. Indeed, a plot of the bulk modulus versus cohesive energy density of face centered cubic (FCC) transition metals results in a linear relationship with a correlation factor 0.93, as shown in Figure 8.4, which was adapted from the work of Wacke et al.[177] Thus comparing the bulk modulus of Ni-201 (a group VIII B metal) in an uncharged and hydrogen charged condition appears

to provide a valid method for determining the effect of hydrogen on the cohesive energy in Ni.

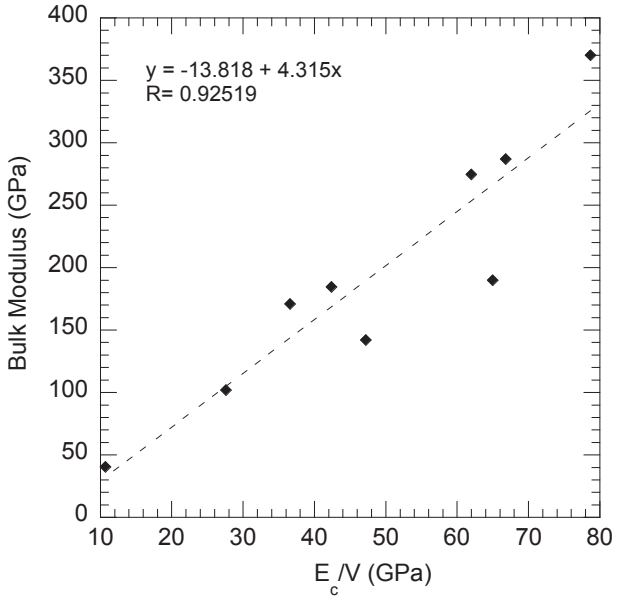

Figure 8.4 Linear relationship between bulk modulus and the cohesive energy density indicates that comparing bulk modulus is a method for evaluating the effect of solute hydrogen on the cohesive energy between atomic planes. Adapted from Wacke, S., Górecki, T., Górecki, C. & Książek, K. Relations between the cohesive energy, atomic volume, bulk modulus and sound velocity in metals. *J. Phys. Conf. Ser.* **289,** 012020 (2011).

In order to compare the effect of hydrogen on atomic bonding more directly, we can integrate the measured elastic modulus and the potential well concept thereby estimating the equilibrium interatomic spacing as a function of hydrogen charging. A typical interatomic potential function has the form:

$$V(r) = \frac{A}{r} + \frac{B}{r^9}, \qquad \text{Equation 8.6}$$

where *V(r)* is the potential as a function of interatomic spacing, *A* and *B* are constants, and *r* is the interatomic spacing. Taking the derivative of the this function yields a force as a function of interatomic spacing, *F(r)*:

$$F(r) = -\frac{dV}{dr} = -\frac{A}{r^2} + \frac{9B}{r^{10}}. \quad \text{Equation 8.7}$$

Realizing that at spacings very close to the equilibrium interatomic spacing, r_0, the curve looks like a straight line, the slope can be determined by taking the derivative of the force function, yielding the following:

$$dF = -\left(\frac{8A}{r_0^3}\right) dr = -k \cdot dr, \quad \text{Equation 8.8}$$

where *k* is the "spring" constant, as in Hooke's Law. This equation indicates, as does Hooke's Law, that in the vicinity of r_0 there is a restoring force that is proportional to the distance from r_0, and the spring constant can be determined from the interatomic potential. Since the interatomic force has been modeled as a spring, there must be a relationship between *k* and the elastic modulus. Applying the definitions of stress and strain to Equation 8.8 we obtain the relationship:

$$dF = -\left(\frac{\sigma}{\varepsilon}\right) r_0 dr = -E r_0 dr, \text{ Equation 8.9}$$

where σ is stress, *e* is strain, and the ratio σ/e is equivalent to the elastic modulus, *E*. By this relationship, elastic modulus is equivalent to the microscopic "spring" constant, thus elastic modulus is directly proportional to the attractive potential and varies inversely with interatomic spacing. Combining Equation 8.8 and Equation 8.9, we find that

$E = {}^{8A}/_{r_0^4}$. Therefore, using the elastic modulus values measured via nanoindentation, the interatomic spacing can be estimated and the relative change as a function of hydrogen charging can be evaluated. Interatomic spacing values, in terms of the constant *A*, are collected in Table 8.2. On average, the interatomic spacing increases by 20-25% when the lattice is saturated with hydrogen. This corresponds with an average 20-25% decrease in bulk modulus in a hydrogen-charged lattice.

The decrease in the measured elastic modulus and calculated bulk and shear moduli agrees with studies conducted on thermally charged 21-6-9 stainless steel by Nibur et al.,[178] which detected a 21% decrease in elastic modulus measured by nanoindentation, as well as with a study by Barnoush and Vehoff[169] reporting a 28% decrease in the shear modulus of Ni that was cathodically charged *in-situ* and indented. The authors of the latter paper attribute the decrease in shear modulus to a hydrogen-induced reduction in cohesive energy. Other published data have detected smaller hydrogen-induced reductions in elastic modulus[179,180] and shear modulus.[180]

Conversely, the measured hardness of Ni-201 does not change appreciably with the addition of hydrogen to the lattice. This is in contrast with other indentation studies, which noted increases in hardness of nearly 30%.[178] A constant hardness suggests that there is no macroscopic increase in flow stress associated with hydrogen charging. However, many studies have suggested that hydrogen solute atoms will affect dislocation mobility and velocity, causing plasticity at lower loads than when the microstructure is free from hydrogen. In order to evaluate the impact of hydrogen solute atmospheres on

dislocation motion, in the absence of an appreciable hardness variation, the onset of plasticity as observed through nanoindentation load-depth curves is analyzed.

8.4.2 Impact on Elastic-Plastic Transition

Closer examination of the initial loading portion of the load-depth curves typified by Figure 8.3 reveals "staircase" yielding proceeding from the initial yield point, or pop-in, to the final load at which full plasticity around the indentation is attained. Various studies[31,181] have indicated that the dislocation density in a well-annealed and electropolished sample is so low that surface dislocations are spaced on the order of 1-10 μm apart, thus it is likely that an indentation test will probe a dislocation-free volume. In this case, the material will load elastically until a stress approaching the theoretical shear strength is reached. This stress is usually on the order of *G/10-G/50*, where *G* is the shear modulus; thus the stress required to nucleate dislocations tracks with the shear modulus of the material.[182] When this stress is attained, a dislocation is nucleated and will develop into a Frank-Read source, resulting in dislocation multiplication. Rapid multiplication of dislocations allows the indenter tip to move deeper into the surface without a corresponding load increase, which is recorded as a depth excursion, or pop-in. Thus, analyzing the observed step-wise yielding reveals information about the effect of hydrogen on plasticity in Ni and relates to the observed decrease in modulus in the presence of hydrogen.

With a stacking fault energy of ~128 kJ/mol,[183] plasticity in Ni is characterized by the ability to cross-slip when the primary system is not oriented for easy glide. Assuming the initial excursion is attributed to a single Frank-Read source, all dislocations emitted

from this source will have the same slip system. However, due to the hemispherical stress field under the indenter tip, additional material displacement will need to be accommodated, requiring either cross-slip to a secondary system or additional dislocation nucleation. Multiple excursions during the staircase yielding phenomena indicate that additional dislocation nucleation is at least partially responsible for this accommodation. As shown in Table 8.2, additional excursions are detected during staircase yielding in the presence of hydrogen. It has been suggested that hydrogen may stabilize the edge component of mixed dislocations, thereby limiting cross-slip,[184] and necessitating additional dislocation nucleation or source activation in order to accommodate deformation. The observation of multiple additional excursions during yielding in H-charged Ni support the proposal that H may inhibit dislocation cross-slip, requiring deformation to proceed by successive dislocation nucleation events.

Additionally, there is a clear orientation dependence on the increase in detected excursions in H-charged Ni-201. Grains oriented in (001) and (101)-type directions require fewer additional excursions to achieve plasticity than those oriented towards (111). This dependence may be explained by the preferred slip systems in Ni; the "soft" orientations, those near (101) are least likely to exhibit slip on a secondary system because the resolved shear stress in these orientations is low. Alternatively, "hard" orientations such as (111) lie in a region of the stereographic triangle where multiple slip systems have the same resolved shear stress and will tend to operate,[185] thus it seems reasonable that fewer nucleation events will take place in the (111) oriented grain prior to plasticity as cross-slip may be favorable. However, when hydrogen is dissolved in the lattice a greater number of excursion events are observed in the 'hard' orientations

suggesting that hydrogen may indeed limit cross-slip, requiring additional nucleation and activation events to accommodate material deformation.

Furthermore, because dislocation nucleation is a shear-biased event,[29,30] the stress required for incipient plasticity lends insight into the mechanism responsible for mechanical behavior changes. The maximum shear stress beneath the indenter tip during elastic loading is described by:[18]

$$\tau_{max} = 0.31\left(\frac{6PE^*}{\pi^3 R^2}\right)^{1/3}, \qquad \text{Equation 8.10}$$

where P is the indentation load at pop-in, R is the instantaneous radius of the indenter tip at the moment of pop-in, calculated as:

$$R = \frac{9P^2}{\delta^3 16E^{*2}}. \qquad \text{Equation 8.11}$$

Again, P is the indentation load, δ is the depth of the indenter contact at the moment of pop-in, and E^*, in both Equation 8.10 and Equation 8.11, is the reduced modulus of the material which accounts for tip compliance. E^* is calculated from:

$$\frac{1}{E^*} = \frac{(1-\nu^2)}{E} + \frac{(1-\nu_i^2)}{E_i}, \qquad \text{Equation 8.12}$$

where the subscript i refers to the indenter. Figure 8.5 presents a cumulative fraction of events plot of maximum shear stress for the orientations corresponding to the vertices of the stereographic triangle. The intermediate orientations will follow similar trends. The maximum shear stress required for incipient plasticity decreases when the microstructure is saturated with hydrogen, though maximum shear stress does not appear to be a

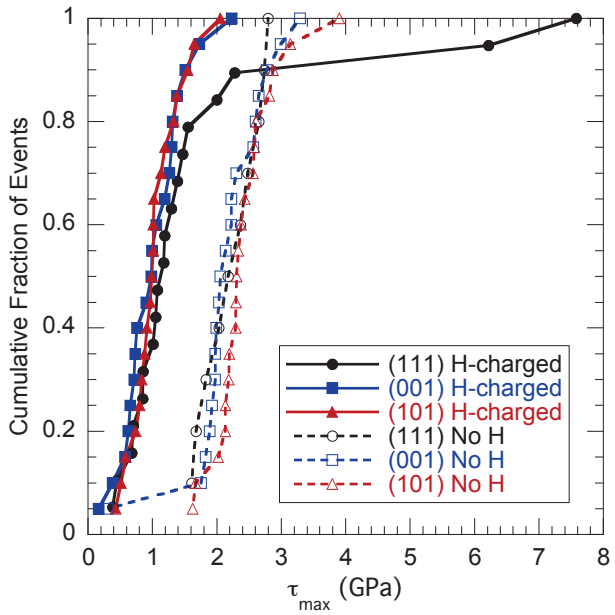

Figure 8.5 Maximum shear stress beneath the indenter tip, calculated using the load and depth at the onset of plasticity, i.e. the first excursion. τ_{max} for all orientations decreases when the material is hydrogen charged.

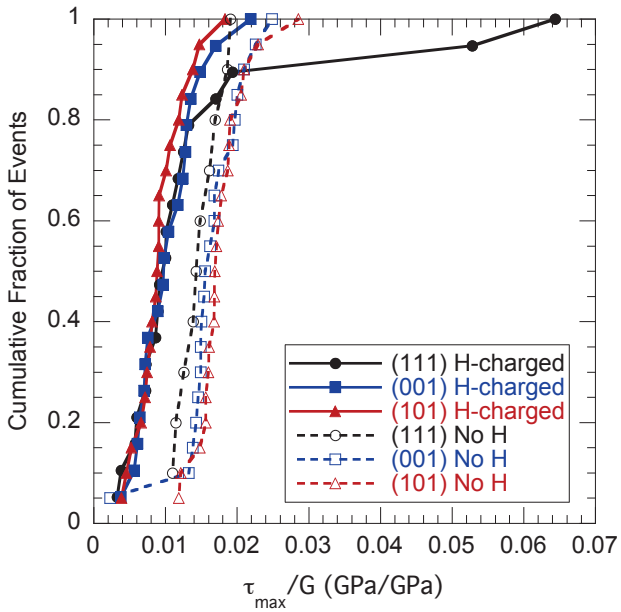

Figure 8.6. Stress required for initiating dislocation motion, in terms of shear modulus, as a function of charging condition and orientation. The minimum stress varies only slightly with the addition of hydrogen, while the overall trends and maximum stresses vary widely between uncharged and hydrogen-charged material, but minimally between orientations.

function of orientation. These values are related to the calculated shear moduli as τ_{max}/G, plotted in Figure 8.6, revealing that the stress required for initial dislocation nucleation decreases for hydrogen charged material. This is in agreement with computational results,[186] which showed that the first excursion load is significantly lower when Ni is charged with 1 at. % H, and with other experimental results that indicate hydrogen enhances dislocation nucleation.[170,187] In the current study, the minimum stress required to initiate dislocation plasticity is nearly insensitive to crystallographic orientation. The calculated τ_{max}/G values are lower than what we might expect (G/30) suggesting that the defect density is large enough that a defect is always sampled and is a source of nucleation behavior, thus it dominates over orientation dependence. Furthermore, the range of shear stresses observed experimentally at the onset of plasticity indicate that dislocation nucleation may initiate at a local defect site, specifically a solute H atom or a H-induced vacancy, rather than in a totally defect free volume. Thus, solute hydrogen may play a dual role in embrittling kinetics: reducing the cohesive energy of the material and also serving as a local site for the additional dislocation nucleation events required for material deformation.

8.5 Summary and Conclusions

Nanoindentation and electron backscatter diffraction were employed to investigate the orientation dependent effects of hydrogen on the mechanical behavior and onset of plasticity in ultra-low sulfur Ni-201. Evaluating changes in bulk modulus, shear modulus, and yield behavior led to three main conclusions.

1. The measured elastic modulus, and subsequently calculated bulk modulus and shear modulus, decrease approximately 22% when Ni-201 is thermally charged

with hydrogen. The sharp reduction of bulk modulus is correlated with a decrease in the cohesive energy between atomic bonds, which supports a macroscopic grain boundary decohesion failure mechanism. There is a pronounced orientation effect, owing to the anisotropy of polycrystalline Ni. As expected the modulus is highest in (111)-type grains, and lowest in (001)-type grains.

2. Ni-201 deforms by a staircase yielding mechanism, that is, multiple depth excursions are required to achieve plasticity, in both the uncharged and hydrogen charged conditions. When the microstructure is saturated with hydrogen, additional excursion events are observed prior to general plasticity. This suggests that additional dislocation nucleation events are required to accommodate the deformation induced by indentation before the material deforms irreversibly, which may be linked to a restriction of cross-slip. Again, an orientation effect is resolved. Hard orientations require the activation of a greater number of extra slip systems prior to plasticity than soft orientations.
3. Hydrogen charged Ni-201 yields at lower maximum shear stresses (applied loads) than the uncharged material. However, the calculated maximum shear stress does not vary with crystallographic orientation. The stress required for initial dislocation nucleation has only a small variation as a function of hydrogen content, when compared in terms of the calculated shear moduli, suggesting that the reduction in cohesive energy is the primary driving force for decreasing the energy barrier to initiate plasticity.

This investigation indicates solute hydrogen may play a dual role in local embrittling kinetics in Ni: hydrogen effectively reduces the cohesive force between atomic planes

and interfaces, manifested as a decrease in measured elastic modulus and calculated bulk modulus, while also serving as a local site for the additional dislocation nucleation events required to accommodate deformation when dislocation cross-slip may be restricted.

CHAPTER 9. GRAIN BOUNDARY CONTRIBUTIONS TO HYDROGEN-AFFECTED PLASTICITY IN NICKEL-201

Previously published by Journal of Materials*, Volume 66, pages 1383-1389, in August 2014.*

9.1 Introduction

Degradation of metallic systems exposed to hydrogen, especially those used in pressure vessels, tanks, and pipelines can lead to unexpected catastrophic failures. Hydrogen has been linked to a decrease in ductility, fracture strength, and fracture toughness in many metals, i.e., the well-known phenomenon of hydrogen embrittlement, and has resulted in loss of life in engineering failures in the energy industry. Thus, understanding the microscopic mechanisms that ultimately lead to macroscale failures is an important step in mitigating hydrogen embrittlement, thereby enabling effective transport and storage of hydrogen. The two microscale mechanisms commonly associated with hydrogen degradation of Ni are decohesion, where hydrogen at interfaces lowers cohesive strength, and hydrogen-enhanced localized plasticity, where hydrogen impacts local instabilities associated with plastic flow.[188]

Hydrogen embrittlement of many structural materials, such as high strength steels and nickel-based alloys, is characterized by decohesion on grain boundaries or interfaces, resulting in low-toughness intergranular fracture in materials that would normally fail in a ductile manner; embrittlement occurs without significant macroscopic plastic

Deformation.[152–155,189] As a result, solute hydrogen is thought to decrease the cohesive force, and corresponding surface formation energy, required to separate atomic bonds along a crystallographic plane, grain boundary, or particle/matrix interface. This postulate, called the hydrogen enhanced decohesion (HEDE) mechanism suggests that dislocation motion is limited to maintain atomically sharp crack tips (though dislocation motion may work to increase stress at decohesion sites by strain gradient hardening [156,158] or similar processes). Direct experimental evidence for HEDE is difficult to attain due to technique limitations for observing atomic-scale events in bulk material. However, high hydrogen concentrations have been measured at critical locations, such as grain boundaries and particle-matrix interfaces [160,161] resulting in increased intergranular fracture in some systems[162,163]. Easier field-evaporation of surface atoms during field-ion microscopy of Fe using hydrogen as an imaging gas has also been reported suggesting hydrogen may weaken interatomic bonds [164], thereby reducing cohesive strength. Furthermore, atomistic models suggest that interatomic bond strength may be weakened by the presence of hydrogen between atomic planes in Al[165] and that solute hydrogen leads to reduction of fracture toughness in high-strength alloys[166].

In contrast to high-strength materials that suffer microscopically brittle fracture mechanisms associated with HEDE, lower-strength materials may exhibit hydrogen-enhanced localized plasticity (HELP).[151] This mechanism suggests that failure in the presence of hydrogen proceeds by locally ductile processes and that hydrogen enhances rather than retards the motion of dislocations. For example, hydrogen atoms forming Cottrell atmospheres along a dislocation core interact with the elastic stress fields of neighboring dislocations, reducing the repulsion between neighboring dislocations[190] and

easing motion. Often, solute Cottrell atmospheres of interstitial atoms causes dislocation drag, retarding plastic flow.[191] But the mobility of interstitial hydrogen is high enough to travel with dislocations, resulting in a stress-shielding effect.

Theoretical consideration of the role of hydrogen on local dislocation motion,[192] as well as experimental observations over a range of strain rates and temperatures,[193] suggest that hydrogen in solid solution decreases barriers to dislocation motion, which in turn, localizes deformation near the fracture surface.[194,195] In essence, macroscopic ductility is limited by the onset of highly localized plasticity resulting in apparent embrittlement. High resolution fractography of embrittled Fe and Ni show extensive plastic deformation adjacent to fracture surfaces;[61] additional in-situ environmental cell deformation and fracture of various metals and intermetallics demonstrated similar localized plasticity.[197,198]

The objective of this study is to evaluate potential roles for both HEDE and HELP to contribute to hydrogen-induced intergranular fracture, focusing on Ni-201 as a model system. Mechanical property and fractographic investigations suggest that grain boundary character may have a prominent role in intergranular hydrogen embrittlement;[172] special low-energy boundaries have been shown to reduce the degree of intergranular fracture of hydrogen charged Ni specimens. Accordingly, commercially pure Ni-201 is chosen for the current investigation primarily because it is susceptible to hydrogen-induced intergranular fracture. While decohesion is identified as the primary mechanism causing intergranular fracture, hydrogen-affected plasticity is thought to contribute to the process.[199] Furthermore, Ni-201 is a representative system for important engineering alloys such as nickel-based superalloys and austenitic stainless steels. In addition, its

stacking fault energy is sufficiently high so as to allow dislocation cross-slip when uncharged, enabling the monitoring of specific dislocation processes. According to the HELP theory, a dislocation with both edge and screw components must convert to screw configuration locally in order to cross-slip, which requires a redistribution of hydrogen around the edge segment, which preferentially attracts hydrogen. But, in the absence of a driving force for hydrogen redistribution, dislocations are confined to the original slip plane and cross-slip is restricted.[200] Nanoindentation has been used to investigate dislocation processes in many materials, including hydrogen charged alloys,[170,171,201–203] and thus is selected as an ideal method to analyze the interaction between grain boundary misorientation and plastic deformation in hydrogen-charged and as-annealed Ni-201.

9.2 Experimental Procedure

Experiments were conducted on Ni-201, a commercially pure nickel alloy supplied by ATI Allegheny Ludlum, with impurities (in wt.%) of 0.01 C, 0.01 Mn, < 0.01 Fe, 0.05 Si, < 0.01 Cu, and < 0.001 S. Grain boundary segregation, especially of S in Ni,[162] has been shown to dramatically alter hydrogen effects on dislocation-grain boundary interactions in commercially pure materials;[204] to mitigate this issue, an alloy grade with an ultralow sulfur concentration was chosen for this investigation. The as-received Ni-201 plate was annealed at 900^{o}C for 1 hr to stimulate grain growth. Two small specimens were then cut from the annealed plate. Samples were prepared by grinding through 1200 grit SiC papers, polishing through 1 μm diamond polish, followed by a final polish with 0.02 μm colloidal silica suspension.

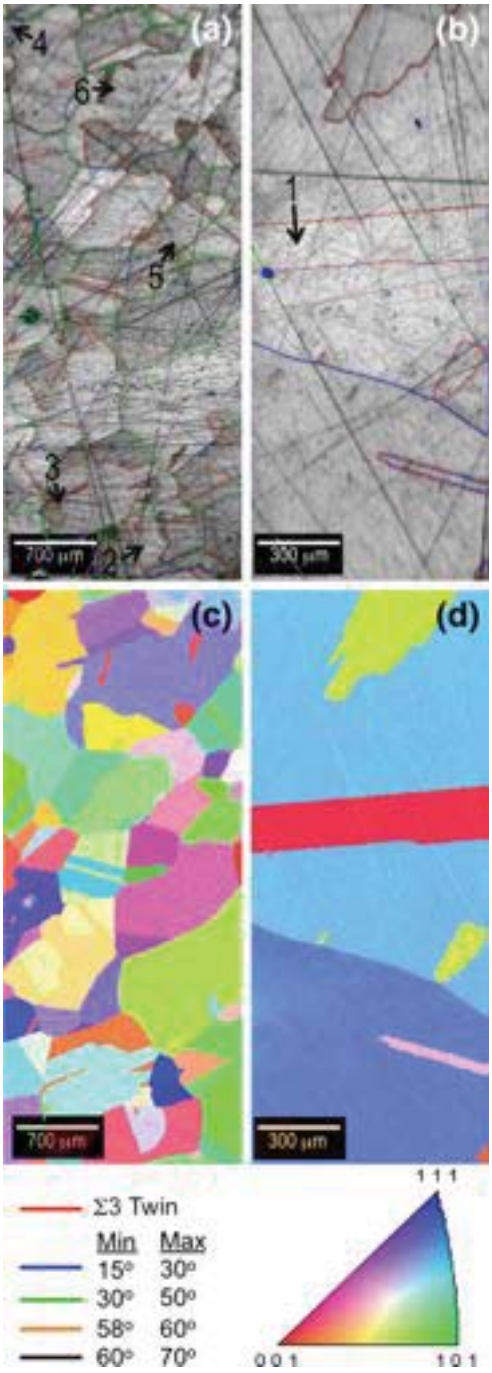

Figure 9.1 Grain boundary maps (a-b) with boundaries investigated for slip transmission behavior labeled. Arrows indicate direction of slip transmission across boundary. Boundaries 1-3 are Σ3 recrystallization twin boundaries, boundary 4 is a random boundary with a misorientation of ~48°, boundaries 5-6 are random boundaries with misorientations of 58° and 59°, respectively. Inverse pole figure maps (c-d) show grain orientations.

The microstructure was characterized using electron backscatter diffraction (EBSD) orientation mapping conducted with a Phillips XL-40 field emission scanning electron microscope at 30 kV. Grain boundaries with random misorientation (>15^{o}) as well as Σ3 recrystallization twins were identified by TSL OIM data collection and analysis software. Figure 9.1 shows sample grain boundary misorientation maps obtained via a Hough-based EBSD analysis of large area (~1.5 mm x 2 mm) scans utilizing 4 x 4 detector binning and a hexagonal grid with a step size of 10 μm; boundaries chosen for slip transmission investigation are labeled.

A Hysitron Ubi nanoindenter equipped with a 60^{o} 150 nm radius conical indenter tip was used to make indents along the grain boundaries at peak loads of 5000 μN, 7000 μN, and 9000 μN. Representative nanoindentation load-displacement records are shown in Figure 9.2. The indents were imaged using a Bruker Multimode atomic force microscope (AFM) in contact mode. Slip transmission across grain boundaries was investigated and slip steps were identified and measured with image processing software. Atomic hydrogen was dissolved into the three specimens, as well as two additional specimens for hydrogen concentration analysis, by thermally charging in high-pressure hydrogen gas. The specimens were inserted into a thick-walled stainless steel (A-286) pressure vessel and then placed in a furnace. Residual gases were removed from the sealed pressure vessel and gas-handling manifold using a purging and evacuating sequence. Three purge/evacuation cycles were conducted with helium, followed by three cycles with hydrogen. Once the purging/evacuation cycles were completed, the pressure vessel was heated and filled with 99.9999% hydrogen gas. Charging was conducted at elevated temperature to enhance hydrogen diffusion, thereby minimizing charging times,

but temperatures were limited to avoid thermally activated microstructural changes in the nickel. Based on previous work [28] a charging cycle was selected to achieve a hydrogen concentration of ~2000 appm. Samples were charged at a hydrogen gas pressure of 82 MPa and a temperature of 200^{o}C for 280 hrs. Hydrogen-charged specimens were stored at subfreezing temperature until indentation could be performed, and samples for LECO hydrogen analysis were transported in dry ice, to minimize hydrogen loss. Indentation was again performed along the same grain boundaries in Figure 1 for this hydrogen-charged condition using the method described previously.

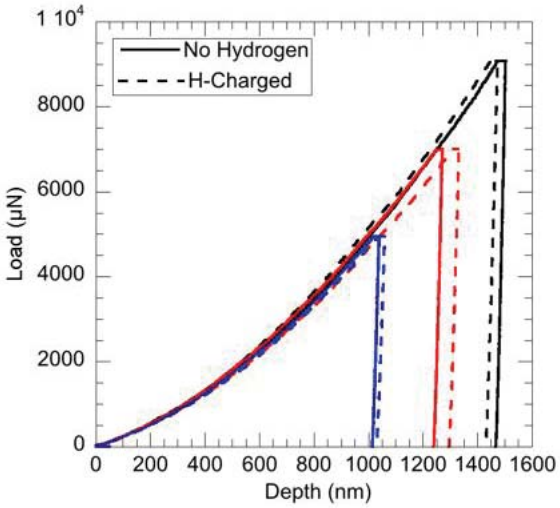

Figure 9.2 Representative load-displacement curves from indents made along a specific grain boundary before and after hydrogen charging. Solid lines correspond to indents made prior to charging, while dashed lines correspond to indents after hydrogen charging.

9.3 Results and Discussion

The average bulk hydrogen concentration in the samples, as determined with an inert gas-fusion instrument, is ~2000 appm (35 ppm by weight). Due to hydrogen egress a concentration gradient will develop between the surface and the bulk; therefore, the

relatively shallow depths probed by nanoindentation will have a concentration less than the bulk. Though it is difficult to determine the hydrogen concentration in the volume beneath each indent or within grain boundaries, AFM analysis of local deformation generated by indentation revealed measurable changes in the hydrogen-charged condition, thus it is reasonable to assume dissolved hydrogen impacts plasticity in Ni.

Hydrogen effects on plasticity can be evaluated by comparing measured hardness as well as material pile-up and emergence of slip steps before and after hydrogen charging. Indentation-induced plastic deformation is often accompanied by the piling up of displaced material around the indent impression. Pile-up of material belies out-of-plane deformation. In a material with high stacking fault energy (SFE_{Ni} ~ 120-130 mJ/m^2)[183] out-of-plane deformation is associated with dislocation cross-slip. When dislocations activated by the applied stress of the indenter emerge on the free surface of the sample they often leave behind slip steps. These slip steps typically form repeatable patterns within the plastic zone of the indent (piled up region) and can be attributed to specific slip planes.[205,206] Evaluating AFM images of indents made at varying loads indicates that, on average, hydrogen increases the spacing between slip steps (Figure 9.3) as well as the total and normalized plastic zone lengths, represented by c and c/a_c, respectively (Table 9.1). The plastic zone length, determined by measuring the extended out-of-plane deformation detected with AFM imaging, is defined in the manner of Samuels and Mulhearn[207] assuming that the plastic zone generated by an indent is hemispherical. In reality the plastic zone has an asymmetric shape,[208] but to first order, the hemispherical approximation is reasonable. The contact radius is determined by

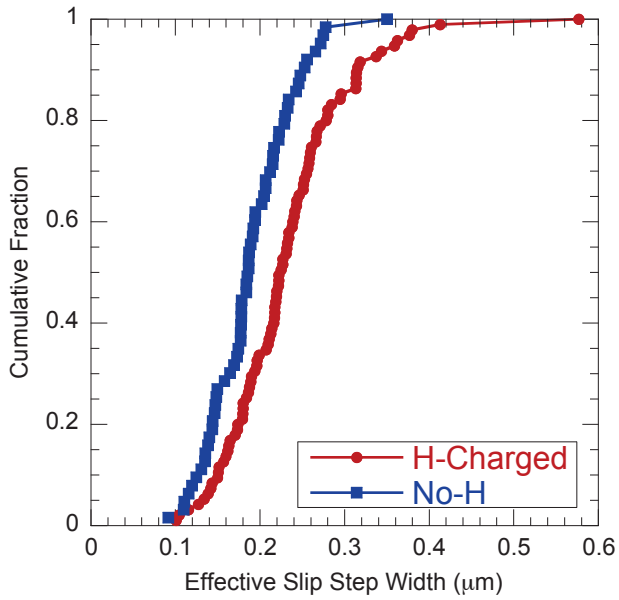

Figure 9.3 Measurements of slip steps resolved with atomic force microscopy images indicates that the average spacing between slip steps on the free surface increases when Ni-201 is hydrogen charged.

measuring the contact area of each indent then calculating radius, a_c, geometrically, assuming an equivalent cono-spherical approximation. The increase in $^{c}/_{a_c}$ is on the order of 20%, well beyond any scatter in the measurements. Normalized plastic zone length is the ratio of measured total plastic zone radius, c, to the measured contact radius, a_c. Conversely, the normalized material pile-up height, $^{h}/_{a_c}$, calculated by dividing measured vertical deformation, h, by measured contact radius, is insensitive to hydrogen charging (Table 9.1). These results suggest that hydrogen enhances dislocation motion but restricts cross-slip, resulting in a larger radius plastic zone for a given contact radius of indenter. Restricted cross-slip would limit the number of dislocations emerging at the free surface, manifested as an increase in distance between slip steps visible on the surface of the sample around the indentation impression. Additionally, hardness, H, as calculated with the calibrated tip area function and as determined by dividing the

maximum applied load, P, by the measured contact radius of the impression, P/a_c, does not change drastically when the material is hydrogen charged. This suggests that the increasing plastic zone radius accommodates additional dislocation motion, thereby allowing the HELP mechanism to proceed without a noticeable change in the hardness that would be calculated using traditional measurement methods.

Table 9.1 Normalized pile-up height (h/a_c), total plastic zone length (c), and normalized plastic zone length (c/a_c) measured from AFM images before and after hydrogen charging. Hardness values output from nanoindenter software ($H_{indenter}$) and hardness calculated from the maximum applied load divided by contact radius (P/a_c) compared as a function of charging condition. Pile-up height is insensitive to dissolved hydrogen, while plastic zone length increases after charging. Hardness also varies slightly when the microstructure is saturated with hydrogen. All values are averages across multiple grain orientation.

Load (μN)	$\mathbf{h}/\mathbf{a_c}$ (nm/nm)		c (μm)		$\mathbf{c}/\mathbf{a_c}$ (μm/μm)		$H_{indenter}$ (GPa)		$\mathbf{P}/\mathbf{a_c}$ (GPa)	
	Before H	*H-charged*	*Before H*	*H-charged*	*Before H*	*H-charged*	*Before H*	*H-charged*	*Before H*	*H-charged*
5000	0.10	0.12	1.74	1.96	2.37	2.70	2.49	2.53	2.91	3.10
7000	0.09	0.09	2.01	2.21	2.52	2.81	2.61	2.58	2.89	3.13
9000	0.08	0.09	2.34	2.70	2.57	2.92	2.69	2.68	3.00	3.17

Furthermore, the susceptibility of various grain boundaries to hydrogen embrittlement may provide a means for reducing intergranular fracture in hydrogen-saturated microstructures. Bechtle et al.[172] have shown that the degree of intergranular fracture of hydrogen charged Ni-201 can be greatly reduced by increasing the fraction of special boundaries, such as Σ3 boundaries, present in the microstructure. In the current investigation, plastic deformation adjacent to different grain boundaries was induced using nanoindentation and slip transmission was observed using AFM. Some clarification of the term “slip transmission” is required. While for some low angle grain boundaries,

dislocations may, in fact, transmit across the boundary, for high angle grain boundaries a pile up and nucleation process is more likely.[209–213] Dislocations will pile up against the grain boundary producing a back stress, when the stress has reached a critical value, a new dislocation can be nucleated from the grain boundary into an adjacent grain. For the special and unique case of Σ3 boundaries (boundaries 1-3), indentations approximately equidistant from the boundary show that if transmission is prohibited in the uncharged condition, it remains prohibited when the material is charged. An example of this situation is shown in Figure 9.4a. Similarly, if transmission occurs across a Σ3 boundary when uncharged, it also occurs for indentations equidistant from the boundary when hydrogen charged. However, for the more complex case of random high angle boundaries deformation transmission across the grain boundaries is less consistent, as shown in Figure 9.4b. Several random high angle boundaries were selected and indentations made at a similar distance from the boundary. In some cases, transmission occurred when the material was uncharged but not when the material was hydrogen charged. The question then is: are there discernible differences between grain boundary types or pile-up characteristics that alter slip transmission behavior in the presence of hydrogen?

To address changes in slip transmission behavior for random grain boundaries after hydrogen charging, the most easily evaluated characteristic is misorientation. As indicated in Figure 9.1a, boundary 4 has a misorientation of ~48^{o}, while boundaries 5 and 6 have misorientations of ~58^{o} and 59^{o}, respectively. For boundary 4, slip lines are observed on both sides of the grain boundary both before and after charging, indicating slip transmission occurs in both cases. In the case of boundary 5, slip transmission occrurs when uncharged, but does not occur when hydrogen charged. The opposite

behavior is observed for boundary 6. Consequently, boundary misorientation appears to be insufficient in explaining slip transmission behavior in the presence of hydrogen.

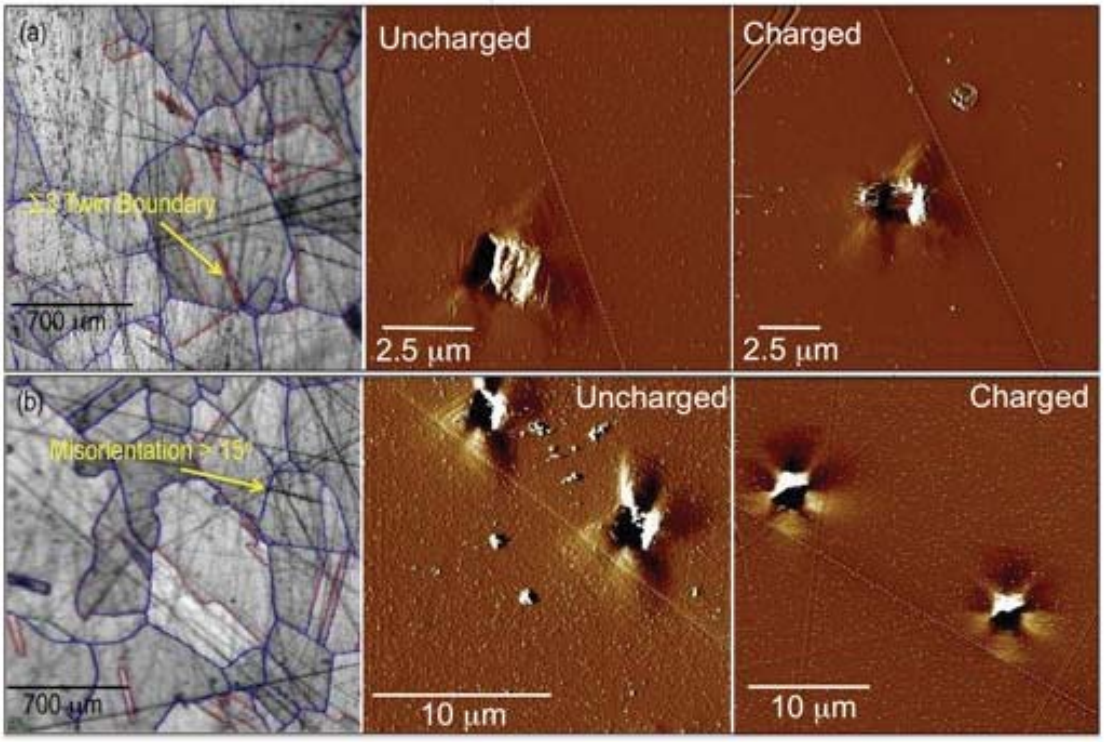

Figure 9.4 EBSD and AFM images of slip transmission characteristics along a Σ3 boundary (a, top) and along a random grain boundary (b, bottom).

Depending on the orientation of the slip system activated by the indentation relative to the grain boundary, slip steps may be generated either parallel to the boundary or nearly perpendicular to it, as noted in Figure 9.5. These preliminary observations suggest that the position of the slip systems which result in a pile-up lobe in the indented grain impact the nature of the resulting slip steps in the adjacent grain. When the pile-up lobes are generated such that slip steps in the indented grain run approximately parallel to the grain boundary the slip steps in the adjacent grain are also parallel to the grain boundary, as shown in Figure 9.5a. This is likely caused by a traditional Hall-Petch type slip-boundary interaction where dislocation motion is impeded by the boundary causing a

pile-up, leading to a stress concentration which in turn activates a dislocation source in the neighboring grain.[209] When the slip steps forming in the indented grain form an acute angle with the grain boundary, then the resultant slip steps in the adjacent grain will also form an acute angle with the boundary (Figure 9.5b), possibly due to slip continuity across the boundary. Continuous slip has been ascribed to screw dislocations or mixed dislocations with predominately screw character; screw dislocations can easily cross-slip and so are unlikely to form strong pile-ups.[211] The Hall-Petch type interaction is often observed for edge or predominately edge dislocations, which can form strong pile-ups because of their limited ability to cross-slip. These results are not meant to ascribe a single or particular mechanism to the activation of slip across a grain boundary in the presence of solute hydrogen, only to note that the indentation technique may be used in further studies to identify specific slip-boundary interactions and elucidate the local misorientation and incident dislocation requirements to either restrict or enhance slip transmission.

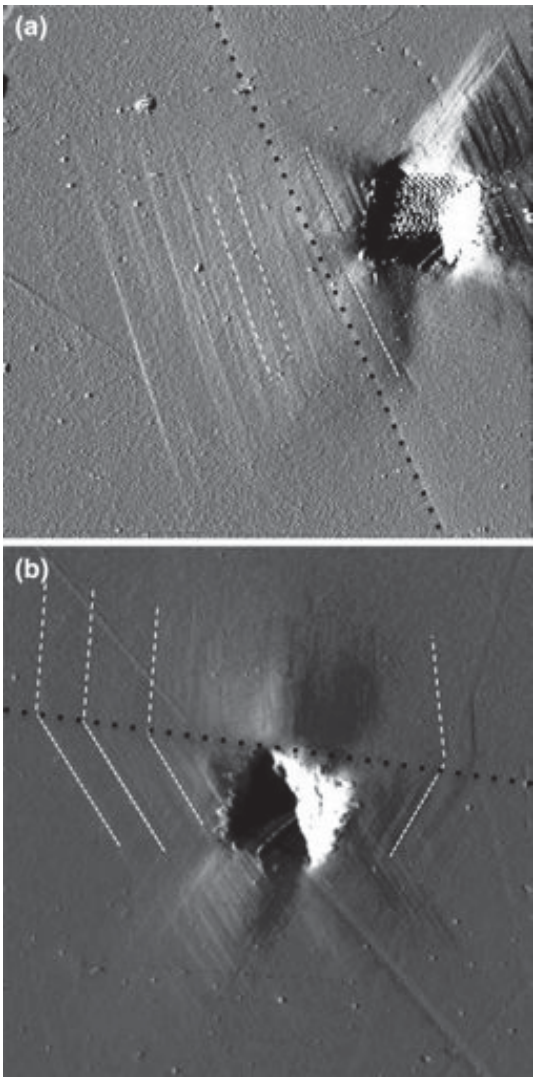

Figure 9.5 Two types of incident-resultant pile-up orientations generated by nanoindentation: (a) incident slip steps that are approximately parallel to the grain boundary result in nearly parallel slip steps in the adjacent grain, while (b) incident slip steps that make an acute angle with the boundary result in slip steps in the adjoining grain which also make acute angles with the boundary.

9.4 Conclusions

Nanoindentation of specifically oriented grain boundaries in Ni-201 reveals three unique observations.

1. Hardness measured in the traditional methods does not vary significantly with charging, but solute hydrogen increases both the total and normalized plastic zone radii produced during indentation in Ni-201, leading to an overall increase in slip step width. The increased plastic zone radii likely arises as a result of the decreased critical stress required to activate Frank-Read sources in the presence of hydrogen, thereby allowing activation of more distant sources. This suggests that the HELP mechanism may be active in the absence of a substantial change in conventionally measured hardness.
2. Increased spacing between slip steps also suggests that cross-slip is restricted when hydrogen-stabilized mixed dislocations are confined to glide on their original slip planes.
3. The behavior of slip transmission in the presence of solute hydrogen appears to be independent of hydrogen content along Σ3 boundaries, but is not always the case for random high angle boundaries. Dislocations may undergo either continuous slip or a Hall-Petch type activation depending on the orientation of the incident pile-up with respect to the grain boundary.

Grain boundary character is an important factor in determining the susceptibility of Ni-based alloys to hydrogen-induced intergranular failure. However, additional investigations will be required to clarify the conditions that must be met locally to either restrict or enhance slip transmission in a hydrogen-charged microstructure.

CHAPTER 10. INTERROGATING HYDROGEN-VACANCY INTERACTIONS

Hydrogen is effectively trapped at open-volume defects, such as vacancies, dislocations, and grain boundaries and the clustering of hydrogen around these defects can lead to the formation of voids,[214] which ultimately leads to the degradation of engineering materials. Studies of hydrogen-vacancy interactions have led to the proposition of a new hydrogen degradation mechanism [215] which emphasizes the importance of vacancies in macroscale fracture processes. This mechanism suggests that hydrogen enhances the formation and agglomeration of vacancies through hydrogen-vacancy interactions during deformation. Ultimately, hydrogen-induced vacancies can agglomerate, forming voids and promoting crack propagation.

Positrons are localized, trapped, and annihilated by vacancies, vacancy clusters, and dislocations,[216] due to the strong Coulomb repulsion from the ion cores; as such, positron annihilation spectroscopy (PAS) is an effective tool for interrogating the effect of hydrogen and plastic deformation on vacancy and void concentration. PAS allows the number of positron states as well as their annihilation rates and relative intensities to be determined. Positrons are delocalized and annihilated via a Bloch state with electrons in the matrix of a perfect crystal. In metals containing vacancies or vacancy clusters, however, the electron density is much lower than in the matrix.[217] Positron annihilation is measured by the positron lifetime and intensity; positron lifetime correlates with the

magnitude of the electron density at the site of positron annihilation and gives information about the open volumes at vacancies. Positron trapping depends on the rearrangement of ions and conduction electrons at the defects as well as the reduction of positron kinetic energy and variation of the electron–positron correlation energy. Positron lifetime in a monovancy is about 50% longer than in the perfect bulk and increases further when vacancies cluster into three-dimensional agglomerates.[216] However, if vacancies or nanovoids contain gas atoms, the positron lifetime decreases due to electron overlap between the trapped gas atoms and positrons.[218,219] Experimental and computational investigations result in a marked decrease in positron lifetime after charging Ni with hydrogen.[214,220]

Thermal desorption spectroscopy (TDS) is a non-isothermic method for interrogating desorption kinetics. In the case of hydrogen desorption, a sample previously charged with hydrogen is continuously heated following a predefined temperature profile while the amount of gas desorbed from the material is recorded. The plot of the flow of desorbed gas as a function of temperature is a TDS spectrum. TDS spectra are usually composed of many desorption peaks, each of which can be associated with a different kinetic process. The main goal of a TDS experiment is to determine binding energy and densities of trap sites.[221] Typically, desorption rates initially increase since the probability for hydrogen release from a trap increases more quickly than the decrease in the content of hydrogen in this trap. Subsequently, desorption rate decreases to zero due to the low hydrogen content remaining in the trap. In general, the activation energy for hydrogen release from a trap dictates the maximum desorption temperature, desorption reaction order, and the heating rate.[222] The peak intensity, on the other hand, depends on the

content of trapped hydrogen and on the heating rate.[223] Qualitatively, the maximum desorption temperature reflects the trapping intensity—a higher temperature indicates a higher activation energy for hydrogen release. The trap density is characterized by the total amount of gas atoms desorbed during heating.[222]

Preliminary PAS and TDS results will be presented in this chapter.

10.1 Experimental Procedures

10.1.1 Material Preparation

A commercially pure nickel alloy, Ni-201, was used for this investigation. Two plates with different grain sizes were supplied by ATI Allegheny Ludlum. Plate 1 had an as-received grain size of 50 μm and impurities (in wt.%) of 0.01 C, 0.01 Mn, < 0.01 Fe, 0.05 Si, < 0.01 Cu, and < 0.001 S. Plate 2 had an as-received grain size of 200 μm and impurities (in wt.%) of 0.01 C, 0.01 Mn, < 0.01 Fe, 0.05 Si, < 0.01 Cu, and < 0.001 S. Grain boundary segregation, especially of S in Ni,[162] has been shown to dramatically alter hydrogen effects on dislocation-grain boundary interactions in commercially pure materials [204]; to mitigate this issue, an alloy grade with an ultralow sulfur concentration was chosen for this investigation. The as-received Ni-201 Plate 2 was annealed at 900^{o}C for 1 hr, stimulating grain growth; this heat treatment resulted in a grain size of 1 mm. Three sets of samples were extracted from each plate. Sample set 1 consisted of specimens for PAS (dimensions: 4 mm x 4mm x 0.5 mm) and TDS (dimensions: 4 mm x 6 mm x 0.3 mm) machined from Plate 1. Identical specimens were machined from Plate 2, and will be referred to as Sample set 2. Sample sets 3 and 4 consisted of tensile bars machined from Plate 1 (set 3) and Plate 2 (set 4), which had a gauge section diameter of 4

mm. After straining, specimens for PAS and TDS were extracted from the tensile bars. Surfaces were finished with emery paper No. 2400. Also included in the test matrix were single crystal (SC) Ni specimens and a high purity (5N) Ni sample as a reference, both provided by Aalto University.

10.1.2 Tensile Straining

Uniaxial tensile tests were conducted on as-machined and hydrogen charged specimens from set 3 and set 4 both at room temperature (300 K) and in a liquid nitrogen bath (77 K). Tensile straining was performed using a MTS 810 servo-hydraulic mechanical testing system under displacement control at a displacement rate of 0.01 mm/s. Displacement was controlled such that the samples were strained to ~10%. At such low applied strains, all deformation should be localized the gauge section of the sample, thus total strain was approximated by calculating the reduction in area, *RA*, after straining:

Equation 10.1 $$RA = (d_i^2 - d_f^2)/d_i^2,$$

where d_i is the initial diameter of the gauge section, and d_f is the final diameter after tensile straining.

10.1.3 Positron Annihilation Spectroscopy

PAS measurements were carried out with the positron lifetime method using a conventional fast–fast spectrometer in collinear geometry [224] with a time resolution of 250 ps. In this scheme, the positron source, a ^{22}Na salt deposited on 1.5 μm thick metal foil, is sandwiched between two identical specimen pieces. The lifetime spectrum was

analyzed as the sum of the exponential decay components convoluted with the Gaussian resolution function of the spectrometer after subtracting the constant background and annihilations in the source material.

10.1.4 Thermal Desorption Spectroscopy

Hydrogen thermal desorption spectra were obtained at a constant heating rate of 6 K min^{-1} in the temperature range from 25 to 850 °C by measuring the hydrogen partial pressure in the UHV chamber of a TDS apparatus. The basic vacuum in the apparatus was kept better than 10^{-7} mbar.

10.1.5 Hydrogen Charging

Atomic hydrogen was dissolved into the PAS specimens, TDS specimens, and the tensile bars by thermally charging in high-pressure hydrogen gas. The specimens were inserted into a thick-walled A-286 stainless steel pressure vessel and then placed in a furnace. Residual gases were removed from the sealed pressure vessel and gas-handling manifold using a purging and evacuating sequence. Three purge/evacuation cycles were conducted with helium, followed by three cycles with hydrogen. Once the purging/evacuation cycles were completed, the pressure vessel was heated and filled with 99.9999% hydrogen gas. Charging was conducted at elevated temperature to enhance hydrogen diffusion, thereby minimizing charging times, but temperatures were limited to avoid thermally activated microstructural changes in the nickel. A charging cycle was selected to achieve a hydrogen concentration of ~3000 appm. Samples were charged at a hydrogen gas pressure of 62 MPa and a temperature of 300^{o}C for 144 hrs. Hydrogen-

charged specimens were stored at subfreezing temperatures and transported cryogenically to minimize hydrogen loss.

10.1.6 Testing Procedure

PAS and TDS measurements were carried out for sample sets 1 and 2 in the as-received or as-annealed conditions using a Cu foil source. These eight specimens, as well as the tensile bars from sample sets 3 and 4 were then thermally charged with hydrogen following the procedure outlined above. Upon removal from the pressure vessel the specimens were immediately stored in a cryogenic freezer. After charging the tensile bars were strained to 10% at room temperature (RT) or 77 K. PAS and TDS specimens were extracted from the gauge length of the tensile bars. Disks with a thickness of 1 mm were cut in the transverse direction and then polished to achieve a final thickness of 0.5 μm for PAS and TDS. Samples were stored at cryogenic temperatures between all preparation steps.

Simultaneously, hydrogen-free tensile bars from sets 3 and 4 were strained to 10% at RT or 77 K and then PAS and TDS specimens were extracted from the gauge section of the as-strained tensile bars as described above. PAS and TDS measurements were subsequently conducted for all the H-charged specimens and the H-free samples. A Ni foil source was used for PAS for these studies.

10.2 Results

10.2.1 Thermal Desorption Spectroscopy

Hydrogen flux calculated from thermal desorption spectra for the SC, 5N Reference, and sample sets 1 and 2 are shown in Figure 10.1. The hydrogen content in the samples increases after hydrogen charging, but the hydrogen pressures detected by TDS indicate that the total dissolved hydrogen content in these samples is on the order of 300- 500 appm. This value falls short of the desired hydrogen content of 3000 appm. However, examining Figure 10.2 indicates a hydrogen concentration in sample sets 3 and 4 on the order of 3000 appm. Comparing these figures suggests that the hydrogen charging process was successful and that cryogenic sample storage drastically slows hydrogen mobility, but that hydrogen egress from sample sets 1 and 2 was swift enough to cause a an order of magnitude hydrogen loss. Enhanced hydrogen egress likely occurs during the 16-hour cooling cycle of the pressure vessel after charging—the diffusivity of hydrogen increases substantially at elevated temperatures. Because the specimens are very thin, hydrogen diffusing out of the near-surface regions of the sample cause steep concentration gradients and reduce the overall bulk hydrogen concentration.

A single main desorption peak is observed for the SC and 5N Reference samples as well as for sample sets 1 and 2, both in the H-free and H-charged conditions. Conversely, for the pre-strained specimens, a secondary desorption peak at a higher temperature appears after hydrogen charging. This may be linked to the presence of stronger trap sites after straining. The effect is particularly pronounced for samples strained at 77 K, likely the result of limited hydrogen mobility at cryogenic temperatures.

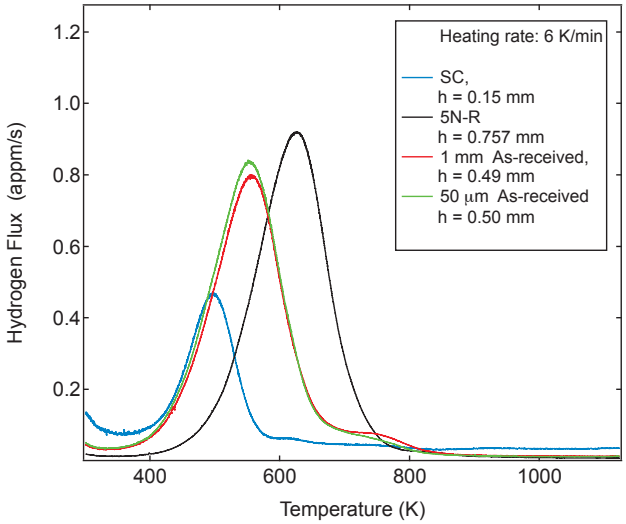

Figure 10.1 Hydrogen flux for 5N reference sample, single crystal sample, and as-received materials with 1 mm grain size and 50 μm grain size. Sample thicknesses, *h*, are tabulated in the legend.

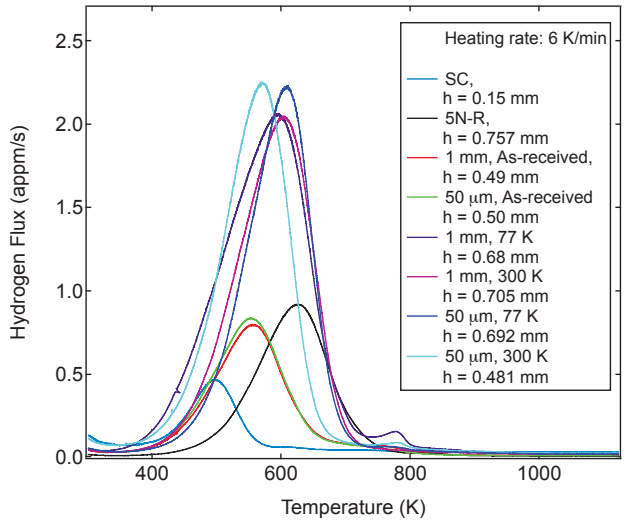

Figure 10.2 Hydrogen flux for samples with 1 mm grain size and 50 μm grain size strained to ~10% at 77 K and 300 K. As-received curves are included for comparison. . Sample thicknesses, *h*, are tabulated in the legend.

10.2.2 Positron Annihilation Spectroscopy

Average values for lifetimes and intensities for all samples are collected in Table 10.1. Only a single lifetime component is detected for the 5N reference sample, both before and after hydrogen charging. The value decreases only slightly upon hydrogen charging and is close to the tabulated bulk lifetime for pure Ni, 120 ps.[219] A slight decrease in lifetime could indicate that hydrogen is dissolved in the lattice, inhibiting positron residence. Positrons moving through the bulk more quickly would be manifested as a decrease in positron lifetime. The intensity of the positron lifetime in both cases is 100%, that is, positrons are not trapped by impurities or lattice defects.

In contrast with the reference sample, the SC sample exhibits two lifetime components, a short lifetime, τ_1, and a long lifetime, τ_2, and an overall increase in average lifetime, τ_{ave}, after hydrogen charging. Two lifetime components connotes the existence of multiple positron trapping features, such as lattice sites and open volume defects. Increasing positron lifetime suggests the concentration of defects where positrons can reside in the material has increased, slowing down their travel. These open volume defects are most likely vacancies.

Similar lifetime increases are observed for the samples from sets 3 and 4, which were charged and then strained at 300 K or 77 K. Most importantly, both the lifetimes and intensities for the hydrogen charged specimens evolve with time. Hydrogen slowly diffuses out of the lattice causing an increase in the apparent positron lifetime. It is likely that the vacancy concentration in the strained samples is higher than that in the as-annealed material, as positron lifetimes are longer than both the typical bulk lattice lifetime value and the measured lifetimes for the as-annealed sample. The details of the

time evolutions differ with straining temperature. As shown in Figure 10.3a, the average lifetime for the 1mm grain size samples strained at 300 K increases linearly approximately 7 ps over 24 hours; the average lifetime of the sample strained at 77 K (Figure 10.3b), however, increases approximately 13 ps over 24 hours. Also the 300 K samples seems to increase in two phases—exponentially from ~205-211 ps and linearly from ~211-218 ps. It is likely that less hydrogen diffused out of the sample strained at 77 K during testing due to limited mobility at cryogenic temperatures. Decreased dislocation mobility at low temperature may also impact the generation of vacancies during straining, which will be detected as a change in the positron lifetime spectra. Slight variation in the intensities of τ_1 and τ_2 with time is shown in Figure 10.4a and Figure 10.4b. In general τ_1 decreases while τ_2 increases, suggesting that as more hydrogen diffuses out of the lattice the long lifetime component becomes the controlling factor in increasing τave. It is also important to note that there is no evolution of τ_{ave} or intensities with time for the hydrogen-free samples, as expected. Because of the time evolution detected for the 1 mm grain size materials, positron lifetimes were measured for 72 hours for the hydrogen-charged samples with a 50 μm grain size, while the hydrogen-free samples were measured for 24 hours. Similar trends are observed for samples with a grain size of 50 μm, strained at 300 K and 77 K. Time evolution of τ_{ave} for these samples are shown in Figure 10.5a and Figure 10.5b, while the intensities for the two lifetime components are presented in Figure 10.6a and Figure 10.6b. Again, there is no time evolution for the hydrogen-free material.

Table 10.1 Average lifetime, τ_{ave}, short lifetime, τ_2, and its intensity, I_1, and long lifetime, τ_2, and intensity, I_2 as a function of sample condition.

Sample Condition	τ_{Ave} *(ps)*	τ_1 *(ps)*	I_1 *(%)*	τ_2 *(ps)*	I_2 *(%)*
5N-R	120.5	120.5	100	––	--
5N-R with H	116.3±0.7	116.3±0.7	100	––	--
SC	138.3±1.0	93.0±2.0	57.4±1.6	199.0±2.0	42.6±1.6
SC with H	149.6±2.3	111.4±5.7	68.5±3.6	233.3±8.3	31.5±3.6
		1 mm Grain Size			
AR	152.19±1.1	134.09±2.9	84.83±3.3	255.34±14.2	15.17±3.3
AR with H	152.2±1.1	134±3.2	85±3.0	255.3±12.4	15±3.0
77K	179.8±0.7	161.6±3.5	78.4±4.7	247.3±10.2	21.5±4.7
77K with H	213.6±3.4	169.5±6.1	68±5.6	307.1±11.6	32±5.6
300K	202.8±0.9	160.8±2.9	70.6±1.6	303.4±3.8	29.3±1.6
300K with H	203.2±1.8	162.6±3.7	71.6±2.6	308.3±0	28.3±2.6
		50 μm Grain Size			
AR	155.96±1.1	136.0±4.0	74.7±6.6	215.75±10.5	25.3±6.6
AR with H	156.0±1.0	136.0±4.0	74.7±6.5	215.75±10.5	25.3±6.5
77K	196.6± 0.9	166.1±3.5	73.9±3.8	283.9±8.9	26.03±3.8
77K with H	212.7±0.9	167.0±3.0	68.0±2.3	310.1±6.5	31.9±2.3
300K	195.5±0.9	166.1±2.6	77.6±2.6	297.9±8.1	22.4±2.6
300K with H	209.6±2.7	166.3±2.6	70.6±2.1	313.9±5.6	29.4±2.1

.

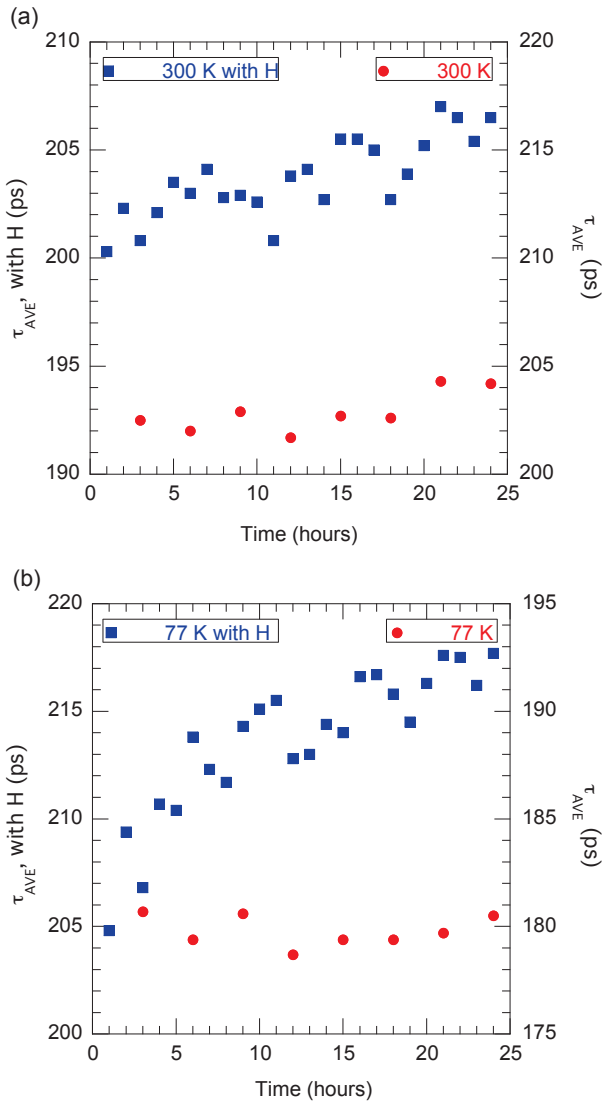

Figure 10.3 Time evolution of average lifetimes for polycrystalline Ni samples with a 1mm grain size, hydrogen charged and strained to 10% at 300 K (a) and 77 K (b).

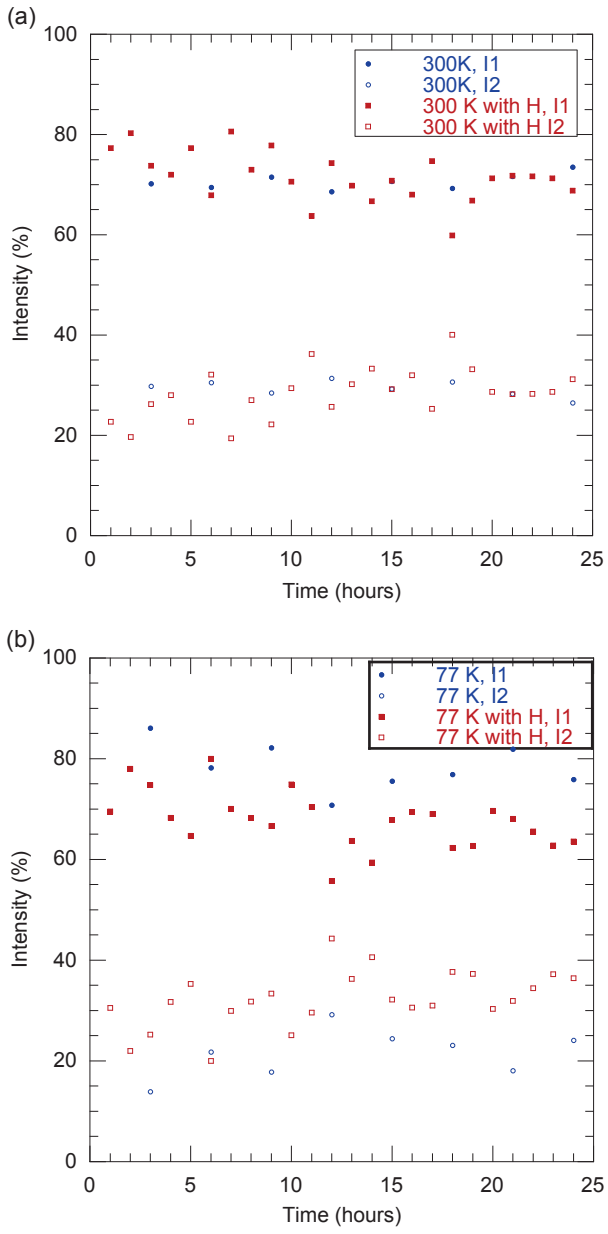

Figure 10.4 Time evolution of short positron lifetime intensity, I_1, and long lifetime intensity, I_2, for polycrystalline Ni samples with a 1mm grain size, hydrogen charged and strained to 10% at 300 K (a) and 77 K (b).

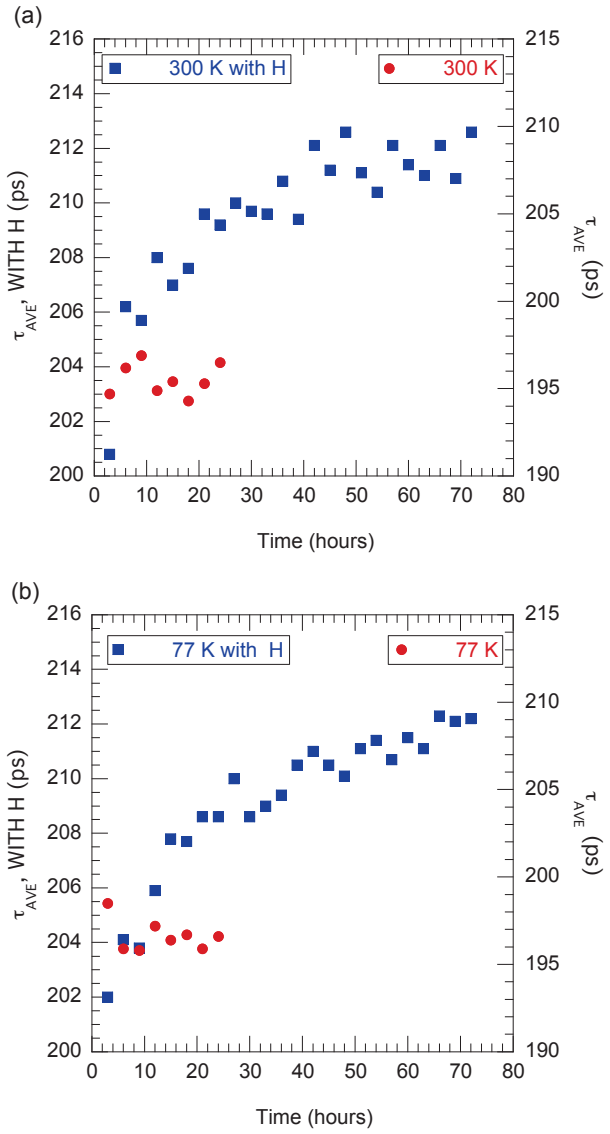

Figure 10.5 Time evolution of average lifetimes for polycrystalline Ni samples with a 50 μm grain size, hydrogen charged and strained to 10% at 300 K (a) and 77 K (b).

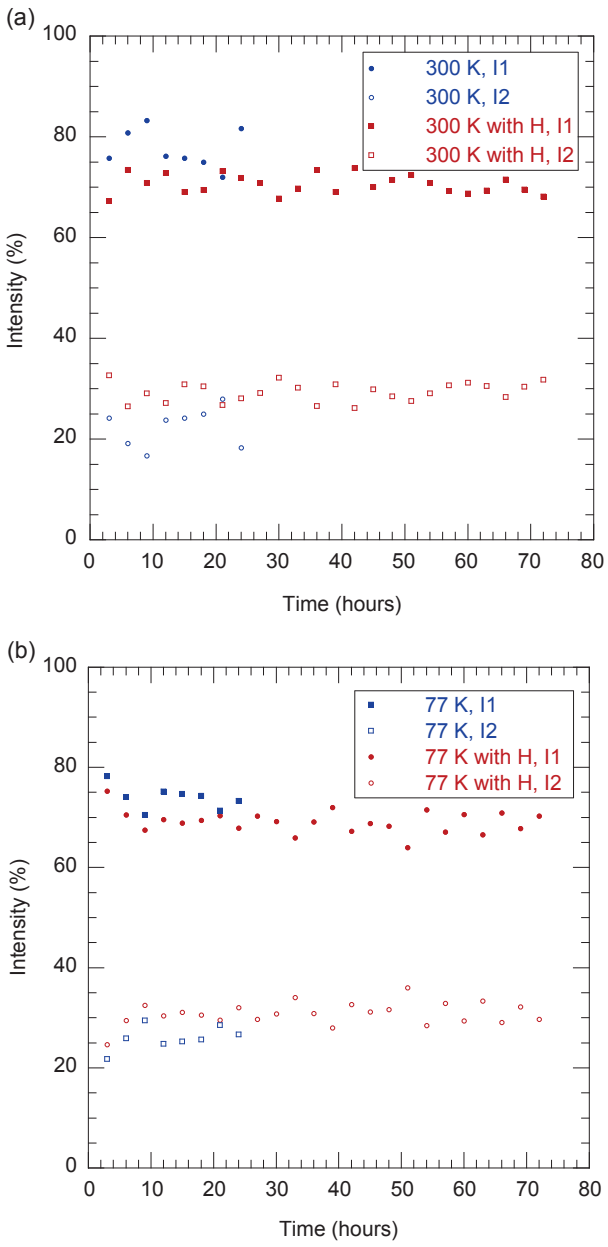

Figure 10.6 Time evolution of short positron lifetime intensity, I_1, and long lifetime intensity, I_2, for polycrystalline Ni samples with a 50 μm grain size, hydrogen charged and strained to 10% at 300 K (a) and 77 K (b).

10.3 Summary and Conclusions

Only preliminary results from an ongoing investigation have been presented in this chapter. Complete data analysis will be published in an archival journal at the conclusion of the work. To this point, however, some broad conclusions may be drawn:

1. Hydrogen dissolved in a Ni lattice can be successfully quantified using thermal desorption spectroscopy, while positron annihilation spectroscopy can be used to confirm that hydrogen resides in lattice sites in a high purity, defect free specimen.
2. High temperature, gas-phase charging induces vacancy formation in both single crystalline and polycrystalline Ni.
3. Uniaxial tensile deformation of hydrogen-charged polycrystalline Ni at cryogenic temperature causes a measurably different microstructural response than straining at room temperature. The grain size of the material also impacts the microstructure. The measured differences in positron lifetime and desorption temperature are attributed to vacancy generation or agglomeration.

CHAPTER 11. CONCLUSIONS AND FUTURE WORK

Designing materials for use in extreme environments—whether that is under high stresses, pressures, temperatures, or in a harsh atmosphere, or both—requires linking changes in the microstructure and properties of engineering alloys with altered performance in each condition. Until recently, experiments of this type, and accompanying computational work, have focused on either bulk samples or single crystal specimens and extrapolated behavior to engineering-scale materials. The challenge in this work has been to bridge the gap between microscale and macroscale by combining nanoscale measurement techniques with bulk characterization methods on model materials and engineering systems with the ultimate goal of predicting and controlling the microstructural response of engineering systems to perform reliably in harsh environments.

Microscale and macroscale mechanical properties can be linked by nanoindentation of polycrystalline specimens of model alloy systems. Systematically varying the sampled volume and the grain orientation indented highlights the interplay between anisotropy and volume of material tested on the yield behavior of Ni 200. Subsequently adding variation in sample preparation condition, representative of changing dislocation density, markedly affects plasticity.

Nanoindentation has also be coupled diffraction and atomic force microscopy techniques to interrogate the effect of dissolved hydrogen on microstructure and plasticity of Ni 201, a model alloy known to suffer from macroscale intergranular fracture in hydrogen atmospheres. In the past it has been suggested that hydrogen enhanced localized plasticity and hydrogen enhanced decohesion are competitive mechanisms, but the present work suggests that they may be complementary mechanisms in hydrogen degradation of Ni 201. It is evident that hydrogen serves to enhance dislocation mobility, while limiting cross-slip and impacts the likelihood of slip transmission across grain boundaries as a function of grain boundary misorientation. This result represents an important step in understanding the impact and coupling of grain boundary misorientation and grain character on macroscale failure. Further investigation will help to develop microstructural parameters that can guide grain boundary engineering techniques to mitigate intergranular fracture of Ni-containing alloys used in hydrogen service.

It is also apparent that hydrogen alters the microstructure in such a way that there is a measureable difference in the indentation modulus irrespective of grain orientation. While this may indicate that hydrogen serves to decrease the cohesive force, ultimately leading to easier atomic separation, these data cannot account for the importance of vacancies in hydrogen-related failure. To assess the impact of vacancies, positron annihilation spectroscopy and thermal desorption spectroscopy have been applied to hydrogen-free and hydrogen-charged specimens in annealed and pre-strained conditions. Preliminary results reveal differences in both vacancy concentration and hydrogen trapping as a function of straining temperature and hydrogen concentration. Ongoing

studies aim to identify vacancy agglomeration or void formation as a function of grain size and compare that microstructural information with positron lifetime evolution and desorption energy to more accurately understand the interrelationships between hydrogen charging and deformation on vacancy formation/agglomeration. Those results may serve to de-convolute measured changes in elastic properties of hydrogen charged Ni.

Linking microscale properties with macroscale performance is also important for oxide-substrate systems that will be used in harsh environments; many of the same techniques applied to study hydrogen degradation can also be used to investigate the reliability of oxide coatings used as passive authentication structures, or “tags”. The fluence of a nanosecond pulsed laser beam has been successfully tailored to irradiate the surface of a metal component such that only the top few microns of the component melt, inducing a pyrolitic reaction with the gasses in the atmosphere, to grow oxide coatings of various thicknesses and colors. For the first time fracture behavior, electromechanical performance, and environmental resistance of oxides fabricated on SS 304L and CP II Ti were successfully determined by combining multiple indentation techniques and high resolution microscopy. In all cases, the coatings are mechanically robust and well adhered to the substrate. The Ti oxide system is environmentally stable, as expected. The stainless steel systems, however, are susceptible degradation in chloride containing environments, except when the oxides have thickness between approximately 100 and 150 nm. Oxides within this thickness range are continuous and single phase—they do not suffer from mudflat cracking like their thicker, dual phase counterparts and chloride does not appear to diffuse through the oxide to the Cr-depleted substrate—and as such they are protective.

Layered oxides with total thicknesses similar to the single layer films were successfully fabricated using sequential irradiation in an attempt to extend the protective thickness range. The layered films are mechanically robust and well adhered to the substrates. The coatings are more resistant to chloride attack than single layer films, but they do not prevent corrosion of the underlying Cr-depleted substrate. Future experiments should be conducted where the component surface is pre-treated to increase the Cr concentration in the near-surface region. This may prevent depletion of Cr below the critical 12 wt. % value necessary for corrosion resistance during subsequent laser processing. Solving the Cr-depletion problem should result in an oxide-substrate system that is both mechanically robust and environmentally stable. Oxide “tags” could then be used reliably in harsh service conditions, enabling accurate monitoring of long-term component stability.

LIST OF REFERENCES

LIST OF REFERENCES

1. Frick, C. P., Clark, B. G., Orso, S., Schneider, A. S. & Arzt, E. Size effect on strength and strain hardening of small-scale [111] nickel compression pillars. *Mater. Sci. Eng. A* **489,** 319–329 (2008).

2. Page, T. F., Oliver, W. C. & McHargue, C. J. The deformation behavior of ceramic crystals subjected to very low load (nano)indentations. *J. Mater. Res.* **7,** 450–473 (2011).

3. Huang, Y. *et al.* A model of size effects in nano-indentation. *J. Mech. Phys. Solids* **54,** 1668–1686 (2006).

4. Böhm, J. *et al.* Tensile testing of ultrathin polycrystalline films: A synchrotron-based technique. *Rev. Sci. Instrum.* **75,** 1110 (2004).

5. Gerberich, W. W., Tymiak, N. I., Grunlan, J. C., Horstemeyer, M. F. & Baskes, M. I. Interpretations of Indentation Size Effects. *J. Appl. Mech.* **69,** 433 (2002).

6. Doerner, M. F. & Nix, W. D. A method for interpreting the data from depth-sensing indentation instruments. *J. Mater. Res.* **1,** 601–609 (1986).

7. Oliver, W. C. & Pharr, G. M. Measurement of hardness and elastic modulus by instrumented indentation: Advances in understanding and refinements to methodology. *J. Mater. Res.* **19,** 3–20 (2004).

8. Venkataraman, S. K., Kohlstedt, D. L. & Gerberich, W. W. Continuous microindentation of passivating surfaces. *J. Mater. Res.* **8,** 685–688 (1993).

9. Kelchner, C., Plimpton, S. & Hamilton, J. Dislocation nucleation and defect structure during surface indentation. *Phys. Rev. B* **58,** 11085–11088 (1998).

10. Schuh, C. a. & Lund, A. C. Application of nucleation theory to the rate dependence of incipient plasticity during nanoindentation. *J. Mater. Res.* **19,** 2152–2158 (2004).

11. Zhu, T. & Li, J. Ultra-strength materials. *Prog. Mater. Sci.* **55,** 710–757 (2010).

12. Ma, L., Morris, D. J., Jennerjohn, S. L., Bahr, D. F. & Levine, L. Finite element analysis and experimental investigation of the Hertzian assumption on the characterization of initial plastic yield. *J. Mater. Res.* **24,** 1059–1068 (2009).

13. Minor, A. M. *et al.* A new view of the onset of plasticity during the nanoindentation of aluminium. *Nat. Mater.* **5,** 697–702 (2006).

14. Bahr, D., Jennerjohn, S. & Morris, D. Dislocation nucleation and multiplication in small volumes: The onset of plasticity during indentation testing. *JOM J. Miner. Met. Mater. Soc.* **61,** 56–60 (2009).

15. Zbib, A. A. & Bahr, D. F. Dislocation Nucleation and Source Activation during Nanoindentation Yield Points. *Metall. Mater. Trans. A* **38,** 2249–2255 (2007).

16. Schuh, C. A., Mason, J. K. & Lund, A. C. Quantitative insight into dislocation nucleation from high-temperature nanoindentation experiments. *Nat. Mater.* **4,** 617–621 (2005).

17. Betteridge, W. *Nickel and Its Alloys*. 66 (Ellis Horwood Ltd, 1984).

18. Johnson, K. L. *Contact Mechanics*. (Cambridge University Press, 1985).

19. Ma, L., Morris, D. J., Jennerjohn, S. L., Bahr, D. F. & Levine, L. E. The role of probe shape on the initiation of metal plasticity in nanoindentation. *Acta Mater.* **60,** 4729–4739 (2012).

20. Corcoran, S. G., Colton, R. J., Lilleodden, E. T. & Gerberich, W. W. Anomalous plastic deformation at surfaces: Nanoindentation of gold single crystals. *Phys. Rev. B* **55,** R16057–R16060 (1997).

21. Kiely, J. & Houston, J. Nanomechanical properties of Au (111), (001), and (110) surfaces. *Phys. Rev. B* **57,** 12588–12594 (1998).

22. Wang, W., Jiang, C. B. & Lu, K. Deformation behavior of Ni3Al single crystals during nanoindentation. *Acta Mater.* **51,** 6169–6180 (2003).

23. Li, T. L., Gao, Y. F., Bei, H. & George, E. P. Indentation Schmid factor and orientation dependence of nanoindentation pop-in behavior of NiAl single crystals. *J. Mech. Phys. Solids* **59,** 1147–1162 (2011).

24. Salehinia, I., Lawrence, S. K. & Bahr, D. F. The effect of crystal orientation on the stochastic behavior of dislocation nucleation and multiplication during nanoindentation. *Acta Mater.* (2012). doi:10.1016/j.actamat.2012.11.019

25. Salehinia, I., Perez, V. & Bahr, D. F. Effect of vacancies on incipient plasticity during contact loading. *Philos. Mag.* **92,** 550–570 (2012).

26. Salehinia, I. & Bahr, D. F. The impact of a variety of point defects on the inception of plastic deformation in dislocation-free metals. *Scr. Mater.* **66,** 339–342 (2012).

27. Wiedersich, H. Hardening mechanisms and the theory of deformation. *JOM* **16,** 425–430 (1964).

28. Wang, W. *et al.* Size effects and strength fluctuation in nanoscale plasticity. *Acta Mater.* **60,** 3302–3309 (2012).

29. Lorenz, D. *et al.* Pop-in effect as homogeneous nucleation of dislocations during nanoindentation. *Phys. Rev. B* **67,** 1–4 (2003).

30. Michalske, T. a. & Houston, J. E. Dislocation nucleation at nano-scale mechanical contacts. *Acta Mater.* **46,** 391–396 (1998).

31. Bahr, D. F., Kramer, D. E. & Gerberich, W. W. Non-linear deformation mechanisms during nanoindentation. *Acta Mater.* **46,** 3605–3617 (1998).

32. Chiu, Y. L. & Ngan, A. H. W. Time-dependent characteristics of incipient plasticity in nanoindentation of a Ni 3 Al single crystal. *Acta Mater.* **50,** 1599–1611 (2002).

33. Tymiak, N. I., Kramer, D. E., Bahr, D. F., Wyrobek, T. J. & Gerberich, W. W. Plastic strain and strain gradients at very small indentation depths. *Acta Mater.* **49,** 1021–1034 (2001).

34. Ngan, A. H. W., Zuo, L. & Wo, P. C. Probabilistic nature of the nucleation of dislocations in an applied stress field. *Scr. Mater.* **54,** 589–593 (2006).

35. Gane, N. & Bowden, F. P. Microdeformation of Solids. *J. Appl. Phys.* **39,** 1432 (1968).

36. Zhu, T. & Li, J. Ultra-strength materials. *Prog. Mater. Sci.* **55,** 710–757 (2010).

37. Li, J., Van Vliet, K. J., Zhu, T., Yip, S. & Suresh, S. Atomistic mechanisms governing elastic limit and incipient plasticity in crystals. *Nature* **418,** 307–310 (2002).

38. Lucca, D. A., Klopfstein, M. J., Ghisleni, R. & Cantwell, G. Investigation of Polished Single Crystal ZnO by Nanoindentation. *Ann. CIRP* **51,** 483–486 (2002).

39. Yan, J. *et al.* Nanoindentation tests on diamond-machined silicon wafers. *Appl. Phys. Lett.* **86,** 181913 (2005).

40. Lodes, M. a., Hartmaier, a., Göken, M. & Durst, K. Influence of dislocation density on the pop-in behavior and indentation size effect in CaF2 single crystals: Experiments and molecular dynamics simulations. *Acta Mater.* **59,** 4264–4273 (2011).

41. Wang, Z., Bei, H., George, E. P. & Pharr, G. M. Influences of surface preparation on nanoindentation pop-in in single-crystal Mo. *Scr. Mater.* **65,** 469–472 (2011).

42. Barnoush, A., Welsch, M. T. & Vehoff, H. Correlation between dislocation density and pop-in phenomena in aluminum studied by nanoindentation and electron channeling contrast imaging. *Scr. Mater.* **63,** 465–468 (2010).

43. Shim, S., Bei, H., George, E. P. & Pharr, G. M. A different type of indentation size effect. *Scr. Mater.* **59,** 1095–1098 (2008).

44. Larson, D. J. *et al.* Field-ion specimen preparation using focused ion-beam milling. *Ultramicroscopy* **79,** 287–293 (1999).

45. Kiener, D., Motz, C., Rester, M., Jenko, M. & Dehm, G. FIB damage of Cu and possible consequences for miniaturized mechanical tests. *Mater. Sci. Eng. A* **459,** 262–272 (2007).

46. Poldi, G. *et al.* Experimental observation of FIB induced lateral damage on silicon samples. *Microelectron. Eng.* **86,** 548–551 (2009).

47. Bei, H., Shim, S., Miller, M. K., Pharr, G. M. & George, E. P. Effects of focused ion beam milling on the nanomechanical behavior of a molybdenum-alloy single crystal. *Appl. Phys. Lett.* **91,** 111915 (2007).

48. Giannuzzi, L. a, Geurts, R. & Ringnalda, J. 2 keV Ga+ FIB Milling for Reducing Amorphous Damage in Silicon. *Microsc. Microanal.* **11,** 2004–2005 (2005).

49. Scott, J. *et al.* Sample preparation for nanoanalytical electron microscopy using the FIB lift-out method and low energy ion milling. *J. Phys. Conf. Ser.* **26,** 223–226 (2006).

50. Wardle, S. T., Lin, L. S., Cetel, A. & Adams, B. L. Orientation Imaging Microscopy: Monitoring Residual Stress Profiles in Single Crystals using an Image-Quality Parameter, IQ. in *Proc. 52nd Annu. Meet. Microsc. Soc. Am.* (Bailey, G. W. & Garratt-Reed, A. J.) 680–681 (San Francisco Press, 1994).

51. Calcagnotto, M., Ponge, D., Demir, E. & Raabe, D. Orientation gradients and geometrically necessary dislocations in ultrafine grained dual-phase steels studied by 2D and 3D EBSD. *Mater. Sci. Eng. A* **527,** 2738–2746 (2010).

52. Kubin, L. . & Mortensen, a. Geometrically necessary dislocations and strain-gradient plasticity: a few critical issues. *Scr. Mater.* **48,** 119–125 (2003).

53. Gao, H., Huang, Y., Nix, W. D. & Hutchinson, J. W. Mechanism-based strain gradient plasticity--I. Theory. *J. Mech. Phys. Solids* **47,** 1239–11263 (1999).

54. Wright, S., Field, D. & Dingley, D. *Electron Backscatter Diffraction in Materials Science*. chp. 13 (Kluwer Academic, 2000).

55. Hughes, D., Hansen, N. & Bammann, D. Geometrically necessary boundaries, incidental dislocation boundaries and geometrically necessary dislocations. *Scr. Mater.* **48,** 147–153 (2003).

56. Taylor, J. W. Dislocation Dynamics and Dynamic Yielding. *J. Appl. Phys.* **36,** 3146 (1965).

57. Tabor, D. *The Hardness of Metals*. 105 (Oxford University Press, 1951).

58. El-Dasher, B. ., Adams, B. . & Rollett, a. . Viewpoint: experimental recovery of geometrically necessary dislocation density in polycrystals. *Scr. Mater.* **48,** 141–145 (2003).

59. Littlewood, P. D., Britton, T. B. & Wilkinson, a. J. Geometrically necessary dislocation density distributions in Ti–6Al–4V deformed in tension. *Acta Mater.* **59,** 6489–6500 (2011).

60. Gane, N. & Cox, J. M. The micro-hardness of metals at very low loads. *Philos. Mag.* **22,** 0881–0891 (1970).

61. Ma, Q. & Clarke, D. R. Size dependent hardness of silver single crystals. *J. Mater. Res.* **10,** 853–863 (1995).

62. Lehmann, E. L. *Nonparametrics: Statistical Methods Based on Ranks*. (Holden-Day, Inc., 1975).

63. Oliver, W. C. & Pharr, G. M. An improved technique for determining hardness and elastic modulus using load and displacement sensing indentation experiments. *J. Mater. Res* **7,** 1564–1583 (1992).

64. Lawrence, S. K., Bahr, D. F. & Zbib, H. M. Crystallographic orientation and indenter radius effects on the onset of plasticity during nanoindentation. *J. Mater. Res.* **27,** 3058–3065 (2012).

65. Ramos, K. J., Hooks, D. E. & Bahr, D. F. Direct observation of plasticity and quantitative hardness measurements in single crystal cyclotrimethylene trinitramine by nanoindentation. *Philos. Mag.* **89,** 2381–2402 (2009).

66. Bei, H., Shim, S., Pharr, G. M. & George, E. P. Effects of pre-strain on the compressive stress–strain response of Mo-alloy single-crystal micropillars. *Acta Mater.* **56,** 4762–4770 (2008).

67. Li, T. L., Bei, H., Morris, J. R., George, E. P. & Gao, Y. F. Scale effects in the convoluted thermal / spatial statistics of plasticity initiation in small stressed volumes during nanoindentation. *Mater. Sci. Technol.* **28,** 1055–1059 (2012).

68. Wautelet, M. Laser-assisted reaction of metas with oxygen. *Appl. Phys. A Mater. Sci. Process.* **50,** 131–139 (1990).

69. Hongyu, Z. SIMTech Technical Report PT/01/004/AM. (2001).

70. Pérez del Pino, A., Fernández-Pradas, J. ., Serra, P. & Morenza, J. . Coloring of titanium through laser oxidation: comparative study with anodizing. *Surf. Coatings Technol.* **187,** 106–112 (2004).

71. Gyorgy, E., Perez del Pino, A., Serra, P. & Morenza, J. L. Structure formation on titanium during oxidation induced by cumulative pulsed Nd:YAG laser irradiation. *Appl. Phys. A Mater. Sci. Process.* **78,** 765–770 (2004).

72. Wong, M. H., Cheng, F. T. & Man, H. C. Laser oxidation of NiTi for improving corrosion resistance in Hanks' solution. *Mater. Lett.* **61,** 3391–3394 (2007).

73. Pérez del Pino, A., Serra, P. & Morenza, J. . Coloring of titanium by pulsed laser processing in air. *Thin Solid Films* **415,** 201–205 (2002).

74. Yilbas, B. S., Shuja, S. Z. & Hashmi, M. S. J. A numerical solution for laser heating of titanium and nitrogen diffusion in solid. *J. Mater. Process. Technol.* **136,** 12–23 (2003).

75. Drory, M. D., Thouless, M. D. & Evans, A. G. On the decohesion of residually stressed thin films. *Acta Met.* **36,** 2019–2028 (1988).

76. Thouless, M. D. Some mechanics for the adhesion of thin films. *Thin Solid Films* **181,** 270–278 (1990).

77. Thouless, M. D., Olsson, E. & Gupta, A. Cracking of brittle films on elastic substrates. *Acta Met. Mater.* **40,** 1287–1292 (1992).

78. Hu, M. S. & Evans, A. G. The Cracking and Decohesion of Thin Films on Ductile Substrates. *Acta Metall.* **37,** 917–925 (1989).

79. Thouless, M. Crack spacing in brittle films on elastic substrates. *J. Am. Ceram. Soc.* **73,** 2144–2146 (1990).

80. Schuh, C. A. Nanoindentation studies of materials. *Mater. Today* **9,** 32–40 (2006).

81. Whitehead, A. & Page, T. Nanoindentation studies of thin film coated systems. *Thin Solid Films* **220,** 277–283 (1992).

82. Gerberich, W. W., Nelson, J. C., Lilleodden, E. T., Anderson, P. & Wyrobek, J. T. Indentation induced dislocation nucleation: The initial yield point. *Acta Mater.* **44,** 3585–3598 (1996).

83. Hainsworth, S. ., McGurk, M. . & Page, T. . The effect of coating cracking on the indentation response of thin hard-coated systems. *Surf. Coatings Technol.* **102,** 97–107 (1998).

84. Rodriguez-Marek, D., Bahr, D. & Pang, M. Mechanical measurements of passive film fracture on an austenitic stainless steel. *Metall. Mater. Trans. A* **34,** 1291–1296 (2003).

85. Boxley, C. J., White, H. S., Gardner, C. E. & Macpherson, J. V. Nanoscale Imaging of the Electronic Conductivity of the Native Oxide Film on Titanium Using Conducting Atomic Force Microscopy. *J. Phys. Chem.* **107,** 9677–9680 (2003).

86. Pang, M., Eakins, D. E., Norton, M. G. & Bahr, D. F. Structural and mechanical characteristics of anodic oxide films on titanium. *Corrosion* **57,** 523 (2001).

87. Adams, D. P. *et al.* Nanosecond pulsed laser irradiation of titanium: Oxide growth and effects on underlying metal. *Surf. Coatings Technol.* **248,** 38–45 (2014).

88. Jiang, H. G., Rühle, M. & Lavernia, E. J. On the applicability of the x-ray diffraction line profile analysis in extracting grain size and microstrain in nanocrystalline materials. *J. Mater. Res.* **14,** 549–559 (2011).

89. Scherrer, P. No Title. *Goettinger Nachr. Math. Phys.* **2,** 98–100 (1918).

90. Bartkowski, S. *et al.* Electronic structure of titanium monoxide. *Phys. Rev. B* **56,** 10656–10667 (1997).

91. Kramer, D., Huang, H., Kriese, M. & Robach, J. Yield strength predictions from the plastic zone around nanocontacts. *Acta Mater.* **47,** 333–343 (1998).

92. Morasch, K. R. & Bahr, D. F. An energy method to analyze through thickness thin film fracture during indentation. *Thin Solid Films* **515,** 3298–3304 (2007).

93. Bahr, D. F., Woodcock, C. L., Pang, M., Weaver, K. D. & Moody, N. R. Indentation induced film fracture in hard film – soft substrate systems. *Int. J. Fract.* **119/120,** 339–349 (2003).

94. Li, J., Forberg, S. & Hermansson, L. Evaluation of the mechanical properties of hot isostatically pressed titania and titania-calcium phosphate composites. *Biomaterials* **12,** 438–440 (1991).

95. Latella, B. a., Gan, B. K. & Li, H. Fracture toughness and adhesion of thermally grown titanium oxide on medical grade pure titanium. *Surf. Coatings Technol.* **201,** 6325–6331 (2007).

96. Thouless, M. D. Modeling the development and relaxation of stresses in films. *Annu. Rev. Mater.* 69–96 (1995).

97. Khan, R. H. U., Yerokhin, a. L. & Matthews, a. Structural characteristics and residual stresses in oxide films produced on Ti by pulsed unipolar plasma electrolytic oxidation. *Philos. Mag.* **88,** 795–807 (2008).

98. Lee, C.-C., Chen, H.-C. & Jaing, C.-C. Investigation of thermal annealing of optical properties and residual stress of ion-beam-assisted TiO2 thin films with different substrate temperatures. *Appl. Opt.* **45,** 3091–6 (2006).

99. Major, B., Ebner, R., Zieba, P. & Wolczynski, W. Titanium-based films deposited using a Nd: YAG pulsed laser. *Appl. Phys. A Mater. ...* **923,** 921–923 (1999).

100. Kennedy, M. S., Moody, N. R., Adams, D. P., Clift, M. & Bahr, D. F. Environmental influence on interface interactions and adhesion of Au/SiO2. *Mater. Sci. Eng. A* **493,** 299–304 (2008).

101. Nowak, R., Chrobak, D. & Nagao, S. An electric current spike linked to nanoscale plasticity. *Nat. Nanotechnol.* **4,** 287–291 (2009).

102. Holleman, A. F. & Wiberg, E. *Inorganic Chemistry*. 1356 (Academic Press, 2001).

103. Kofstad, P. *Nonstoichiometry, Diffusion, and Electrical Conductivity in Binary Metal Oxides*. 87 (Wiley-Interscience, 1972).

104. Lawrence, S. K. *et al.* Deformation and Fracture of Oxides Fabricated on 304L Stainless Steel via Pulsed Laser Irradiation. *MRS Proc.* **1424,** 73–78 (2012).

105. Huisman, L., Carlsson, A., Jr, C. G. & Ehrenreich, H. Mechanisms for energetic-vacancy stabilization: TiO and TiC. *Phys. Rev. B* **22,** 991–1006 (1980).

106. Valeeva, a., Rempel, a., Sprengel, W. & Schaefer, H.-E. Vacancies on the Ti sublattice in titanium monoxide TiOy studied using positron annihilation techniques. *Phys. Rev. B* **75,** 3–8 (2007).

107. Wautelet, M. & Baufay, L. Laser-induced oxidation of thin cadmium and copper films. *Thin Solid Films* **100,** 5–8 (1982).

108. Ursu, I. *et al.* Vanadium Oxidation as a Result of cw CO_2 Laser Irradiation in Atomospheric Air. *Appl. Phys. A Mater. Sci. Process.* **35,** 103–108 (1984).

109. Cui, C., Hu, J., Liu, Y., Gao, K. & Guo, Z. Morphological and structural characterizations of different oxides formed on the stainless steel by Nd:YAG pulsed laser irradiation. *Appl. Surf. Sci.* **254,** 6537–6542 (2008).

110. Steyer, P. *et al.* Surface modification of martensitic stainless steels by laser marking and its consequences regarding corrosion resistance. *Surf. Eng.* **22,** 167–172 (2006).

111. Adams, D. P. *et al.* Nanosecond pulsed laser irradiation of stainless steel 304L : Oxide growth and effects on underlying metal. *Surf. Coatings Technol.* **222,** 1–8 (2013).

112. Li, Z. L. *et al.* Analysis of oxide formation induced by UV laser coloration of stainless steel. *Appl. Surf. Sci.* **256,** 1582–1588 (2009).

113. Lawrence, S. K., Adams, D. P., Bahr, D. F. & Moody, N. R. Deformation and fracture of a mudflat cracked laser-fabricated oxide on Ti. *J. Mater. Sci.* **48,** 4050–4058 (2013).

114. Cuthrell, R. E. Residual stress anisotropy, stress control, and resistivity in post cathode magnetron sputter deposited molybdenum films. *J. Vac. Sci. Technol. A Vacuum, Surfaces, Film.* **6,** 2914 (1988).

115. Saha, R. & Nix, W. D. Effects of the substrate on the determination of thin film mechanical properties by nanoindentation. *Acta Mater.* **50,** 23–38 (2002).

116. Jiang, W.-G., Su, J.-J. & Feng, X.-Q. Effect of surface roughness on nanoindentation test of thin films. *Eng. Fract. Mech.* **75,** 4965–4972 (2008).

117. Archard, J. F. Contact and Rubbing of Flat Surfaces. *J. Appl. Phys.* **24,** 981 (1953).

118. Oberle, T. L. Properties influencing wear of metals. *J. Met.* **3,** 438 (1951).

119. Richardson, R. C. D. The wear of metals by relatively soft abrasives. *Wear* **11,** 245–275 (1968).

120. Leyland, A. & Matthews, A. On the significance of the H/E ratio in wear control: a nanocomposite coating approach to optimised tribological behaviour. *Wear* **246,** 1–11 (2000).

121. Michler, J. & Blank, E. Analysis of coating fracture and substrate plasticity induced by spherical indentors: diamond and diamond-like carbon layers on steel substrates. *Thin Solid Films* **381,** 119–134 (2001).

122. Tromans, D. & Meech, J. Fracture toughness and surface energies of minerals: theoretical estimates for oxides, sulphides, silicates and halides. *Miner. Eng.* **15,** 1027–1041 (2002).

123. Ibrahim, M. A. M., Abd El Rehim, S. S. & Hamza, M. M. Corrosion behavior of some austenitic stainless steels in chloride environments. *Mater. Chem. Phys.* **115,** 80–85 (2009).

124. Pacquentin, W., Caron, N. & Oltra, R. Nanosecond laser surface modification of AISI 304L stainless steel: Influence the beam overlap on pitting corrosion resistance. *Appl. Surf. Sci.* **288,** 34–39 (2014).

125. Conde, A., García, I. & de Damborenea, J. J. Pitting corrosion of 304 stainless steel after laser surface melting in argon and nitrogen atmospheres. *Corros. Sci.* **43,** 817–828 (2001).

126. Khalfallah, I. Y., Rahoma, M. N., Abboud, J. H. & Benyounis, K. Y. Microstructure and corrosion behavior of austenitic stainless steel treated with laser. *Opt. Laser Technol.* **43,** 806–813 (2011).

127. *Standard Guide for Laboratory Immersion Corrosion Testing of Metals*. 1–10 (2012). doi:10.1520/G0031-12A.

128. *Standard Practice for Operating Salt Spray (Fog) Apparatus 1*. 1–12 (2011). doi:10.1520/B0117-11.2

129. Khatak, H. S. & Raj, B. *Corrosion of Austenitic Stainless Steels: Mechanism, Mitigation, and Monitoring*. 117 (Woodhead, 2002).

130. Davis, J. R. *Stainless Steels*. 3–12 (ASM International, 1994).

131. Trax, R. V. & Holzwarth, J. C. Effect of Chromium Depleted Surface on Corrosion Behavior of Type 430 Stainless Steel. *Corrosion* **16,** 271t–274t (1960).

132. Lawrence, S. K., Adams, D. P., Bahr, D. F. & Moody, N. R. Mechanical and electromechanical behavior of oxide coatings grown on stainless steel 304L by nanosecond pulsed laser irradiation. *Surf. Coatings Technol.* **235,** 860–866 (2013).

133. Chou, W.-J., Yu, G.-P. & Huang, J.-H. Corrosion behavior of TiN-coated 304 stainless steel. *Corros. Sci.* **43,** 2023–2035 (2001).

134. Shieu, F. S., Sung, Y. C., Cheng, L. H., Huang, J. H. & Yu, G. P. Control Of The Corrosion Resistance of TiN-coated AISI 304 Stainless Steel. *Corros. Sci.* **39,** 893–899 (1997).

135. Hakiki, N. E., Montemor, M. F., Ferreira, M. G. S. & Belo, M. C. Semiconducting properties of thermally grown oxide films on AISI 304 stainless steel. *Corros. Sci.* **42,** 687–702 (2000).

136. Guo, L. Q., Lin, M. C., Qiao, L. J. & Volinsky, A. A. Duplex stainless steel passive film electrical properties studied by in situ current sensing atomic force microscopy. *Corros. Sci.* **78,** 55–62 (2014).

137. Mischler, S., Vogel, A., Mathieu, H. J. & Landolt, D. The Chemical Composition of the Passive Film on Fe-24Cr and Fe-24Cr-11Mo Studied by AES , XPS and SIMS. *Corros. Sci.* **32,** 925–944 (1990).

138. Montemor, M. F., Ferreira, M. G. S., Hakiki, N. E. & Da Cunha Belo, M. Chemical composition and electronic structure of the oxide films formed on 316L stainless steel and nickel based alloys in high temperature aqueous environments. *Corros. Sci.* **42,** 1635–1650 (2000).

139. Ferreira, M. G. S. *et al.* Influence of the temperature of film formation on the electronic structure of oxide films formed on 304 stainless steel. *Electrochim. Acta* **46,** 3767–3776 (2001).

140. Noel, J. J. *et al.* Passive oxide films on titanium in aqueous chloride solution probed by electrochemistry, XPS and in situ neutron reflectometry. in *Proc. Symp. Surf. Oxide Film.* (Bardwell, J. A.) 246–257 (Electrochemical Society, Inc., 1996).

141. Griess Jr., J. C. Crevice corrosion of Titanium in Aqueous Salt Solutions. *Corrosion* **24,** 96–109 (1968).

142. Bloyce, A., Qi, P.-Y., Dong, H. & Bell, T. Surface modification of titanium alloys for combined improvements in corrosion and wear resistance. *Surf. Coatings Technol.* **107,** 125–132 (1998).

143. Valente, T. & Galliano, F. . Corrosion resistance properties of reactive plasma-sprayed titanium composite coatings. *Surf. Coatings Technol.* **127,** 86–92 (2000).

144. Zheng, H. Y., Rosseinsky, D. & Lim, G. C. Laser-evoked coloration in polymers. *Appl. Surf. Sci.* **245,** 191–195 (2005).

145. Zheng, H. Y., Qian, H. X. & Zhou, W. Analyses of surface coloration on TiO2 film irradiated with excimer laser. *Appl. Surf. Sci.* **254,** 2174–2178 (2008).

146. Ibrahim, M. A. M., Korablov, S. F. & Yoshimura, M. Corrosion of stainless steel coated with TiN , (TiAl) N and CrN in aqueous environments. *Corros. Sci.* **44,** 815–828 (2002).

147. Hunt, R. W. G. & Pointer, M. R. *Measuring Color*. (John Wiley & Sons, Inc., 2011).

148. Fairman, H. S., Brill, M. H. & Hemmendinger, H. How the CIE 1931 color-matching functions were derived from Wright-Guild data. *Color Res. Appl.* **22,** 11–23 (1997).

149. Smith, T. & Guild, J. The C.I.E. colorimetric standards and their use. *Trans. Opt. Soc.* **33,** 5–134

150. Fossati, A., Borgioli, F., Galvanetto, E. & Bacci, T. Corrosion resistance properties of glow-discharge nitrided AISI 316L austenitic stainless steel in NaCl solutions. *Corros. Sci.* **48,** 1513–1527 (2006).

151. Birnbaum, H. K. & Sofronis, P. Hydrogen-enhanced localized plasticity—a mechanism for hydrogen-related fracture. *Mater. Sci. Eng. A* **176,** 191–202 (1994).

152. Kimura, A. & Birnbaum, H. K. Hydrogen induced grain boundary fracture in high purity nickel and its alloys—Enhanced hydrogen diffusion along grain boundaries. *Acta Metall.* **36,** 757–766 (1988).

153. Kameda, J. & McMahon, C. Solute Segregation and Brittle Fracture in an Alloy Steel. *Metall. Mater. Trans. A* **11,** 91–101 (1980).

154. Takeda, T. & McMahon, C. Strain controlled vs. stress controlled hydrogen induced fracture in a Quenched and Tempered Steel. *Metall. Mater. Trans. A* **12,** 1255–1266 (1981).

155. Gerberich, W. W. & Chen, Y. T. Hydrogen-controlled cracking—An approach to threshold stress intensity. *Metall. Trans. A* **6,** 271–278 (1975).

156. Fleck, N. A., Muller, G. ., Ashby, M. F. & Hutchinson, J. W. Strain Gradient Plasticity: Theory and Experiment. *Acta Met. Mater.* **42,** 475–487 (1994).

157. Vehoff, H. & Rothe, W. Gaseous Hydrogen Embrittlement in FeSi- AND Ni-Single Crystals. *Acta Metall.* **31,** 1781–1793 (1983).

158. Gangloff, R. P. in *Compr. Struct. Integr.* (Milne, I., Ritchie, R. & Karihaloo, B.) 31–101 (Elsevier Science, 2003).

159. Lynch, S. Hydrogen embrittlement phenomena and mechanisms. *Corros. Rev.* **30,** 105–123 (2012).

160. Moody, N. R., Perra, M. W. & Robinson, S. L. Hydrogen pressure and crack tip stress effects on slow crack growth thresholds in an iron-based superalloy. *Scr. Metall.* **22,** 1261–1266 (1988).

161. McMahon, C. Hydrogen-induced intergranular fracture of steels. *Eng. Fract. Mech.* **68,** 773–788 (2001).

162. Bruemmer, S. M., Jones, R. H., Thomas, M. T. & Baer, D. R. Influence of Sulfur , Phosphorus , and Antimony Segregation on the Intergranular Htdrogen Embrittlement of Nickel. *Metall. Mater. Trans. A* **14,** 223–232 (1983).

163. Jones, R. H., Bruemmer, S. M., Thomas, M. T. & Baer, D. R. Hydrogen Pressure Dependence of the Fracture Mode Transition in Nickel. *Metall. Mater. Trans. A* **14,** 1729–1736 (1983).

164. Wada, M., Akaiwa, N. & Mori, T. Field evaporation of iron in neon and hydrogen and its rate-controlling processes. *Philos. Mag. A* **55,** 389–403 (1987).

165. Van der Ven, A. & Ceder, G. The thermodynamics of decohesion. *Acta Mater.* **52,** 1223–1235 (2004).

166. Dadfarnia, M. *et al.* Recent advances in the study of structural materials compatibility with hydrogen. *Adv. Mater.* **22,** 1128–35 (2010).

167. Lee, T. C., Robertson, I. M. & Birnbaum, H. K. An HVEM In situ deformation study of nickel doped with sulfur. *Acta Metall.* **37,** 407–415 (1989).

168. Messmer, R. P. & Briant, C. L. The role of chemical bonding in grain boundary embrittlement. *Acta Mater.* **30,** 457–467 (1982).

169. Barnoush, A. & Vehoff, H. Electrochemical nanoindentation: A new approach to probe hydrogen/deformation interaction. *Scr. Mater.* **55,** 195–198 (2006).

170. Barnoush, A. & Vehoff, H. Recent developments in the study of hydrogen embrittlement: Hydrogen effect on dislocation nucleation. *Acta Mater.* **58,** 5274–5285 (2010).

171. Kheradmand, N., Dake, J. & Barnoush, A. Novel methods for micromechanical examination of hydrogen and grain boundary effects on dislocations. *Philos. Mag.* **92,** 3216–3230 (2012).

172. Bechtle, S., Kumar, M., Somerday, B. P., Launey, M. E. & Ritchie, R. O. Grain-boundary engineering markedly reduces susceptibility to intergranular hydrogen embrittlement in metallic materials. *Acta Mater.* **57,** 4148–4157 (2009).

173. Vlassak, J. J. & Nix, W. D. Measuring the Elastic Properties of Anisotropic Materials by Means of Indentation Experiments. *J. Mech. Phys. Solids* **42,** 1223–1245 (1994).

174. Kittel, C. *Introduction to Solid State Physics*. 53, 64, 233–236 (John Wiley & Sons, Inc., 1986).

175. Plendl, J. N., Mitra, S. S. & Gielisse, P. J. Compressibility, Cohesive Energy, and Hardness of Non-Metallic Solids. *Phys. Status Solidi* **12,** 367–374 (1965).

176. Srivastava, G. P. & Weaire, D. The theory of the cohesive energies of solids. *Adv. Phys.* **36,** 463–517 (1987).

177. Wacke, S., Górecki, T., Górecki, C. & Książek, K. Relations between the cohesive energy, atomic volume, bulk modulus and sound velocity in metals. *J. Phys. Conf. Ser.* **289,** 012020 (2011).

178. Nibur, K., Bahr, D. & Somerday, B. Hydrogen effects on dislocation activity in austenitic stainless steel. *Acta Mater.* **54,** 2677–2684 (2006).

179. Mazzolai, F. M. & Birnbaum, H. K. Elastic constants and ultrasonic attenuation of the α-α’ phase of the Nb-H(D) system. II. Interpretation of results. *J. Phys. F Met. Phys.* **15,** 525–542 (1985).

180. Lunarska, E., Zielnski, A. & Smialowski, M. Effect of Hydrogen on Shear Modulus of Polycrystalline α Iron. *Acta Metall.* **25,** 305–308 (1977).

181. Miller, R. E., Shilkrot, L. E. & Curtin, W. A. A coupled atomistics and discrete dislocation plasticity simulation of nanoindentation into single crystal thin films. *Acta Mater.* **52,** 271–284 (2004).

182. Bahr, D. F. & Vasquez, G. Effect of Solid Solution Impurities on Dislocation Nucleation During Nanoindentation. *J. Mater. Res.* **20,** 1947–1951 (2005).

183. Carter, C. B. & Holmes, S. M. The stacking-fault energy of nickel. *Philos. Mag.* **35,** 1161–1172 (1977).

184. Ferreira, P. J., Robertson, I. M. & Birnbaum, H. K. Hydrogen effects on the character of dislocations in high-purity aluminum. *Acta Mater.* **47,** 2991–2998 (1999).

185. Honeycombe, R. H. W. *Plastic Deformation of Metals*. 81–85 (Edward Arnold, 1984).

186. Wen, M., Zhang, L., An, B., Fukuyama, S. & Yokogawa, K. Hydrogen-enhanced dislocation activity and vacancy formation during nanoindentation of nickel. *Phys. Rev. B* **80,** 094113 (2009).

187. Barnoush, A. & Vehoff, H. In situ electrochemical nanoindentation: A technique for local examination of hydrogen embrittlement. *Corros. Sci.* **50,** 259–267 (2008).

188. Birnbaum, H. K. Hydrogen Effects on Deformation and Fracture : Science and Sociology. *MRS Bull.* **28,** 479–485 (2003).

189. Gerberich, W. in *Gaseous Hydrog. Embrittlement Mater. Energy Technol.* (Gangloff, R. P. & Somerday, B. P.) 209–246 (Woodhead, 2012).

190. Jagodzinski, Y., Hanninen, H., Tarasenko, O. & Smuk, S. Interaction of hydrogen with dislocation pile-ups and hydrogen induced softening of pure iron. *Scr. Mater.* **43,** 245–251 (2000).

191. Cottrell, A. H. & Bilby, B. A. Dislocation Theory of Yielding and Strain Ageing of Iron. *Proc. Phys. Soc.* **62,** 49–62 (1949).

192. Sofronis, P. & Birnbaum, H. K. Mechanics of the hydrogen-dislocation-impurity interactions--I. Increasing shear modulus. *J. Mech. Phys. Solids* **43,** 49–90 (1995).

193. Sirois, E. & Birnbaum, H. K. Effects of hydrogen and carbon on thermally activated deformation in nickel. *Acta Metall.* **40,** 1377–1385 (1992).

194. Tabata, T. & Birnbaum, H. K. Direct observations of the effect of hydrogen on the behavior of dislocations in iron. *Scr. Metall.* **17,** 947–950 (1983).

195. Robertson, I. M. & Birnbaum, H. K. An HVEM study of hydrogen effects on the deformation and fracture of nickel. *Acta Metall.* **34,** 353–366 (1986).

196. Matsumoto, T., Eastman, J. & Birnbaum, H. K. Direct observations of enhanced dislocation mobility due to hydrogen. *Scr. Metall.* **15,** 1033–1037 (1981).

197. Bond, G. M., Robertson, I. M. & Birnbaum, H. K. Effects of hydrogen on deformation and fracture processes in high-purity aluminum. *Acta Metall.* **36,** 2193–2197 (1988).

198. Robertson, I. M. The effect of hydrogen on dislocation dynamics. *Eng. Fract. Mech.* **64,** 649–673 (1999).

199. Martin, M. L., Somerday, B. P., Ritchie, R. O., Sofronis, P. & Robertson, I. M. Hydrogen-induced intergranular failure in nickel revisited. *Acta Mater.* **60,** 2739–2745 (2012).

200. Robertson, I. M., Martin, M. L. & Fenske, J. A. in *Gaseous Hydrog. Embrittlement Mater. Energy Technol.* (Gangloff, R. P. & Somerday, B. P.) 166–206 (Woodhead, 2012).

201. Barnoush, A. & Vehoff, H. Hydrogen embrittlement of aluminum in aqueous environments examined by in situ electrochemical nanoindentation. *Scr. Mater.* **58,** 747–750 (2008).

202. Barnoush, A., Yang, B. & Vehoff, H. Effect of Hydrogen and Grain Boundaries on Dislocation Nucleation and Multiplication Examined with a NI-AFM. *Adv. Solid State Phys.* **47,** 253–269 (2008).

203. Barnoush, A., Asgari, M. & Johnsen, R. Resolving the hydrogen effect on dislocation nucleation and mobility by electrochemical nanoindentation. *Scr. Mater.* **66,** 414–417 (2012).

204. Jones, R. H., Bruemmer, S. M., Thomas, M. T. & Baer, D. R. Effect of Sulfur and Antimony on the Intergranular Fracture of Iron at Cathodic Potentials. *Metall. Trans. A* **13,** 241–249 (1982).

205. Stelmashenko, N. A., Walls, M. G., Brown, L. M. & Milman, Y. V. Microindentations on W and Mo oriented single crystals: An STM study. *Acta Metall. Mater.* **41,** 2855–2865 (1993).

206. Nibur, K. A. & Bahr, D. F. Identifying slip systems around indentations in FCC metals. *Scr. Mater.* **49,** 1055–1060 (2003).

207. Samuels, L. E. & Mulhearn, T. O. An Experimental Investigation of the Deformed Zone Associated with Indentation Hardness Impressions. *J. Mech. Phys. Solids* **5,** 125–134 (1957).

208. Chaudhri, M. M. Subsurface plastic strain distribution around spherical indentations in metals. *Philos. Mag. A* **74,** 1213–1224 (1996).

209. Sangid, M. D., Ezaz, T., Sehitoglu, H. & Robertson, I. M. Energy of slip transmission and nucleation at grain boundaries. *Acta Mater.* **59,** 283–296 (2011).

210. Lee, T. C., Robertson, I. M. & Birnbaum, H. K. An In Situ Transmission Electron Microscope Deformation Study of the Slip Transfer Mechanisms in Metals. *Metall. Trans. A Trans. A* **21,** 2437–2447 (1990).

211. Lim, C. L. & Raj, R. Continuity of Slip Screw and Mixed Crystal Dislocations across Bicrystals of Nickel at 573 K. *Acta Metall.* **33,** 1577–1583 (1985).

212. Kheradmand, N., Vehoff, H. & Barnoush, A. An insight into the role of the grain boundary in plastic deformation by means of a bicrystalline pillar compression test and atomistic simulation. *Acta Mater.* **61,** 7454–7465 (2013).

213. Kheradmand, N. & Vehoff, H. Orientation Gradients at Boundaries in Micron-Sized Bicrystals. *Adv. Eng. Mater.* **14,** 153–161 (2012).

214. Shivachev, B. L. Positron lifetime computations of defects in nickel containing hydrogen or helium. **306,** 105–111 (2002).

215. Nagumo, M. Hydrogen related failure of steels – a new aspect. *Mater. Sci. Technol.* **20,** 940–950 (2004).

216. Nieminen, R. M. & Manninen, M. J. in *Positrons in Solids* (Hautojarvi, P.) 145–195 (Springer, 1979).

217. He, C. *et al.* Detection of hydrogen in neutron-irradiated nickel using positron lifetime spectroscopy. *Philos. Mag.* **89,** 1183–1195 (2009).

218. Xu, Q., Ishizaki, T., Sato, K., Yoshiie, T. & Nagata, S. Coincidence Doppler Broadening of Positron Annihilation Radiation for Detection of Helium in Irradiated Ni and Cu.pdf. *Mater. Trans.* **47,** 2885–2887 (2006).

219. Ohkubo, H. *et al.* Positron-lifetime study of electrically hydrogen charged Ni , austenitic stainless steel and Fe. *J. Nucl. Mater.* **283-287,** 858–862 (2000).

220. Rajainmaki, H., Linderoth, S., Hansen, H. E. & Nieminen, R. M. Defect recovery and hydrogen-vacancy interactions in nickel between 20 and 650 K. *J. Phys. F Met. Phys.* **18,** 1109–1118 (1988).

221. Castro, F. J. & Meyer, G. Thermal desorption spectroscopy (TDS) method for hydrogen desorption characterization (I): theoretical aspects. *J. Alloys Compd.* **330-332,** 59–63 (2002).

222. Tal-Gutelmacher, E., Eliezer, D. & Abramov, E. Thermal desorption spectroscopy (TDS)—Application in quantitative study of hydrogen evolution and trapping in crystalline and non-crystalline materials. *Mater. Sci. Eng. A* **445-446,** 625–631 (2007).

223. Carter, G. Thermal Resolution of Desorption Energy Spectra. *Vacuum* **12,** 245–254 (1962).

224. Corbel, C., Saarinen, K. & Hautojarvi, P. Positron Annihilation Spectroscopy of Vacancy-related Defects in Semiconductors. *Prog. Cryst. Growth Charact.* **25,** 241–256 (1992).

VITA

VITA

Samantha Lawrence graduated from Christian Heritage High School in Utah in 2007. She obtained a B.S. in Metallurgical and Materials Engineering, with an emphasis in metals processing and corrosion engineering, from Colorado School of Mines in December 2010, graduating Magna Cum Laude. Samantha began doctoral studies at Washington State University with Dr. David Bahr in January 2011. In 2012 she was awarded the United States Department of Energy's National Nuclear Security Administration Stewardship Science Graduate Fellowship (DOE NNSA SSGF) to continue studies of materials behavior in extreme conditions. She transferred to Purdue in 2013 and completed doctoral studies in 2014. Her doctoral research focused on assessing mechanisms to predict coupled mechanical behavior and environmental degradation at submicron scales.